

Light Hadron Spectroscopy in Two-flavor Lattice QCD with Small Sea Quark Masses

Yusuke NAMEKAWA

A dissertation submitted to the Doctoral Program
in Physics, the University of Tsukuba
in partial fulfillment of the requirements
for the degree of Doctor of Philosophy in Science

January 2004

Abstract

We study the light hadron spectrum and quark masses in QCD with two flavors of dynamical quarks in small sea quark mass region, corresponding to $m_{PS}/m_V = 0.60 - 0.35$. Numerical simulations are carried out using the RG-improved gauge action and the meanfield-improved clover quark action at $\beta = 1.80(a_\rho = 0.2007(38)$ fm from the ρ meson mass). We observe systematic deviations from the previous chiral extrapolations using $m_{PS}/m_V = 0.80 - 0.55$ with quadratic functions. The difference is especially large for quark masses. The previous quadratic extrapolations overestimated them by $10 - 20(4 - 10\sigma)\%$. Then, combining our previous data, we test several chiral extrapolations to control the errors associated with the chiral extrapolation. We find that the Wilson chiral perturbation theory(WChPT) including a^2 effect, associated with the explicit chiral symmetry breaking of the Wilson-type fermions, as well as the conventional polynomial fitting reproduce our data. The light quark mass through the axial Ward identity is $m_{ud}^{\overline{\text{MS}}}(2 \text{ GeV}) = 2.725(38)$ from WChPT and $m_{ud}^{\overline{\text{MS}}}(2 \text{ GeV}) = 2.851(58)$ from the polynomial extrapolation, indicating additional $5\%(2.2\sigma)$ systematic deviation due to the chiral extrapolation. Our results suggest indispensability of the WChPT formulae for the calculation of quark masses.

Contents

1	Introduction	1
2	Lattice QCD	5
2.1	Formulation	5
2.2	Continuum limit	7
2.3	Improvements of actions	8
2.4	Quenched approximation	10
3	Effective field theory approach for QCD	11
3.1	Chiral perturbation theory	11
3.2	Chiral perturbation theory for Wilson-type fermions	18
4	Previous simulation results in lattice QCD	24
4.1	Quenched QCD	24
4.2	two-flavor full QCD	28
5	Simulations	31
5.1	Simulation parameters and algorithm	31
5.2	Stability of BiCGStab(L) method	32
5.3	Spike	35
6	Results at simulation points	38
6.1	Hadron spectrum	38
6.2	Autocorrelation	41
6.3	Finite size effects	43
7	Chiral extrapolations	47
7.1	Conventional polynomial extrapolation	47

7.2	Naive ChPT extrapolation	60
7.3	WChPT extrapolation	67
8	Observables at the physical point	73
8.1	Deviations from the previous results	73
8.2	Comparison of function form dependence of physical quantities	74
9	Conclusions	77
A	Measurements of observables	84
A.1	Hadron Masses	84
A.2	Decay constants	85
A.3	bare quark masses	86
A.4	Static quark potential	87
A.5	Autocorrelation	87
B	Jackknife error estimation for full QCD simulations	89
C	Renormalization factors and improvement coefficients	90
D	Hadron spectrum data	92

Chapter 1

Introduction

Quarks have been considered as elementary particles of matter for the present. No experimental data has shown the internal structure of quarks. The strong interaction among quarks is formulated by the $SU(3)$ gauge theory called Quantum Chromodynamics(QCD). The non-Abelian structure of QCD brings a special feature of asymptotic freedom. In contrast to the electromagnetic interactions, force between quarks becomes small at short distances, on the other hand, large at long distances. Therefore, at high energies perturbative analysis works well. But at low and intermediate energies perturbative calculations breakdown and non-perturbative methods are needed.

Lattice QCD is a theory that formulates quark and gauge fields on a discrete four-dimensional lattice [1]. This formulation gives a mathematically well-defined path integral. The infinite number of degrees of freedom reduces to finite on lattices. It allows us to calculate non-perturbative properties of QCD by numerical simulations. Hadron spectrum and quark masses, corrections to the weak matrix elements and QCD phase transitions at finite temperature and density have been studied with lattice QCD.

On the other hand, lattice QCD has disadvantages, either. In addition to the statistical error due to the use of numerical method, several systematic errors prevent precise calculations of lattice QCD. There are four major systematic errors in lattice QCD. They are errors caused by continuum extrapolation, renormalization factors, finite size effects and chiral extrapolations.

The systematic errors except that from chiral extrapolations are under control at present. For the continuum extrapolation and the calculation of renormalization factors, improvement methods has been developed. The improved actions and operators decrease lattice artifacts due to discretization of spacetime. Therefore, continuum extrapolation can be taken smoothly from coarse lattices and the error is within a few percent. For the

renormalization factors, which relate lattice quantities to the $\overline{\text{MS}}$ scheme of dimensional regularization, one-loop values by lattice perturbations were often used. But on coarse lattices more than two-loop effects become large and they cause the systematic error. However, non-perturbative renormalization by use of Schrödinger functional method is developed [2]. The systematic errors due to renormalization factors are suppressed well. For finite size effects, no improvement method has not been proposed. But systematic studies of finite size scaling show the relation between a spatial volume and its effects on observables [3–5]. Therefore, finite size effects are also under control.

The only systematic error we have not controlled yet is that from chiral extrapolations. With currently available computer power and simulation algorithms, dynamical sea quark masses which can be explored are far from the physical value. The long extrapolation to the physical u and d quark masses may involve sizable systematic errors. The present conditions of the range of sea quark masses depend on formulations of quarks. Though there are several formulations of quarks on lattices, Kogut-Susskind(KS)-type [6] and Wilson-type fermions [7] are often used in full QCD simulations. For the KS-type quarks, the sea quark masses are down to small values corresponding to the ratio of a pseudoscalar and vector meson masses $m_{PS}/m_V = 0.3$ [8], which is 76% larger than the ratio in the real world $m_\pi/m_\rho = 0.17$. However the KS-type quarks have a problem of non-locality of the action due to the number of flavors. In two-flavor cases, one has to take the square root of the action, which makes the KS-type quark action non-local. Since this non-locality must vanish in the continuum limit, it may be a source of an additional scaling violation. On the other hand, the Wilson-type quarks do not suffer from the non-locality problem. But since the computational costs are larger than those of the KS quarks, the sea quark masses have been limited to heavier values corresponding to $m_{PS}/m_V \gtrsim 0.6$. Another point is that the Wilson-type fermions explicitly breaks the chiral symmetry at finite lattice spacings.

Conventionally chiral extrapolations have been done using a polynomial of a quark mass m_{quark} . The problem of the polynomial extrapolations is that they are expected to need high order terms when they approach the chiral limit to the zero quark mass point. A low energy effective theory, chiral perturbation theory(ChPT), predicts that there is a logarithmic singularity of the form of $m_{quark} \log m_{quark}$ [9]. Though the physical quarks are not massless and the polynomial extrapolations are always possible, we must check how many orders are needed to extrapolate our lattice data to the physical quark mass value reliably. In other words, we have to control the systematic errors due to the contribution of high order terms when we extrapolate lattice data with polynomials.

It is desirable that informations of the quark mass dependence in hadronic quantities are given from some theoretical arguments. For this purpose, ChPT has been adopted to provide a guide for a chiral extrapolation of hadron data. We call the ChPT formulated for QCD in the continuum limit as “naive ChPT” in this thesis. Naive ChPT formulae include the chiral log term and predict fast changes of physical quantities around the chiral limit. A practical problem of the naive ChPT formulae is the application range. For the one-loop formulae of the naive ChPT, the next-to-leading order must be small enough to make sure the next-next-to-leading contribution is negligible. Therefore, the naive ChPT formulae can be applied only in a small sea quark mass region. An estimate from a partially quenched analysis shows $m_{quark} \lesssim m_s/4$ is required [10, 11]. JLQCD collaboration tested the one-loop formulae of the naive ChPT in two-flavor full QCD with Wilson-type fermions [5]. They found, however, their data of $m_{PS}/m_V = 0.8 - 0.6$ are not reproduced by the one-loop formulae. A possible reason for the absence of the chiral logarithm in JLQCD data is that the sea quark mass in their simulations is still too large and the higher order corrections of ChPT should be included to describe the data. Another reason may be the explicit chiral symmetry breaking of the Wilson-type fermions. Effects of the violation of the chiral symmetry appear clearly in various observables such as the difference between the quark mass defined with the vector Ward identity and that with the axial vector Ward identity and the renormalization of the axial current. The contribution of finite lattice spacings to the ChPT formulae should be taken into account on coarse lattices.

Recently several proposals have been made to modify ChPT for the Wilson-type fermion at finite lattice spacings (WChPT) [12–15]. These WChPT formulae are expected to work on coarse lattices because they reflect the effect of the explicit breaking of the chiral symmetry in a theoretically natural way.¹ qq+q collaboration has applied the one-loop naive ChPT and WChPT formulae to their data [19]. They found their data can be described by both the one-loop naive ChPT and WChPT formulae even though they employed heavy sea quark mass data of $m_{PS}/m_V = 0.9 - 0.5$. A subtle point in their studies is that they used coarse lattices of $a \sim 0.19, 0.28$ fm with the unimproved plaquette gauge action and the naive Wilson fermion action. It is not clear if discretization effects are controlled on such coarse lattices.

In this study, we try our best to produce data in realistic sea quark mass regions. We generate configurations of small sea quark masses corresponding to $m_{PS}/m_V = 0.60 - 0.35$,

¹Similar attempts to include the $O(a^2)$ taste violations for the KS-type fermion have been made [16–18].

extending our previous study in two-flavor full QCD with Wilson-type fermions [20]. Since the computational costs toward the chiral limit grow rapidly, roughly proportional to $(m_{PS}/m_V)^{-6}$ [21], we are forced to use a coarse lattice of $a_\rho = 0.2007(38)$ fm determined from the rho meson mass. To reduce the effects of a finite lattice spacing, we employ an improved gauge and quark action. Our simulations are performed at $\beta = 1.80$ using a renormalization-group(RG) improved gauge action and a meanfield-improved clover quark action.

Using these configurations, we calculate the light hadron spectrum and quark masses and extrapolate them to the physical point. The validity of the quadratic extrapolations in the previous work is examined by estimating the deviations of our new data from the previous extrapolations. Then we study several extrapolation function forms including polynomials and the ChPT-based ones. The adaptability and convergence of these formulae are examined. We find the previous quadratic forms fail to describe our data. On the other hand, polynomials including higher order terms as well as WChPT formulae reproduce our data well.

Finally, we compare the results at the physical point. Deviations from the previous results are estimated. Then dependence of physical quantities on the extrapolation formulae is discussed and their systematic deviations are studied. We confirm that the previous quadratic chiral extrapolations give 10 – 20% systematic difference in the quark masses. Moreover, the WChPT formulae show further differences implying its necessity for the quark mass calculation. Preliminary results of these calculations have been reported in Ref. [22].

This thesis is organized as follows. We formulate QCD on lattices in Chap. 2. Then Chap. 3 is devoted to the explanation of an alternative effective approach for QCD. After reviewing the previous lattice QCD calculations in Chap. 4, we describe details of our simulations in Chap. 5. Chap. 6 is devoted to detailed description of our simulation results. Then we discuss chiral extrapolations in Chap. 7 and the extrapolated results at the physical point in Chap. 8. Our conclusion is given in Sec. 9.

Chapter 2

Lattice QCD

Lattice QCD is the most successful theory to deal with QCD in low and intermediate energy regions. It allows us to study QCD non-perturbatively from the first principle by use of numerical techniques. In this chapter, we briefly explain the formulation of lattice QCD.

2.1 Formulation

The partition function of QCD is written in the Euclidean path integral formulation

$$Z = \int \mathcal{D}A \mathcal{D}\psi \mathcal{D}\bar{\psi} e^{-S_{QCD}[A, \psi, \bar{\psi}]}, \quad (2.1)$$

where the QCD action S_{QCD} consists of the gauge fields A_μ and the quark fields ψ such that

$$S_{QCD}[A, \psi, \bar{\psi}] = \int d^4x \left(\frac{1}{4} (F_{\mu\nu}^a)^2 + \bar{\psi} (\not{D} + m) \psi \right). \quad (2.2)$$

The field strength is

$$F_{\mu\nu}^a = \partial_\mu A_\nu^a - \partial_\nu A_\mu^a + g_0 f^{abc} A_\mu^b A_\nu^c, \quad (2.3)$$

where f^{abc} are the structure constants of $SU(3)$ and g_0 is the bare coupling. The covariant derivative is defined by

$$D_\mu = \partial_\mu - ig_0 A_\mu^a t^a, \quad (2.4)$$

where t^a is the generator of $SU(3)$. S_{QCD} is invariant under Lorentz and color $SU(3)_c$ transformation. In addition to these exact symmetries, S_{QCD} has an approximate flavor symmetry. In the chiral limit $m = 0$, S_{QCD} has a $U(N_f)_L \otimes U(N_f)_R$ symmetry. However, due to the Adler-Bell-Jackiw anomaly, $U(N_f)_L \otimes U(N_f)_R = SU(N_f)_L \otimes SU(N_f)_R \otimes U(1)_V \otimes U(1)_A$ breaks into $SU(N_f)_L \otimes SU(N_f)_R \otimes U(1)_V$. $SU(N_f)_L \otimes SU(N_f)_R$ shows

the chiral symmetry and $U(1)_V$ the quark number symmetry. Actually S_{QCD} is invariant under the following chiral transformation

$$\psi_L \rightarrow L\psi_L, \bar{\psi}_L \rightarrow \bar{\psi}_L L^\dagger, \quad (2.5)$$

$$\psi_R \rightarrow R\psi_R, \bar{\psi}_R \rightarrow \bar{\psi}_R R^\dagger, \quad (2.6)$$

where $L, R \in SU(N_f)$ with the number of light quark masses N_f . $\psi_{L,R}$ are the left and right-handed quark field,

$$\psi_{L,R} = P_{L,R}\psi, \quad P_{L,R} \equiv \frac{1}{2}(1 \pm \gamma_5). \quad (2.7)$$

The lattice QCD action $S_{QCD}^{lattice}$ is constructed to recover S_{QCD} in the continuum limit. $S_{QCD}^{lattice}$ consists of the gauge and fermion parts.

$$S_{QCD}^{lattice} = S_G[U] + S_F^{(W)}[U, \psi, \bar{\psi}]. \quad (2.8)$$

The gauge part is

$$S_G[U] = \beta \sum_{n,\mu\nu} \left(1 - \frac{1}{N_c} U_{\mu\nu}(n) \right), \quad (2.9)$$

where N_c is the number of colors ($N_c = 3$) and $U_{\mu\nu}(n)$ is a plaquette with the base site n lying on the $\mu - \nu$ plane,

$$U_{\mu\nu}(n) \equiv U_\mu(n) U_\nu(n + \hat{\mu}) U_\mu^\dagger(n + \hat{\nu}) U_\nu^\dagger(n). \quad (2.10)$$

The $\hat{\mu}$ means a unit vector along the μ direction. The gauge field $A_\mu(n)$ is defined on the link between the site n and $n + \hat{\mu}$ as

$$U_\mu(n) = e^{i a g_0 A_\mu(n)}, \quad (2.11)$$

where a is a lattice spacing. The lattice action must be the continuum one in the limit $a \rightarrow 0$,

$$\lim_{a \rightarrow 0} S_G = \frac{1}{4} \int d^4x F_{\mu\nu}^a F_{\mu\nu}^a. \quad (2.12)$$

This condition determines the parameter β in S_G (2.9) as

$$\beta = \frac{2N_c}{g_0^2}. \quad (2.13)$$

The fermion part of the action with Wilson fermions is

$$\begin{aligned} S_F^{(W)}[\psi, \bar{\psi}, U] &= (\hat{m}_0 + 4r) \sum_n \hat{\bar{\psi}}(n) \hat{\psi}(n) \\ &\quad - \frac{1}{2} \sum_{n,\mu} \left(\hat{\bar{\psi}}(n) (r - \gamma_\mu) U_\mu(n) \hat{\psi}(n + \hat{\mu}) + \hat{\bar{\psi}}(n + \hat{\mu}) (r + \gamma_\mu) U_\mu^\dagger(n) \hat{\psi}(n) \right), \end{aligned} \quad (2.14)$$

where r is a Wilson parameter. The dimensionless bare mass \hat{m}_0 and quark fields $\hat{\psi}$ are defined as follows,

$$\hat{\psi} = a^{\frac{3}{2}}\psi, \quad (2.15)$$

$$\hat{m}_0 = am_0. \quad (2.16)$$

Though for $r \neq 0$ the chiral symmetry is explicitly broken, it removes doublers. The naive formulation of fermion produces doublers, which are pure lattice artifacts having no continuum analog. $S_F^{(W)}$ recover the fermion action in the continuum theory without doublers.

$$\lim_{a \rightarrow 0} S_F^{(W)} = \int d^4x \left(\bar{\psi} (\not{D} + m) \right). \quad (2.17)$$

2.2 Continuum limit

We discuss the scaling and the continuum limit in this section. Let us consider an observable O with the mass dimension d_O . The corresponding lattice quantity \hat{O} is measured in units of the lattice spacing a on a lattice.

$$O(g_0, a) = \left(\frac{1}{a} \right)^{d_O} \hat{O}(g_0). \quad (2.18)$$

Since QCD has the asymptotic freedom, the continuum limit $a \rightarrow 0$ is realized for $g_0 \rightarrow 0$.

$$\lim_{g_0 \rightarrow 0} O(g_0, a) = O_{phys}. \quad (2.19)$$

For sufficiently small g_0 the QCD β function has the form

$$\beta(g_0) = -a \frac{dg_0}{da} = -b_0 g_0^3 - b_1 g_0^5, \quad (2.20)$$

$$b_0 = \frac{1}{16\pi^2} \left(11 - \frac{2}{3} N_f \right), \quad (2.21)$$

$$b_1 = \frac{1}{(16\pi^2)^2} \left(102 - \frac{38}{3} N_f \right), \quad (2.22)$$

where N_f is the number of flavors of massless quarks. Integrating this β function leads to

$$a = \frac{1}{\Lambda_L} f(g_0), \quad (2.23)$$

where Λ_L is an integration constant called lattice Λ_{QCD} parameter and $f(g_0)$ is the two-loop scaling function of $SU(3)$ gauge theory,

$$f(g_0) = (b_0 g_0^2)^{-\frac{b_1}{2b_0^2}} e^{-\frac{1}{2b_0 g_0^2}}. \quad (2.24)$$

Substituting (2.23) and (2.18) into (2.19) implies

$$\hat{O}(g_0, a) \sim \hat{C} f(g_0)^{d_O} \quad \text{for sufficiently small } g_0, \quad (2.25)$$

where \hat{C} is a dimensionless constant. This relation is called asymptotic scaling. By studying the ratio $\frac{\hat{O}(g_0)}{(f(g_0))^{d_O}}$ as a function of g_0 in this scaling region we can determine the constant \hat{C} . However our simulations are usually carried out of the asymptotic scaling region, we conventionally fix a by identifying the rho meson mass $a(g_0) = \hat{m}_\rho(g_0)/m_\rho$.

2.3 Improvements of actions

Simulations on fine lattices are desirable to obtain the continuum limit values but it requires large computational resources. On the other hand, simulations on coarse lattices are cheap but they are usually out of the scaling region and are not useful for continuum extrapolations. Therefore, in order to obtain a reliable result from coarse lattices, improved actions are often used. The improvement reduces cutoff effects. It leads to a better scaling from coarse lattices. We briefly explain the improvements in the gauge and quark actions.

First, we consider the gauge sector. Due to the universality, there are infinitely many candidates for the lattice action describing the same continuum limit. We can introduce higher order terms ΔS_i to the standard lattice gauge action of Eq. (2.9).

$$S_{improved} = c_0 S_{standard} + c_1 \Delta S_1 + c_2 \Delta S_2 + \dots, \quad (2.26)$$

where the coefficients c_i must satisfy a condition that the leading order of the action reproduces the continuum action. Since we can adjust c_i under this condition, lattice artifacts can be suppressed by the choice of c_i .

There are two major methods to determine c_i . One is the Symanzik improvement and the other is the renormalization group(RG) improvement. The Symanzik improvement is based on perturbations. The gauge action is expanded in powers of the lattice spacing a and c_i are adjusted such that up to $O(a^n)$ contributions are canceled [23]. The RG improvement is based on the analysis of the RG group flow. A block transformation of a field shows that there are two fixed points P_0 and P_∞ . P_0 corresponds to the strong coupling limit and P_∞ the weak coupling i.e. continuum limit. These two fixed points are connected by a renormalized trajectory(RT). All the actions on RT, called perfect actions, describe the same physics as that at P_∞ . However, an infinite number of parameters are needed for the perfect action. In practical simulations, we restrict ourselves to a small

number of coupling parameters, which make the action close to RT as much as possible. Y. Iwasaki proposed an RG action that includes only plaquette and rectangular loops but becomes close to RT after one or two block transformations [24]. c_i are determined by evaluating the distance from RT with the perturbative calculation of the Wilson loop.

$$c_0 = 1 - 8c_1, \quad c_1 = -0.331. \quad (2.27)$$

Next, we move on to the quark sector. The naive Wilson quark action defined in Eq. (2.14) has $O(a)$ discretization errors. $O(a)$ improved Wilson fermion is realized by adding the clover term [25].

$$S_F^{(O(a)-improved)} = S_F^{(W)} + S_F^{(Clover)}, \quad (2.28)$$

$$S_F^{(Clover)} \equiv -a^5 c_{\text{SW}} \kappa \frac{1}{2} \sum_{n, \mu, \nu} \bar{\psi}(n) \sigma_{\mu\nu} F_{\mu\nu}(n) \psi(n), \quad (2.29)$$

where $\sigma_{\mu\nu} = (i/2)[\gamma_\mu, \gamma_\nu]$ and the field strength $F_{\mu\nu}$ is defined as

$$F_{\mu\nu}(n) = \frac{1}{8i} ((U_{\mu\nu}(n) + U_{-\mu\nu}(n) + U_{-\mu-\nu}(n) + U_{\mu-\nu}(n)) - (h.c.)). \quad (2.30)$$

The parameter c_{SW} is chosen so that the $O(a)$ contribution cancels. At the tree level, $O(a)$ improvement is achieved with $c_{\text{SW}} = 1$ for $r = 1$. The one-loop value of c_{SW} has also been obtained, but it does not work well because of the poor convergence of lattice perturbation. Since tadpole loops make the convergence worse, the meanfield improvement(tadpole improvement) is invented [26]. It simply substitutes U as follows.

$$U_\mu(n) \rightarrow \frac{U_\mu(n)}{u_0}, \quad (2.31)$$

where u_0 is a meanfield value for U . This replacement corresponds to the change of the expansion parameter from the bare coupling g to $g' = g/u_0^2$. The modified perturbation shows better convergence at rather large g , where numerical simulations have been done. This meanfield improvement is adopted for C_{SW} by

$$c_{\text{SW}} \rightarrow \frac{c_{\text{SW}}}{u_0^3}, \quad (2.32)$$

where we redefined the hopping parameter κ as $\kappa \rightarrow \kappa/u_0$. We note that with the plaquette gauge action the non-perturbative value of C_{SW} has been obtained by use of the Schrödinger functional method [27].

2.4 Quenched approximation

Let us explain the quenched approximation, which was often used at the early stage of lattice QCD study.

The quark fields ψ are bilinear in $S_F^{(W)}$,

$$S_F^{(W)} = \hat{\bar{\psi}} K \hat{\psi}. \quad (2.33)$$

Therefore we can immediately perform the Grassmann integrals in the partition function. The result is

$$Z = \int \mathcal{D}U \, e^{-S_{eff}} \quad (2.34)$$

where the effective action S_{eff} is given by

$$S_{eff} = S_G - \log \det K. \quad (2.35)$$

The quenched approximation is take $\det K = 1$. In this approximation dynamical quark effects are ignored because $\det K$ means the vacuum polarization effects. It is given by the sum of single fermion loops with an arbitrary number of external gluons attached to them. This quenched approximation reduces the simulation cost by $O(100)$ times.

Chapter 3

Effective field theory approach for QCD

Due to the asymptotic free character of QCD, perturbative analysis can be applied only in a high energy region. At low energies, a perturbation with fundamental parameters of QCD goes beyond its radius of convergence. Instead of using the fundamental parameters of QCD such as lattice QCD, there is an effective approach that employs the bound states as more natural variables for a low energy region. As long as an effective theory respects the symmetries of QCD and the relevant variables are identified, it provides the same physics in its application energy range. This chapter is devoted to explanations of such effective theories.

3.1 Chiral perturbation theory

Chiral perturbation theory(ChPT) is a typical example of an effective theory for QCD [9]. First, ChPT respects all symmetries respected by QCD. QCD has color, flavor and Lorentz symmetry. The color symmetry gives no effect on ChPT, because quarks are confined and therefore hadrons are color-singlet. On the other hand, flavor and Lorentz symmetry restrict the form of ChPT effective Lagrangian. Second, the fundamental degrees of freedom of ChPT are identified with the light pseudoscalar mesons: π^0, π^\pm for $N_f = 2$ case and $\pi^0, \pi^\pm, K^0, \overline{K}^0, K^\pm, \eta^0$ for $N_f = 3$ case, where N_f is the number of flavors of light quarks.

ChPT is based on the following two assumptions. One is that in the chiral limit, the global $SU(N_f)_L \otimes SU(N_f)_R$ chiral symmetry in massless QCD is spontaneously broken into $SU(N_f)_{L+R=V}$ and the pseudoscalar mesons are identified with the corresponding Nambu-Goldstone(NG) bosons. The other is that the light quark masses are treated as small

perturbations around the chiral limit. According to these hypotheses, ChPT Lagrangian is constructed with the most general Lagrangian invariant under $SU(N_f)_L \otimes SU(N_f)_R$ and the explicit flavor breaking terms of quark masses transforming linearly.

Though the symmetries determine the form of ChPT Lagrangian, an infinite number of terms can be included. Therefore, we must order the terms by their importance for the effective theory to be a predictive. Since we want to create a low-energy effective theory, we perform an energy expansion of the physical amplitudes. In that case, terms with lower powers have a greater importance. This power counting rule is concretely discussed below.

Before explaining the concrete form of the ChPT Lagrangian, we note that even renormalizability is not necessary for an effective theory. An effective theory works in the energy range below some cutoff, $E < \Lambda$. Actually renormalizable theories are a subset of effective field theories. The advantage of renormalizable theories is that it is very predictive. Only a finite set of couplings are needed independently of the energy range. On the other hand, they have a disadvantage that their validity range is not explicitly shown. To ensure a predictive power to ChPT below some cutoff Λ_{ChPT} , we only need renormalizability order by order in the energy expansion of E/Λ_{ChPT} . Strictly, if for any $n \geq 0$ the number of counterterms contributing at $O(E^n)$ to the physical amplitudes is finite, then only a finite set of couplings is needed to describe the physics at $E < \Lambda_{ChPT}$ with arbitrary accuracy. We note that ChPT picture also breaks down at energies where particles that are not included in ChPT (ex. ρ meson) play an essential role as well as $E \sim \Lambda_{ChPT}$.

The ChPT Lagrangian is constructed as follows.

$$\mathcal{L}_{ChPT} = \mathcal{L}_{NG} + \mathcal{L}_{quark} \quad (3.1)$$

where \mathcal{L}_{NG} purely consists of the NG boson fields and \mathcal{L}_{quark} includes the explicit flavor breaking terms of light quark masses. The NG boson fields are associated to the coordinates of the coset space $SU(N_f)_L \otimes SU(N_f)_R / SU(N_f)_V$, transforming non-linearly under $SU(N_f)_L \otimes SU(N_f)_R$ but linearly under $SU(N_f)_V$. It is useful to introduce a non-linear realization of a spontaneously broken symmetry to construct the most general Lagrangian invariant under $SU(N_f)_L \otimes SU(N_f)_R$. I employ the exponential parameterization in the $N_f \times N_f$ flavor space. For $N_f = 2$ case, it is written as follows.

$$U = \exp \left(i \sum_{a=1}^3 \pi_a \sigma^a / f \right) \in SU(N_f = 2), \quad (3.2)$$

where f is a constant that is not determined by the symmetry, π are pseudoscalar meson fields and σ are Pauli matrices. The choice of U is not unique, but all possible formula-

tions lead to the same physical results. Under the chiral transformation of Eq. (2.6), U transforms linearly under $SU(N_f)_L \otimes SU(N_f)_R$,

$$U \rightarrow LUR^\dagger. \quad (3.3)$$

π transforms linearly under vector transformation $SU(N_f)_V$,

$$\pi \rightarrow V\pi V^\dagger, \quad V = L = R. \quad (3.4)$$

In the other cases, π transforms non-linearly.

Next we explain on the form of \mathcal{L}_{NG} . NG bosons can only interact when they carry momentum. The interaction terms for the NG bosons always contain derivatives because of the chiral symmetry. Therefore, NG bosons interact weakly at low energies. It allows us to expand \mathcal{L}_{NG} according to the momentum of NG bosons (p^2/Λ_{ChPT}^2) at low energies.

$$\mathcal{L}_{NG} = \mathcal{L}_{NG}^{(0)} + \mathcal{L}_{NG}^{(2)} + \mathcal{L}_{NG}^{(4)} + \dots, \quad (3.5)$$

where the subscript shows the order of p or the highest number of derivatives. $\mathcal{L}_{ChPT}^{(0)}$ term is an uninteresting constant. It just represents the vacuum energy of QCD in the chiral limit. Not only $\mathcal{L}_{ChPT}^{(1)}$ term but all odd order terms are forbidden by the Lorentz and parity symmetry. A nontrivial structure first appears at $\mathcal{L}_{NG}^{(2)}$. $\mathcal{L}_{NG}^{(2)}$ is uniquely determined as follows.

$$\mathcal{L}_{NG}^{(2)} = \frac{f^2}{4} \text{Tr} \left(\partial_\mu U \partial^\mu U^\dagger \right). \quad (3.6)$$

f is introduced to reproduce the standard kinetic term, explained later in detail. Notice that $\partial_\mu U$ corresponds to the power of momentum.

Then, after some preparations, we show the concrete form of \mathcal{L}_{quark} . $SU(N_f)_L \otimes SU(N_f)_R$ is not an exact symmetry of QCD because of non-zero quark masses. But the variation in the action due to quark masses can be compensated by the transformation of the quark mass matrix. Therefore, we can make an invariant action under $SU(N_f)_L \otimes SU(N_f)_R$ with quark mass terms. The quark mass matrix m for $N_f = 2$ case is defined as

$$m = \begin{pmatrix} m_u & 0 \\ 0 & m_d \end{pmatrix} \quad (3.7)$$

It is convenient to count m as $O(p^2)$ such that \mathcal{L}_{quark} starts at $O(p^2)$ and only even order terms appear. It is also convenient to use the “spurion analysis”. It reproduces the explicit symmetry breaking due to the quark mass correctly. In the spurion analysis, we distinguish m and m^\dagger so that the mass term becomes

$$\overline{\psi}_L m \psi_R + \overline{\psi}_R m^\dagger \psi_L. \quad (3.8)$$

This mass term is invariant under $SU(N_f)_L \otimes SU(N_f)_R$, if m transforms as

$$m \rightarrow LmR^\dagger, m^\dagger \rightarrow Rm^\dagger L^\dagger. \quad (3.9)$$

With these preparations, \mathcal{L}_{quark} can be expressed as an expansion in powers of quark masses (m_{quark}/Λ_{ChPT}).

$$\mathcal{L}_{quark} = \mathcal{L}_{quark}^{(2)} + \mathcal{L}_{quark}^{(4)} + \dots \quad (3.10)$$

$\mathcal{L}_{quark}^{(2)}$ is given by

$$\mathcal{L}_{quark}^{(2)} = \frac{f^2 B}{2} \text{Tr} (mU^\dagger + Um^\dagger), \quad (3.11)$$

where B is another unknown constant, which should be determined by the data out of ChPT.

Expanding U in powers of π such that $U = 1 + i(\pi \cdot \sigma)/f + \dots$ reveals us the relation between the pseudoscalar meson mass and B . It also shows the correspondence of B to the quark condensate and f to f_π . At $O(\pi^2)$ order, the leading order chiral Lagrangian \mathcal{L}_{ChPT}^{LO} is expressed as

$$\mathcal{L}_{ChPT}^{LO} = \mathcal{L}_{tree}^{(2)} = \mathcal{L}_{NG}^{(2)} + \mathcal{L}_{quark}^{(2)} \quad (3.12)$$

$$= (m_u + m_d)f^2 B + \frac{1}{2}(\partial_\mu \pi \partial^\mu \pi) - \frac{1}{2}(m_u + m_d)B\pi^2 + O(\pi^4). \quad (3.13)$$

The second term is a usual kinetic term and the third term represents the PCAC relation between m_π and B ,

$$m_\pi^2 = (m_u + m_d)B + O(m^2). \quad (3.14)$$

The first term shows a contribution to the potential *i.e.* the vacuum energy, which leads to the relation between B and the quark condensate. The energy shift can be written as

$$\Delta E_0 = -V(m_u + m_d)f^2 B, \quad (3.15)$$

where V is the volume factor. On the other hand, ΔE_0 is given in QCD at the leading order of quark masses as follows.

$$\Delta E_0 = \langle 0 | H_{QCD}^{(1)} | 0 \rangle = V \langle 0 | m_u \bar{u}u + m_d \bar{d}d | 0 \rangle. \quad (3.16)$$

Therefore, we have

$$\langle 0 | m_u \bar{u}u + m_d \bar{d}d | 0 \rangle = -(m_u + m_d)f^2 B + O(m^2). \quad (3.17)$$

In the chiral limit, it gives

$$B = -\frac{1}{f^2} \frac{\langle 0 | \bar{u}u + \bar{d}d | 0 \rangle}{N_f}. \quad (3.18)$$

To examine the relation between f and the pion decay constant f_π , we work out the vacuum to pion matrix element of the axial current. It is convenient to introduce external sources v_μ, a_μ, s and p both in the QCD and ChPT Lagrangian such that they are invariant under $SU(N_f)_L \otimes SU(N_f)_R$ at finite quark masses. Keeping $SU(N_f)_L \otimes SU(N_f)_R$ requires transformations of external sources under $SU(N_f)_L \otimes SU(N_f)_R$ as,

$$l_\mu \equiv v_\mu - a_\mu \rightarrow L l_\mu L^\dagger, \quad (3.19)$$

$$r_\mu \equiv v_\mu + a_\mu \rightarrow R r_\mu R^\dagger, \quad (3.20)$$

$$s - ip \rightarrow L(s - ip)R^\dagger, \quad (3.21)$$

$$s + ip \rightarrow R(s + ip)L^\dagger. \quad (3.22)$$

and the QCD Lagrangian becomes

$$\mathcal{L}_{QCD}(v, a, s, p) = \mathcal{L}_{QCD}(v = a = s = p = 0) + \bar{q}\gamma^\mu(v_\mu + a_\mu\gamma_5)q - \bar{q}(s - ip\gamma_5)q. \quad (3.23)$$

The quark mass terms, which explicitly breaking $SU(N_f)_L \otimes SU(N_f)_R$, can be recovered by functional derivatives of the partition function $Z(v, a, s, p)$ at $v_\mu = a_\mu = p = 0$ and $s = m$. \mathcal{L}_{ChPT}^{LO} in Eq. (3.12) with external sources is expressed as

$$\mathcal{L}_{ChPT}^{LO}(v, a, s, p) = \frac{f^2}{4} \text{Tr} \left(D_\mu U D^\mu U^\dagger + \chi U^\dagger + U \chi^\dagger \right), \quad (3.24)$$

where

$$D_\mu U \equiv \partial_\mu U + i l_\mu U - i U r_\mu \quad (3.25)$$

$$\chi \equiv 2B(s + ip). \quad (3.26)$$

We note that though s, p is counted $O(p^2)$, v_μ, a_μ is $O(p)$ because of the local invariance of D_μ . Then differentiating the action $S_{ChPT}^{LO}(v, a, s, p) = \int d^4x \mathcal{L}_{ChPT}^{LO}(v, a, s, p)$ with respect to the external sources, the axial current operator A_μ^a is identified with

$$A_\mu^a = \frac{\delta S_{ChPT}^{LO}}{\delta a_\mu^a} = -i \frac{f^2}{2} \text{Tr} \left(U^a (\partial^\mu U^\dagger) - (\partial^\mu U) U_a^\dagger \right) = -f \partial^\mu \pi_a + O(\pi^3). \quad (3.27)$$

It leads to

$$\langle 0 | A_\mu^a | \pi \rangle = \langle 0 | (+f i p_\mu \pi^a) \pi^{a,\dagger} | 0 \rangle = i p_\mu f. \quad (3.28)$$

Therefore, f is related to f_π as follows.

$$f_\pi = f + O(m). \quad (3.29)$$

We note that we can construct not only the axial vector operator A_μ^a but the scalar S^0 , pseudoscalar P^a and vector operators V_μ^a using external sources.

$$S^0 = -\frac{\delta S}{\delta s}, \quad (3.30)$$

$$P^a = -i\frac{\delta S}{\delta p^a}, \quad (3.31)$$

$$V_\mu^a = \frac{\delta S}{\delta v_\mu^a}, \quad (3.32)$$

$$A_\mu^a = \frac{\delta S}{\delta a_\mu^a}. \quad (3.33)$$

Here we summarize the power counting rules. For the momentum of the NG boson p ,

$$U \sim O(p^0), \quad (3.34)$$

$$D_\mu U, a_\mu, v_\mu \sim O(p^1), \quad (3.35)$$

$$s, p \sim O(p^2). \quad (3.36)$$

At the leading order, $\mathcal{L}_{tree}^{(2)}$ is needed. However, at the next-to-leading order, not only $\mathcal{L}_{tree}^{(4)}$ but also one-loop contributions of $\mathcal{L}_{1-loop}^{(2)}$ are required.

$$\mathcal{L}_{ChPT}^{NLO} = \mathcal{L}_{1-loop}^{(2)} + \mathcal{L}_{tree}^{(4)}. \quad (3.37)$$

For $N_f = 2(m_u = m_d = m)$ case, $\mathcal{L}_{tree}^{(4)}$ is given by

$$\begin{aligned} \mathcal{L}_{tree}^{(4)} &= \frac{1}{4}l_1 \left(\text{Tr} \left(\partial_\mu U \partial^\mu U^\dagger \right) \right)^2 + \frac{1}{4}l_2 \left(\text{Tr} \left(\partial_\mu U \partial_\nu U^\dagger \right) \text{Tr} \left(\partial^\mu U \partial^\nu U^\dagger \right) \right) \\ &\quad + \frac{1}{4}l_4 \left(\text{Tr} \left(\partial_\mu U \partial^\mu U^\dagger \right) \text{Tr} \left(mB_0 (U + U^\dagger) \right) \right) \\ &\quad + \frac{1}{4}(l_3 + l_4) \left(\text{Tr} \left(mB_0 (U + U^\dagger) \right) \right)^2 \end{aligned} \quad (3.38)$$

$$= \frac{1}{2} \left(\frac{4l_4 m B_0}{f^2} \right) \partial_\mu \pi \partial^\mu \pi - \frac{4m^2 B_0^2 (l_3 + l_4)}{f^2} \pi^2 + O(\pi^4). \quad (3.39)$$

On the other hand, for $\mathcal{L}_{1-loop}^{(2)}$ expressing the $O(\pi^4)$ in Eq. (3.13) leads to

$$\begin{aligned} \mathcal{L}_{1-loop}^{(2)} &= \text{const.} + \frac{1}{2} \left(\partial_\mu \pi \partial^\mu \pi - m_0^2 \pi^2 \right) \\ &\quad + \frac{1}{6f^2} \left((\pi \partial_\mu \pi)^2 - (\partial_\mu \pi \partial^\mu \pi) \pi^2 \right) + \frac{m_0^2}{24f^2} (\pi^2)^2 \end{aligned}$$

where

$$m_0^2 = 2mB_0. \quad (3.40)$$

The pion propagator at one-loop order is obtained by loop integrals. Using the pion propagator at the tree level,

$$\langle \pi^a(-p) \pi^b(p) \rangle = \delta^{ab} \frac{1}{p^2 + m_0^2}. \quad (3.41)$$

Then the loop integrals are evaluated as follows.

$$\langle \pi^a(x) \pi^b(x) \rangle = \delta^{ab} \frac{m_0^2}{(4\pi)^2} \log \frac{m_0^2}{\Lambda_3^2} \equiv \delta^{ab} I, \quad (3.42)$$

$$\langle \partial_\mu \pi^a(x) \partial_\nu \pi^b(x) \rangle = \delta^{ab} \delta_{\mu\nu} \left(-\frac{m_0^2}{4} I \right), \quad (3.43)$$

where Λ_3 is a scale parameter in the $\overline{\text{MS}}$ scheme. The divergence is absorbed in the renormalization of l_3 . The inverse pion propagator at one-loop is calculated as

$$\begin{aligned} \mathcal{L}_{ChPT}^{NLO} &= \frac{1}{2} (\partial_\mu \pi)^2 \left(1 - \frac{2I}{3f^2} \right) + \frac{1}{2} \pi^2 \left(m_0^2 \left(1 - \frac{I}{6f^2} \right) \right) \\ &= \frac{1}{2} \left((\partial_\mu \pi_R)^2 + m_\pi^2 \pi_R^2 \right), \end{aligned} \quad (3.44)$$

where

$$\pi = Z^{1/2} \pi_R \quad (3.45)$$

$$Z = \left(1 - \frac{2I}{3f^2} \right)^{-1} \quad (3.46)$$

$$m_\pi^2 = m_0^2 \left(1 + \frac{1}{N_f} \frac{m_0^2}{(4\pi f)^2} \log \frac{m_0^2}{\Lambda_3^2} \right). \quad (3.47)$$

The decay constant at one-loop order is obtained as in the case of the tree level.

$$f_{PS} = f \left(1 - \frac{N_f}{2} \frac{m_0^2}{(4\pi f)^2} \log \frac{m_0^2}{\Lambda_4^2} \right). \quad (3.48)$$

The symmetry does not determine the numerical values of Λ_3 and Λ_4 . The phenomenological estimates are [9, 28]

$$0.2 \text{ GeV} < \Lambda_3 < 2 \text{ GeV}, \quad (3.49)$$

$$\Lambda_4 = 1.26 \pm 0.14 \text{ GeV}. \quad (3.50)$$

Λ_4 is calculated rather accurately from the $I = 0$ S -wave phase shift of $\pi\pi$ scattering.

3.2 Chiral perturbation theory for Wilson-type fermions

Since the Wilson-type quarks explicitly break the chiral symmetry at finite lattice spacings, it is desirable to include its violation effect into ChPT. In this section, ChPT for Wilson-type fermions(WChPT) is introduced.

The effects of $O(a)$ breaking by the Wilson term were first introduced to ChPT in the study of spontaneous parity and flavor breaking phase in two-flavor full QCD [12]. The tree level WChPT Lagrangian including $O(a)$ contribution is constructed. Then, the pseudoscalar meson mass and decay constant formulae have been calculated at one-loop [13]. The extension to the partially quenched case was also discussed. Including $O(a^2)$ contribution was the next step. It has been done in the next-to-leading order Lagrangian [14] and in the tree level one [15]. We note that including $O(a^2)$ chiral breaking term in the tree level Lagrangian plays an essential role to generate the parity-flavor breaking phase transition, which is needed for the existence of the massless pions with the Wilson-type action [12]. Similar attempts to include the $O(a^2)$ taste violations for the KS-type fermion have been made. The taste refers to the degrees of freedom of the KS-type fermion resulting from the doubling problem. One-flavor chiral perturbation theory was first considered [16]. Then it has been extended to the multi-flavor case [17, 18].

Hereafter, we consider the one-loop formulae including $O(a^2)$ terms, which are needed to realize massless pions at $a \neq 0$ [15]. First the tree level WChPT formulae including $O(a^2)$ terms are calculated. Then the one-loop calculations are performed. Finally we discuss the resummation of the one-loop WChPT formulae.

For the tree level case, adding a , a^2 , $m_{quark}a$ and p^2a contributions to the naive ChPT Lagrangian at $O(p^2)$ in Eq. (3.12) leads to

$$\mathcal{L}_{WChPT}^{LO} = \mathcal{L}_{tree}^{(2)} = \frac{f^2}{4} \left(1 + c_0(S^0 - 1) \right) \text{Tr}(\partial_\mu U \partial^\mu U) + c_1 S^0 + c_2 (S^0)^2, \quad (3.51)$$

where S^0 is the scalar operator normalized the one in Eq. (3.30) and c_0 , c_1 and c_2 are defined as

$$c_0 = W_0 a, \quad (3.52)$$

$$c_1 = W_1 a + B_1 m_{quark}, \quad (3.53)$$

$$c_2 = W_2 a^2 + V_2 (m_{quark} a). \quad (3.54)$$

There are three notices. One is that $O(a^2)$ is uniquely given by $(S^0)^2$. Though one power of m_{quark} , $O(a)$ and $(O(a))^2$ is uniquely given by S^0 , not only $(S^0)^2$ but also $(P^a)^2$ and

$\text{Tr}(U + U^\dagger)^2$ can contribute to the Lagrangian. However, due to the feature of $N_f = 2$ case, $(P^a)^2$ and $\text{Tr}(U + U^\dagger)^2$ can be written in terms of $(S^0)^2$,

$$(P^a)^2 = (S^0)^2 - 1, \quad (3.55)$$

$$\text{Tr}(U + U^\dagger)^2 = 2(S^0)^2. \quad (3.56)$$

Another is that an independent term at $O(ap^2)$ is given uniquely by $S_0 \text{Tr}(\partial_\mu U \partial^\mu U^\dagger)$ because $\text{Tr}((U + U^\dagger) \partial_\mu U \partial^\mu U^\dagger) \propto S_0 \text{Tr}(\partial_\mu U \partial^\mu U^\dagger)$. The last one is that \mathcal{L}_{WChPT}^{LO} includes $(S^0 - 1)$ because the overall factor can be redefined. $(S^0 - 1)$ keeps the first +1.

From \mathcal{L}_{WChPT}^{LO} the operators in WChPT can be identified with those in lattice QCD as,

$$S_{lattice}^0 = Z_S S^0 (1 + c_S (S^0 - 1)), \quad (3.57)$$

$$P_{lattice}^a = Z_P P^a (1 + c_P (S^0 - 1)), \quad (3.58)$$

$$A_{lattice}^\mu = Z_A (A^\mu (1 + c_A (S^0 - 1))), \quad (3.59)$$

where $Z_{S,P,A}$ are dimensionless constants and $c_{S,P,A}$ and \tilde{c}_A are $O(a)$ in general.

Next we perform one-loop calculations. Expanding $\mathcal{L}_{1-loop}^{(2)}$ in powers of π lead to

$$\begin{aligned} \mathcal{L}_{1-loop}^{(2)} = & \text{const.} + \frac{1}{2} (\partial_\mu \pi \partial^\mu \pi + m_0^2 \pi^2) \\ & + \frac{1}{6f^2} \left((\pi \partial_\mu \pi)^2 - \left(1 + \frac{3}{2}c_0\right) (\partial_\mu \pi \partial^\mu \pi) \pi^2 \right) + \frac{8c_2 - c_1}{24f^4} (\pi^2)^2, \end{aligned} \quad (3.60)$$

where

$$m_0^2 = \frac{c_1 - 2c_2}{f^2}. \quad (3.61)$$

The operators $S_{lattice}^0$, $P_{lattice}^a$ and $A_{lattice}^\mu$ are also expanded as

$$S_{lattice}^0 = Z_S \left(1 - \frac{\pi^2}{2f^2} (1 + c_S) \right), \quad (3.62)$$

$$P_{lattice}^a = iZ_P \frac{\pi^a}{f} \left(1 - \frac{\pi^2}{6f^2} (1 + 3c_P) \right), \quad (3.63)$$

$$\begin{aligned} A_{lattice,a}^\mu = & iZ_A \left((1 + \tilde{c}_A) \frac{\partial_\mu \pi^a}{f} - \frac{2\partial_\mu \pi^a \pi^2}{3f^3} \left(1 + \frac{3c_A + \tilde{c}_A}{4} \right) \right. \\ & \left. + \frac{2\pi^a \pi \partial_\mu \pi}{3f^3} \left(1 - \frac{\tilde{c}_A}{2} \right) \right). \end{aligned} \quad (3.64)$$

To obtain the pion propagator at one-loop order, we calculate loop integrals. The pion propagator at the tree level is

$$\langle \pi^a(-p) \pi^b(p) \rangle = \delta^{ab} \frac{1}{p^2 + m_0^2}. \quad (3.65)$$

Then the loop integrals are evaluated as in the naive ChPT case,

$$\langle \pi^a(x) \pi^b(x) \rangle = \delta^{ab} \frac{m_0^2}{(4\pi)^2} \log \frac{m_0^2}{\Lambda^2} \equiv \delta^{ab} I, \quad (3.66)$$

$$\langle \partial_\mu \pi^a(x) \partial_\nu \pi^b(x) \rangle = \delta^{ab} \delta_{\mu\nu} \left(-\frac{m_0^2}{4} I \right), \quad (3.67)$$

where Λ is an arbitrary mass parameter in the $\overline{\text{MS}}$ scheme. We note that the value of Λ depends on physical observables. The inverse pion propagator at one-loop is calculated as

$$\begin{aligned} \mathcal{L}_{WChPT}^{NLO} &= \frac{1}{2} (\partial_\mu \pi)^2 \left(1 - \frac{I}{3f^2} \left(2 + \frac{9c_0}{2} \right) \right) + \frac{1}{2} \pi^2 \left(m_0^2 \left(1 - \frac{I}{6f^2} (1 - 9c_0) \right) + \frac{5c_2 I}{f^4} \right) \\ &= \frac{1}{2} \left((\partial_\mu \pi_R)^2 + m_\pi^2 \pi_R^2 \right), \end{aligned} \quad (3.68)$$

where

$$\pi = Z^{1/2} \pi_R \quad (3.69)$$

$$Z = \left(1 - \frac{I}{3f^2} \left(2 + \frac{9c_0}{2} \right) \right)^{-1} \quad (3.70)$$

$$m_\pi^2 = m_0^2 \left(1 + \frac{m_0^2}{32\pi^2 f^2} (1 + 6c_0) \log \frac{m_0^2}{\Lambda^2} + \frac{5c_2}{16\pi^2 f^4} \log \frac{m_0^2}{\Lambda^2} \right). \quad (3.71)$$

This Eq. (3.71) is the one-loop WChPT formula for m_π^2 . The formula for the decay constant f_π is obtained using the axial current operator $A_{lattice,a}^\mu$. The vacuum to pion matrix element of the axial current is given by

$$\begin{aligned} \langle A_{lattice,a}^\mu(x) \pi_R^b(y) \rangle &= \delta_{ab} \frac{iZ_A}{f} \langle \partial^\mu \pi_R^a(x) \pi_R^b(y) \rangle Z^{1/2} \\ &\quad \left((1 + \tilde{c}_A) - \frac{I}{3f^2} \left(4 + \frac{9c_A - 3\tilde{c}_A}{2} \right) \right) \end{aligned} \quad (3.72)$$

$$= ip^\mu f_\pi. \quad (3.73)$$

Therefore, taking $Z_A = i\sqrt{2}f^2$, we obtain

$$f_\pi = f(1 + \tilde{c}_A) \left(-\frac{m_0^2}{16\pi^2 f^2} (1 + c_{f_\pi}) \log \frac{m_0^2}{\Lambda^2} \right), \quad (3.74)$$

$$c_{f_\pi} = \frac{3}{2} c_A - \frac{11}{6} \tilde{c}_A - \frac{3}{4} c_0. \quad (3.75)$$

Similarly, the axial Ward identity quark mass m_{quark}^{AWI} is obtained by

$$m_{quark}^{AWI} = \frac{\langle \partial_\mu A_{lattice,a}^\mu(x) \pi_R^b(y) \rangle}{\langle P_{lattice}^a(x) \pi_R^b(y) \rangle}. \quad (3.76)$$

Using

$$\begin{aligned} \langle \partial_\mu A_{lattice,a}^\mu(x) \pi_R^b(y) \rangle &= \langle \pi_R^a(x) \pi_R^b(y) \rangle \sqrt{2} f m_\pi^2 Z^{1/2} \\ &\quad \left((1 + \tilde{c}_A) - \frac{I}{3f^2} \left(4 + \frac{9c_A - 3\tilde{c}_A}{2} \right) \right), \end{aligned} \quad (3.77)$$

$$\langle P_{lattice}^a(x) \pi_R^b(y) \rangle = i \frac{Z_P}{f} \langle \pi_R^a(x) \pi_R^b(y) \rangle Z^{1/2} \left(1 - \frac{5I}{6f^2} (1 + 3c_P) \right), \quad (3.78)$$

we have

$$m_{quark}^{AWI} = \frac{1 + \tilde{c}_A}{2B_0} m_0^2 \left(1 + \frac{m_0^2 c_{AWI} + 10c_2/f^2}{32\pi^2 f^2} \log \frac{m_0^2}{\Lambda^2} \right), \quad (3.79)$$

where

$$B_0 = \frac{iZ_P}{2\sqrt{2}f^2}, \quad (3.80)$$

$$c_{AWI} = 6c_0 - 3c_A + \frac{11}{3}\tilde{c}_A + 5c_P. \quad (3.81)$$

Let us recall the pion mass at tree level is written as

$$m_0^2 = \frac{c_1 - 2c_2}{f^2} = \frac{m_{quark}(B_1 - 2V_2a) + aW_1 - 2a^2W_2}{f^2} \equiv Am_R, \quad (3.82)$$

where

$$A \equiv \frac{B_1 - 2aV_2}{f^2}, \quad (3.83)$$

$$m_R \equiv m_{quark} - m_c, \quad (3.84)$$

$$m_c \equiv -a \frac{W_1 - 2aW_2}{B_1 - 2aV_2}. \quad (3.85)$$

We note that this m_c does not correspond to $1/(2\kappa_c)$ in lattice QCD, because $1/a$ contribution to the quark mass has been subtracted in m_{quark} . Another point is that c_2 controls the parity-flavor symmetry breaking. If $m < m_c$, m_0 becomes tachyonic, $m_0^2 < 0$. However, as long as $c_2 = O(a^2) > 0$, the parity-flavor symmetry breaking phase transition occurs such that $m_0^2 > 0$ [10].

We summarize the WChPT formulae for m_π , m_{quark}^{AWI} and f_π at one-loop as follows,

$$m_\pi^2 = Am_R \left(1 + \frac{(A + w_1^\pi a)m_R}{32\pi^2 f^2} \log \frac{Am_R}{\Lambda_{m_\pi}^2} + \frac{w_0 a^2}{32\pi^2 f^2} \log \frac{Am_R}{\Lambda_0^2} \right), \quad (3.86)$$

$$m_{quark}^{AWI} = A_0 m_R \left(1 + \frac{w_1^{AWI} a m_R}{32\pi^2 f^2} \log \frac{Am_R}{\Lambda_{AWI}^2} + \frac{w_0 a^2}{32\pi^2 f^2} \log \frac{Am_R}{\Lambda_0^2} \right), \quad (3.87)$$

$$f_\pi = f(1 + \tilde{c}_A) \left(1 - \frac{(A + w_1^{f_\pi} a)m_R}{16\pi^2 f^2} \log \frac{Am_R}{\Lambda_{f_\pi}^2} \right), \quad (3.88)$$

where we recover the labels of scale parameters Λ and w and A_0 are defined as

$$w_1^\pi \equiv 6W_0 + \frac{10V_2}{f^2}, \quad (3.89)$$

$$w_0 \equiv \frac{10}{f^2} \left(\frac{m_c V_2}{a} + W_2 \right), \quad (3.90)$$

$$w_1^{AWI} \equiv w_1 - 3W_A + \frac{11}{3}\tilde{W}_A + 5W_P, \quad (3.91)$$

$$w_1^{f\pi} \equiv \frac{3}{2}W_A - \frac{11}{6}\tilde{W}_A - \frac{3}{4}W_0, \quad (3.92)$$

$$A_0 = \frac{A(1 + \tilde{c}_A)}{2B_0}. \quad (3.93)$$

There are two features in these formulae. One is that in addition to the normal $m_R \log m_R$ chiral singularity, the $\log m_R$ contribution are generated by $O(a^2)$ effects. Another point is that m_{quark}^{AWI} has additional $m_R \log m_R$ and $\log m_R$ terms, which are not in the naive ChPT.

Since the contribution of $\log m_R$ in WChPT becomes larger and larger toward the chiral limit, we must perform a resummation on $\log m_R$. The direct resummation by calculating n -loop terms is possible in principle but is difficult in practice. Instead of the direct approach, we use the four dimensional scalar theory with complicated interactions that describes the parity-flavor phase transition. The phase transition has the meanfield critical exponent with possible logarithmic corrections. For the pion mass corresponding to the inverse of the correlation length, the behavior near the critical point should be

$$m_\pi^2 = C m_R \left(\log \left(\frac{m_R}{D} \right) \right)^{\nu'} + (\text{less singular terms}). \quad (3.94)$$

For the comparison with the WChPT formula, we expand it as

$$\begin{aligned} m_\pi^2 &= C m_R (X + Y)^{\nu'} \\ &= C m_R X^{\nu'} \left(1 + \nu' \frac{Y}{X} + \dots \right), \end{aligned} \quad (3.95)$$

where

$$X = \log \left(\frac{\Lambda_0^2}{AD} \right), \quad (3.96)$$

$$Y = \log \left(\frac{A m_R}{\Lambda_0} \right), \quad (3.97)$$

Comparing Eq. (3.95) with the WChPT formula of Eq. (3.86) leads to the identification

$$\frac{\nu'}{X} = \frac{a^2 w_0}{32\pi^2 f^2}, \quad (3.98)$$

$$C X^{\nu'} = A. \quad (3.99)$$

To determine ν' and X separately, the WChPT formula at two-loop level is needed. Finally we have the resummed formulae for m_π^2 and m_{quark}^{AWI} ,

$$m_\pi^2 = Am_R \left(\log \left(\frac{Am_R}{\Lambda_0^2} \right) \right)^{\frac{a^2 w_0}{32\pi^2 f^2}} \left(1 + \frac{(A + w_1^\pi a)m_R}{32\pi^2 f^2} \log \left(\frac{Am_R}{\Lambda_3^2} \right) \right) \quad (3.100)$$

$$m_{quark}^{AWI} = A_0 m_R \left(\log \left(\frac{Am_R}{\Lambda_0^2} \right) \right)^{\frac{a^2 w_0}{32\pi^2 f^2}} \left(1 + \frac{w_1^{AWI} a m_R}{32\pi^2 f^2} \log \left(\frac{Am_R}{\Lambda_{3,AWI}^2} \right) \right), \quad (3.101)$$

where A, Λ_0 and w_0 can be different from those in Eq. (3.86) and (3.87). We note that $\log m_R$ contribution does not appear in f_π and therefore f_π does not need the resummation.

Chapter 4

Previous simulation results in lattice QCD

In this chapter, the previous calculations in the quenched and two-flavor lattice QCD are reviewed, paying attention to the role of chiral extrapolations. In these previous cases, the chiral and continuum extrapolations have been done and the results are compared with experiments.

4.1 Quenched QCD

Since lattice QCD calculations need large computational resources, the quenched approximation ignoring the quark vacuum polarization effects was often used. In the quenched approximation, a precise calculation of light hadron spectrum has been done by the CP-PACS collaboration [29]. Simulations were made with the naive plaquette gauge and Wilson quark action on $32^3 \times 56 - 64^3 \times 112$ lattices at four values of lattice spacings $a \sim 0.1 - 0.05$ fm with the spatial size $L \sim 3$ fm. Hadronic observables were calculated at five quark masses corresponding to $m_{PS}/m_V = 0.75 - 0.40$. One of the major results of their work is the observation of quenched chiral singularities. They also showed the failure of the quenched approximation in the hadron spectrum and the strange quark mass.

The feature of the quenched light hadron spectrum is the appearance of the quenched chiral log singularity. Quenched chiral perturbation theory (QChPT) predicts that a characteristic logarithm singularity appears in the hadron mass as a function of quark mass m_{quark} [30,31]. For pseudoscalar mesons made of quarks with masses m_1 and m_2 , QChPT predicts

$$m_{PS}^2(m_1, m_2) = A(m_1 + m_2) \left(1 - \delta \left(\log \frac{2m_1 A}{\Lambda_{QChPT}^2} + \frac{m_2}{m_2 - m_1} \log \frac{m_2}{m_1} \right) \right)$$

$$\begin{aligned}
& + \frac{\alpha_\Phi A}{12\pi^2 f^2} \left(m_1 \log \frac{2m_1 A}{\Lambda_{QChPT}^2} + m_2 \log \frac{2m_2 A}{\Lambda_{QChPT}^2} + \frac{m_1 m_2}{m_2 - m_1} \log \frac{m_2}{m_1} \right) \\
& + B(m_1 + m_2)^2 + O(m^3, \delta^2).
\end{aligned} \tag{4.1}$$

$A, B, \delta, \alpha_\Phi$ and Λ_{QChPT} are constants determined by fits of lattice data.¹ The logarithmic term proportional to δ represents the leading quenched singularity. At the leading order in the $1/N_c$ expansion in terms of the number of colors N_c , δ is given by

$$\delta = \frac{m_{\eta'}^2 + m_\eta^2 - 2m_K^2}{48\pi^2 f^2}. \tag{4.2}$$

Using the experimental values for the pseudoscalar meson masses and the decay constant f of 93MeV, $\delta \sim 0.2$ is obtained as a phenomenological estimate. Λ_{QChPT} is a scale parameter of QChPT, estimated as $\Lambda_{QChPT} \sim O(1)$. α_Φ in Eq. (4.1) is a constant representing the coefficient of the kinetic term of the flavor-singlet meson field, which is subleading in terms of $1/N_c$. One of the fit results of m_{PS}^2 is shown in Fig. 4.1. Lattice data of m_{PS}^2 support the existence of the quenched singularity. The best estimate of δ from finer lattices is $\delta = 0.10(2)$, which is close to the phenomenological estimate $\delta \sim 0.2$.

Using the quenched ChPT formulae, the light hadrons are extrapolated to the physical point. Then after taking the continuum limit, the results are compared with experiments. The quenched light hadron spectrum in the continuum limit is displayed in Fig. 4.2. There are about 10% difference between the quenched results and the experimental data. Since the statistical errors are 1-3% and the systematic errors are 0-2%, the quenched approximation is the major source of this difference.

Another failure of the quenched approximation can be seen in the strange quark mass m_s . To determine the strange quark mass in lattice QCD, we need an input observable. The mass of kaon m_K or that of ϕ meson m_ϕ is used for this purpose. The obtained quark mass is expected to be independent of the choice of the input. However the result shows a systematic deviation.

$$m_s = 113.8(2.3)_{-2.9}^{+5.8}[\text{MeV}] \quad m_K \text{ input}, \tag{4.3}$$

$$m_s = 142.3(5.8)_0^{+5.8}[\text{MeV}] \quad m_\phi \text{ input}, \tag{4.4}$$

where the first error is statistical and the second error is systematic. The difference is clearly larger than the error. Therefore, this is again the quenching effect.

¹A modification of fitting parameters is needed because they are not independent in χ^2 fits.

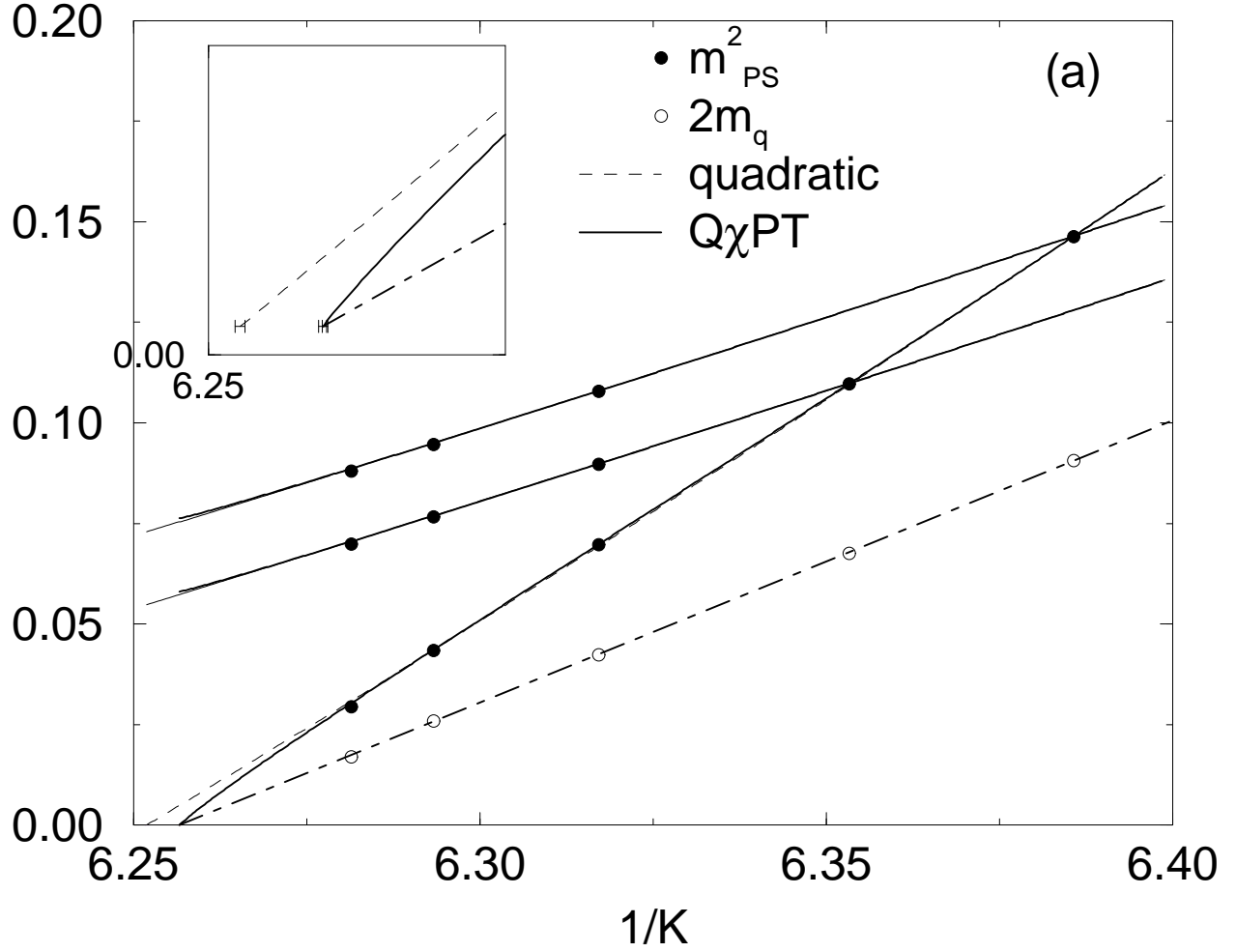


Figure 4.1: Chiral extrapolations for pseudoscalar meson masses at $\beta = 5.9$ with the quenched plaquette and Wilson quark action combination. The insets are expanded displays for the degenerate case. The QChPT and quadratic chiral fits are shown by solid and dashed line. AWI quark masses are used for m_q .

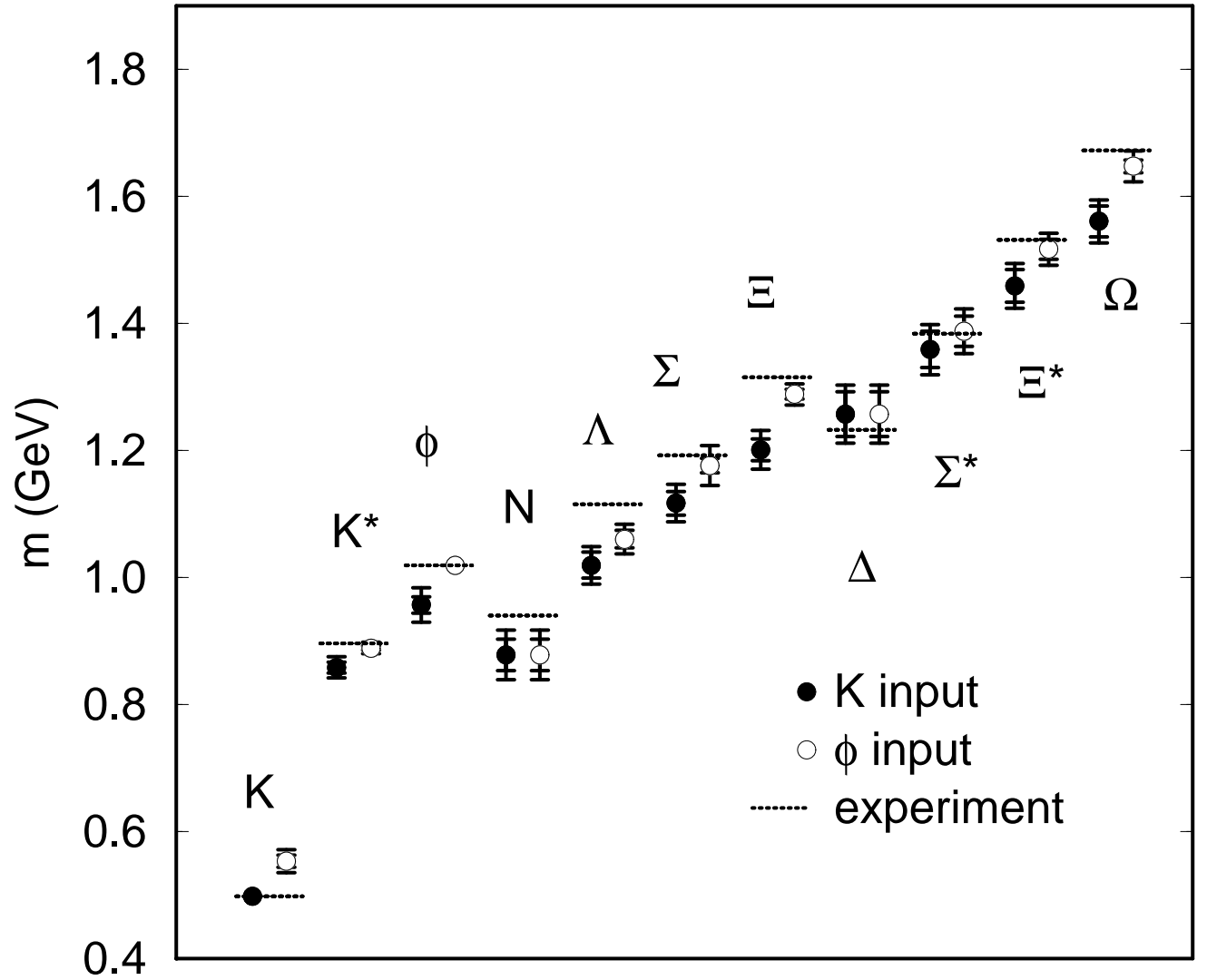


Figure 4.2: Quenched light hadron spectrum compared with experiment.

4.2 two-flavor full QCD

For the first step in full QCD, two-flavor simulations including dynamical up and down quarks with degenerate masses have performed. The CP-PACS collaboration made a first attempt toward execution of chiral and continuum extrapolations within a single set of simulations [20]. Simulations were made with the RG improved gauge and the meanfield-improved clover quark action on $12^3 \times 24 - 24^3 \times 48$ lattices at values of lattice spacings $a \sim 0.2 - 0.1$ fm with the spatial size $L \sim 2.5$ fm and four sea quark masses corresponding to $m_{PS}/m_V = 0.8 - 0.6$. Hadronic observables were calculated at five valence quark masses corresponding to $m_{PS}/m_V = 0.8 - 0.5$.

As in the quenched QCD, chiral perturbation theory(ChPT) predicts a characteristic logarithm in the hadron mass formulae. For a pseudoscalar meson in two-flavor($N_f = 2$) cases, ChPT predicts

$$\frac{m_{PS}^2}{2B_0 m_{quark}} = 1 + \frac{1}{N_f} \frac{2B_0 m_{quark}}{(4\pi f)^2} \log \frac{2B_0 m_{quark}}{\Lambda_3^2}, \quad (4.5)$$

$$f_{PS} = f \left(1 - \frac{N_f}{2} \frac{2B_0 m_{quark}}{(4\pi f)^2} \log \frac{2B_0 m_{quark}}{\Lambda_4^2} \right), \quad (4.6)$$

where B_0 is a constant, which is not determined in the context of ChPT. f is the pseudoscalar meson decay constant in the chiral limit and Λ_3 is a renormalization scale. In contrast to the case of the quenched QCD, however, the data do not show curvature of the chiral logarithm as shown in Fig 4.3. Therefore, instead of the ChPT formulae, polynomials of quark masses are used in their analysis.

$$m_{PS}^2 = B m_{quark} + C m_{quark}^2. \quad (4.7)$$

Then, after taking chiral and continuum extrapolations, the comparisons with experiments have been done. The major physics results are agreement of the $K^* - K$ hyperfine splitting with experiments and decrease of the light quark masses by 25% from those obtained in the quenched approximation.

In the quenched approximation, difference of the K^* meson mass from experiments was $2.6_{-0.9}^{+0.3}\%$ when the K meson mass is used to fix the strange quark mass. This difference is reduced to $0.7_{-1.7}^{+1.1}\%$ in full QCD. Similarly, when the ϕ meson mass is used as an input, difference of the K^* meson mass from experiments is under 1% for both quenched and full QCD, that of the K meson mass is reduced from $8.5_{-3.8}^{+1.6}\%$ in quenched QCD to $1.3_{-5.3}^{+5.3}\%$ in full QCD. The results are summarized in Fig. 4.4.

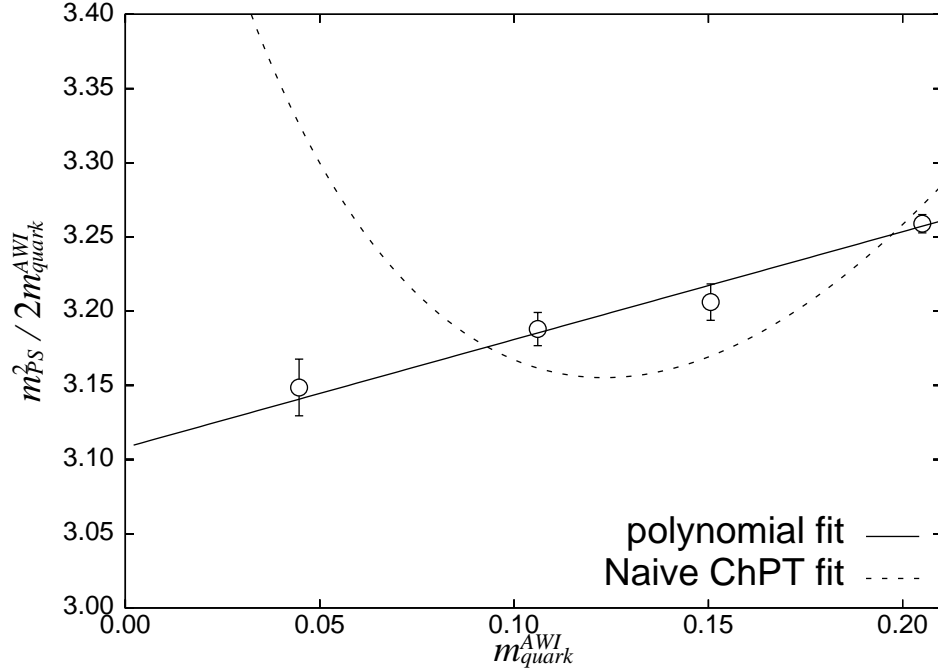


Figure 4.3: A test of the chiral logarithmic singularity in quark mass dependence of pseudoscalar meson masses on $12^3 \times 24$ lattices at $\beta = 1.80$. Quark masses defined by the axial vector Ward identity are used in this plot.

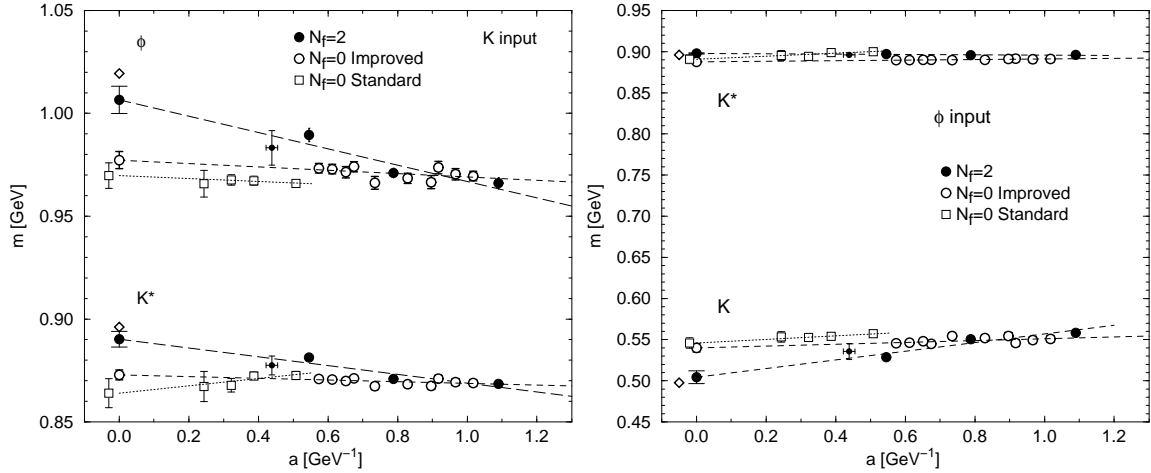


Figure 4.4: Comparison of meson masses in full and quenched QCD as functions of the lattice spacing a . Masses in the left figure have been obtained using the K meson mass as an input, while in the right figure the ϕ meson mass is used. Experimental values are indicated in diamonds. Data from the additional full QCD run at $\beta = 2.2$ are shown with small filled circles.

For light quark masses in the quenched QCD, $m_{ud}^{\overline{\text{MS}}} = 4.29(14)_{-0.79}^{+0.51}$ MeV and $m_s^{\overline{\text{MS}}} = 113.8(2.3)_{-2.9}^{+5.8}$ MeV from m_K and $m_s^{\overline{\text{MS}}} = 142.3(5.8)_{-0}^{+22.0}$ MeV from m_ϕ were obtained. m_s depended on the strange meson mass chosen for input. On the other hand, in full QCD, the light quark masses are $m_{ud}^{\overline{\text{MS}}} = 3.45_{-0.20}^{+0.14}$ MeV and $m_s^{\overline{\text{MS}}} = 89_{-6}^{+3}$ MeV from m_K and $m_s^{\overline{\text{MS}}} = 90_{-10}^{+5}$ MeV from m_ϕ . They are reduced by approximately 25% compared with the values in the quenched QCD. In addition, the input dependence of m_s vanishes in full QCD within errors, as described in Fig. 4.5.

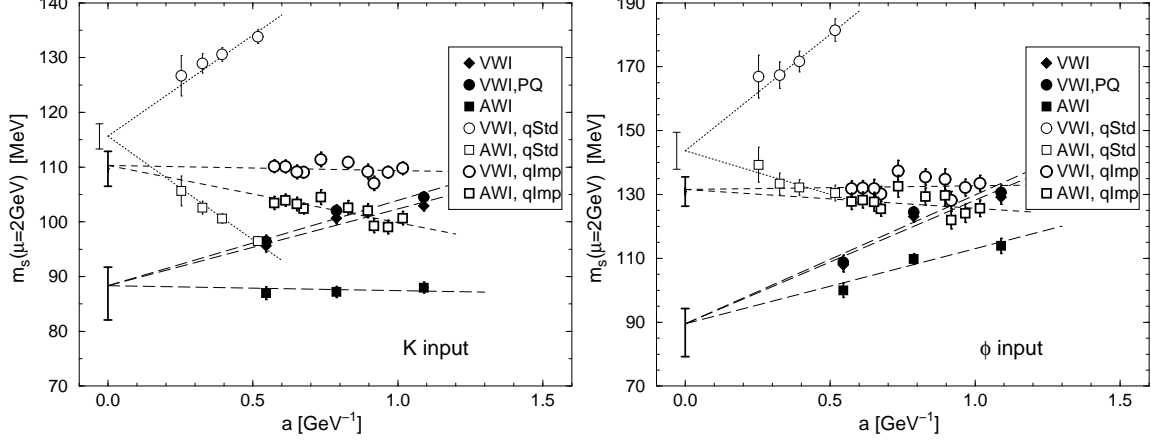


Figure 4.5: Comparison of strange quark masses in full and quenched QCD as functions of the lattice spacing a . Lines are from combined linear continuum extrapolations. Masses in the left figure have been obtained using the K meson mass as an input, while in the right figure the ϕ meson mass is used.

Chapter 5

Simulations

The following chapters are based on our original works. In this chapter, details of our simulations are presented. After explaining our simulation setup, the features of small sea quark mass simulations are discussed.

5.1 Simulation parameters and algorithm

Though the chiral and continuum limit has been taken for two-flavor full QCD as explained in the previous chapter, a subtle point is in the chiral extrapolation. Due to the large computational cost for full QCD simulations, the sea quark masses in the previous study were restricted in rather heavy region corresponding to $m_{PS}/m_V = 0.80 - 0.55$, larger than the ratio in the real world $m_\pi/m_\rho = 0.17$ by more than three times. The long extrapolation to the physical u and d quark masses may cause large systematic errors in the simulation results.

We have pushed two-flavor full QCD simulations with more realistic sea quark masses. Since the computational costs toward the chiral limit are huge, we use a coarse lattice. Therefore, to reduce the effects of a finite lattice spacing, we use an improved gauge and quark action. For the gauge part we employ the RG improved action defined by

$$S_g = \frac{\beta}{6} \left\{ c_0 \sum_{x,\mu,\nu} W_{\mu\nu}^{1 \times 1}(x) + c_1 \sum_{x,\mu,\nu} W_{\mu\nu}^{1 \times 2}(x) \right\}. \quad (5.1)$$

The coefficient $c_1 = -0.331$ of the 1×2 Wilson loop $W_{\mu\nu}^{1 \times 2}$ is fixed by an approximate renormalization group analysis [24], and $c_0 = 1 - 8c_1 = 3.648$ of the 1×1 Wilson loop by the normalization condition, which defines the bare coupling $\beta = 6/g^2$. For the quark part we use the clover quark action [25] defined by

$$S_q = \sum_{x,y} \bar{q}_x D_{x,y} q_y, \quad (5.2)$$

$$\begin{aligned}
D_{x,y} = & \delta_{xy} - \kappa \sum_{\mu} \left\{ (1 - \gamma_{\mu}) U_{x,\mu} \delta_{x+\hat{\mu},y} + (1 + \gamma_{\mu}) U_{x,\mu}^{\dagger} \delta_{x,y+\hat{\mu}} \right\} \\
& - \delta_{xy} c_{SW} \kappa \sum_{\mu < \nu} \sigma_{\mu\nu} F_{\mu\nu},
\end{aligned} \tag{5.3}$$

where κ is the hopping parameter and $F_{\mu\nu}$ the standard clover-shaped lattice discretization of the field strength. For the clover coefficient c_{SW} we adopt a mean field improved value [26]

$$c_{SW} = \left(W^{1 \times 1} \right)^{-3/4} = \left(1 - 0.8412 \beta^{-1} \right)^{-3/4}, \tag{5.4}$$

where the plaquette value $W^{1 \times 1}$ is calculated in the one-loop perturbation theory [24]. This choice is based on our observation in Ref. [32] that the one-loop calculation reproduces the measured values well.

Our simulations are performed at a single value of $\beta = 1.8$. The lattice spacing fixed from m_{ρ} at the physical sea quark mass is found to be 0.2007(38) fm. We adopt four values of the sea quark mass corresponding to the hopping parameter $\kappa_{sea} = 0.14585, 0.14660, 0.14705$ and 0.14720. This choice covers $m_{PS}/m_V = 0.35 - 0.60$. Gauge configurations are generated using the Hybrid Monte Carlo (HMC) algorithm [33, 34]. The trajectory length in each HMC step is fixed to the unity. We use the conventional leap-frog integration scheme for the molecular dynamics equation.

We accumulate 4000 HMC trajectories at $\kappa_{sea} = 0.14585, 0.14660$ and 0.14705 and 1400 trajectories at $\kappa_{sea} = 0.14720$ on the $12^3 \times 24$ lattice. We also accumulate 2000 trajectories at $\kappa_{sea} = 0.14585$ and 0.14660 on the $16^3 \times 24$ lattice. The simulation parameters are summarized in Table 5.1.

5.2 Stability of BiCGStab(L) method

In HMC, inversed quark matrices are needed. The even/odd preconditioned BiCGStab algorithm is often used for the quark matrix inversion to solve the equation $D_{xy} G_y = B_x$ [35]. However, the BiCGStab algorithm sometimes fails to converge at small quark masses. While the CG algorithm is guaranteed to converge, it is time-consuming. We find that an extension of BiCGStab to L -th order minimal residual polynomials, the BiCGStab(L) algorithm [36] is more stable [37]. Fig 5.1 is an example of the convergences of each algorithms. Though the conventional BiCGStab, corresponding to the case $L = 1$, and BiCGStab($L = 2$) do not converge, BiCGStab($L \geq 4$) converge well. The naive expectation from this result is that a larger L leads to a better convergence. In practice, however, too large L also frequently introduces another instability. The optimum value of

$12^3 \times 24$							
κ_{sea}	0.14585		0.14660		0.14705		0.14720
#MD	200		333	400	800	1000	1250 1600
Accept.	0.76		0.72	0.84	0.82	0.90	0.87 0.91
N_{traj}	4000		1750	2250	680	3320	100 1300
Stop.	10^{-10}		10^{-11}		10^{-11}		10^{-12}
N_{inv}	88		138		222		322
m_{PS}/m_V	0.600(3)		0.504(6)		0.411(11)		0.341(31)
$16^3 \times 24$							
κ_{sea}	0.14585		0.14660		0.14705		0.14720
#MD	200	250	333	500	—		—
Accept.	0.61	0.71	0.79	0.80	—		—
N_{traj}	800	1200	325	1675	—		—
Stop.	10^{-10}		10^{-11}		—		—
N_{inv}	87		163		—		—
m_{PS}/m_V	0.598(5)		0.522(6)		—		—

Table 5.1: Run parameters in simulations. The step size dt is given by the inverse of the number of the molecular dynamics steps (#MD). We denote the tolerance parameter in the stopping condition for the quark matrix inversion in calculations of the force by Stop. The number of trajectory is denoted by N_{traj} .

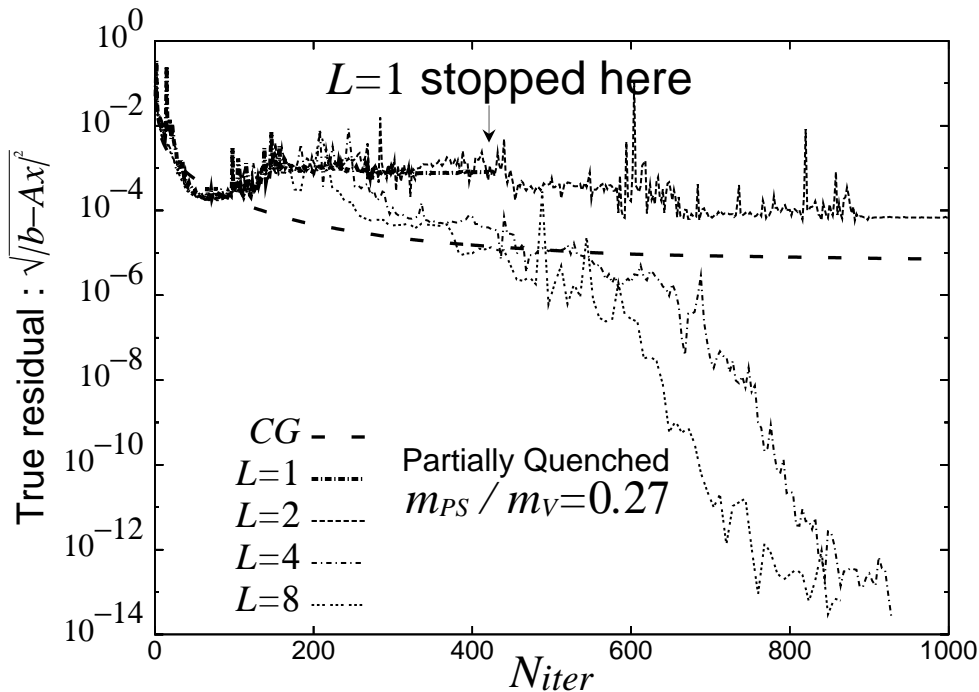


Figure 5.1: Convergences of several inversion algorithms.

L depends on simulation parameters. To avoid a tuning of L at each simulation point, we employ the BiCGStab(DS- L) algorithm [38]. This is an improvement of BiCGStab(L) in which an optimum L is dynamically selected. We find that BiCGStab(DS- L) is much more robust than the original BiCGStab at small quark masses without much increase of the computer time. The comparison of the CPU times is plotted in Fig. 5.2. BiCGStab(DS- L) shows a good efficiency in the wide range.

We take the stopping condition of the form $\|DG - B\| < \Delta$ in the HMC program. The value of Δ in the evaluation of the fermionic force is determined so that the reversibility over unit length is satisfied to a relative level better than 10^{-8} for the Hamiltonian. We use a stricter stopping condition in the calculation of the Hamiltonian in the Metropolis accept/reject test. Table 5.1 shows our choice of Δ together with the average number of the BiCGStab(DS- L) iteration in the quark matrix inversion for the force calculation, N_{inv} .

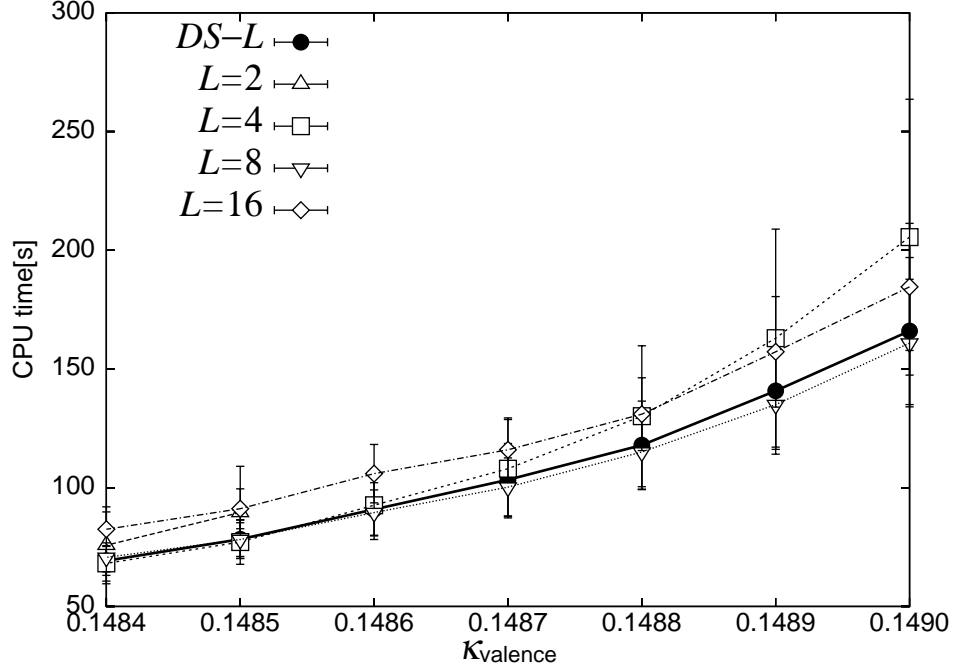


Figure 5.2: Comparison of the CPU time of inversion algorithms at different valence hopping parameters.

5.3 Spike

When we generate configurations by the HMC algorithm, we sometimes encountered huge values of $\Delta H \equiv H_{\text{trial}} - H_{\text{old}}$, the difference of the trial and starting hamiltonians as in the cases of other simulations [39]. We call these huge ΔH as spikes. A typical example of spikes is shown in Fig. 5.3. The abnormality of spikes can be also seen in the histogram of $\exp(-\Delta H)$ shown in Fig. 5.4. We note that if spikes do not appear, HMC gives $\langle \exp(-\Delta H) \rangle = 1$. Spikes distorts the distribution of $\exp(-\Delta H)$.

The practical problem of the spikes is that the simulations are more expensive at small sea quark masses. As the sea quark masses become smaller, more frequently huge ΔH appear. We must take a smaller value of the step size to keep the acceptance toward the chiral limit. But the additional decrease of the acceptance by huge ΔH requires more smaller step sizes. We found that the number of these spikes decreases more when we employ smaller step sizes as shown in the histogram of Fig. 5.4. A concrete example is shown in Fig. 5.5. Therefore to avoid the additional decrease of the efficiency by spikes we employ rather small step sizes for small sea quark mass cases such that the acceptance becomes approximately 90%, which is usually 70 – 80%.

These huge ΔH are expected to come from hyperbolicity of a leapfrog step of the molecular dynamics in HMC [40]. The solution to this spike problem is still under investigation.

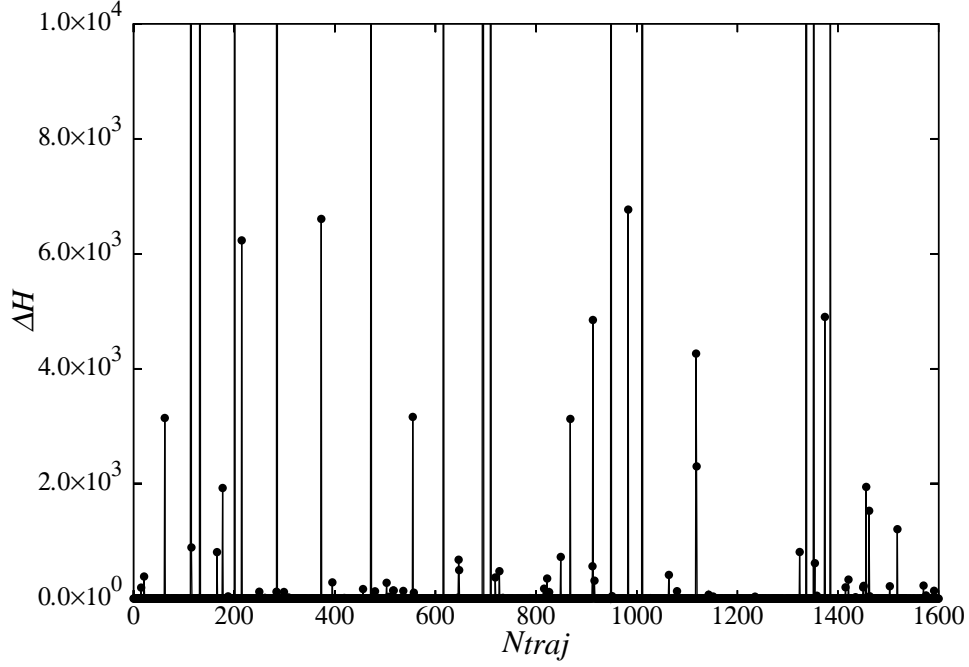


Figure 5.3: Huge ΔH (spikes) in the HMC trajectory at $\beta = 1.80, \kappa_{sea} = 0.14660$ with the step size $dt = 0.003$. We note that for the system with the spacetime volume V , $\langle \Delta H \rangle \sim O((dt)^4 V) \sim O(1)$.

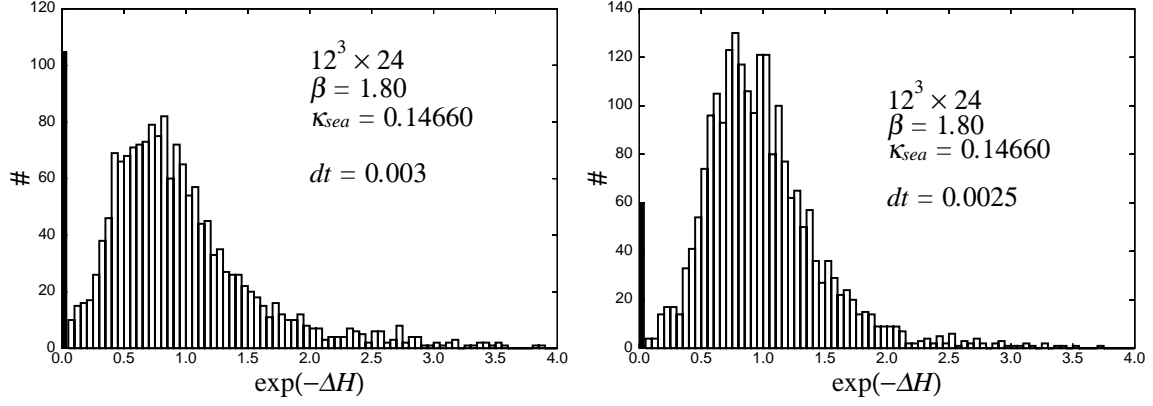


Figure 5.4: Histogram of $\exp(-\Delta H)$ at $\beta = 1.80, \kappa_{sea} = 0.14660$ with the step size $dt = 0.003$ and $dt = 0.0025$. The peak at $\exp(-\Delta H) = 0$ shows the contribution of spikes.

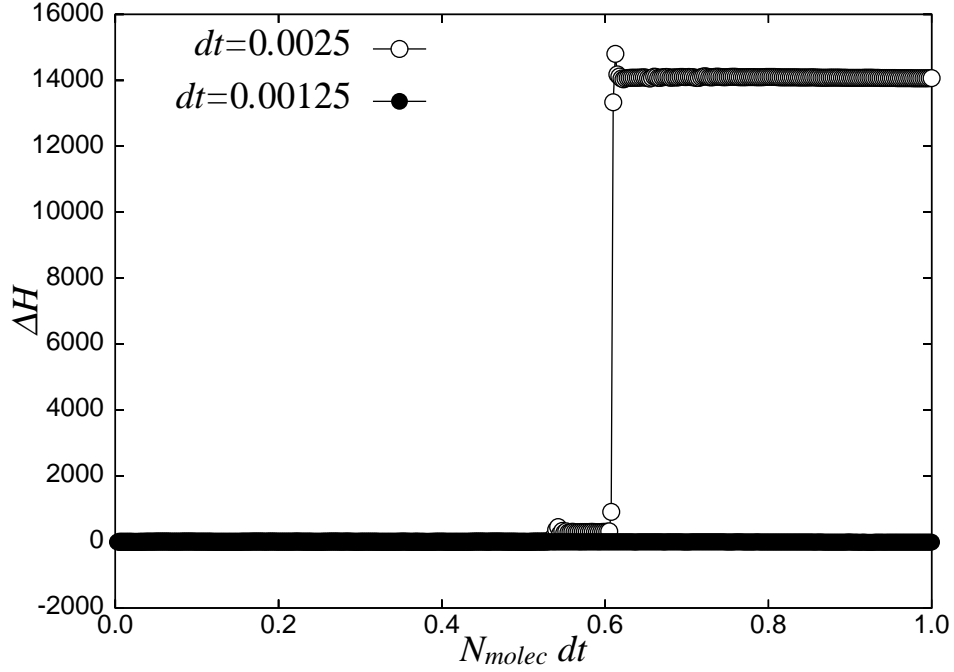


Figure 5.5: Huge ΔH (spike) in the molecular dynamics steps in HMC at $\beta = 1.80, \kappa_{sea} = 0.14660$ with the step size $dt = 0.0025$ and $dt = 0.00125$. The spike appear in the case of $dt = 0.0025$ but it does not in the case of $dt = 0.00125$.

Chapter 6

Results at simulation points

In this chapter, the measured observables such as hadron masses, decay constants and static potential are explained. Then autocorrelations and finite size effects of the observables are examined.

6.1 Hadron spectrum

For measurements in full QCD, we use four values of the sea quark mass corresponding to the hopping parameter $\kappa = 0.14585, 0.14660, 0.14705$ and 0.14720 which cover the range of $m_{PS}/m_V \simeq 0.60 - 0.35$. Measurements of light hadron masses and the static quark potential are carried out at every 5 trajectories. Details of the measurement methods are described in the appendix A. Their errors are estimated by the Jackknife method, which are shown in the appendix B.

We use the same operators and smearing functions as those in our previous study [20]. For each configuration quark propagators are calculated with a point source and a smeared source. For the smeared source, we fix the gauge configuration to the Coulomb gauge and use an exponential smearing function $\psi(r) = A \exp(-Br)$ for $r > 0$ with $\psi(0) = 1$. We chose $A = 1.25$ and $B = 0.50$.

Figures 6.1, 6.2 show typical examples of effective mass plots. Good plateau of the effective mass is obtained from hadron correlators with the point sink and the doubly smeared source for mesons and the triply smeared one for baryons. Hadron masses are extracted from these types of correlators.

We carry out χ^2 fits to hadron correlators, taking account of correlations among different time slices. A single hyperbolic cosine form is assumed for mesons, and a single exponential form for baryons. We set the lower cut of the fit range as $t_{min} = 6$ for mesons

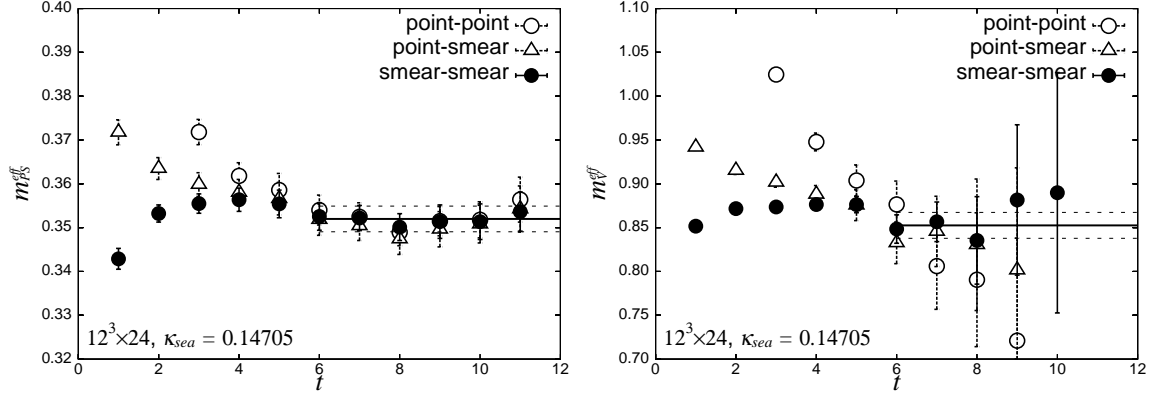


Figure 6.1: Effective masses of a pseudoscalar (left figure) and a vector meson (right figure) at $\kappa_{sea} = 0.14705$ on $12^3 \times 24$ lattice.

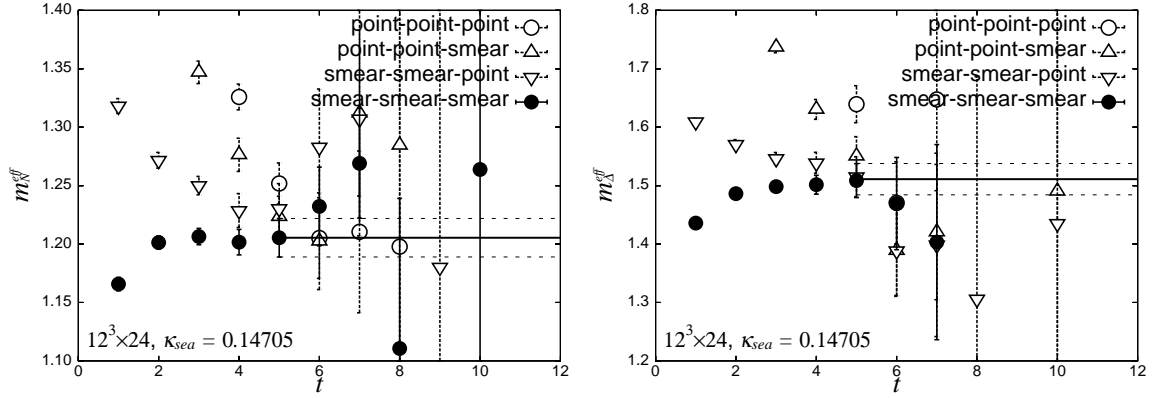


Figure 6.2: Effective masses of an octet baryon (left figure) and a decuplet baryon (right figure) at $\kappa_{sea} = 0.14705$ on $12^3 \times 24$ lattice.

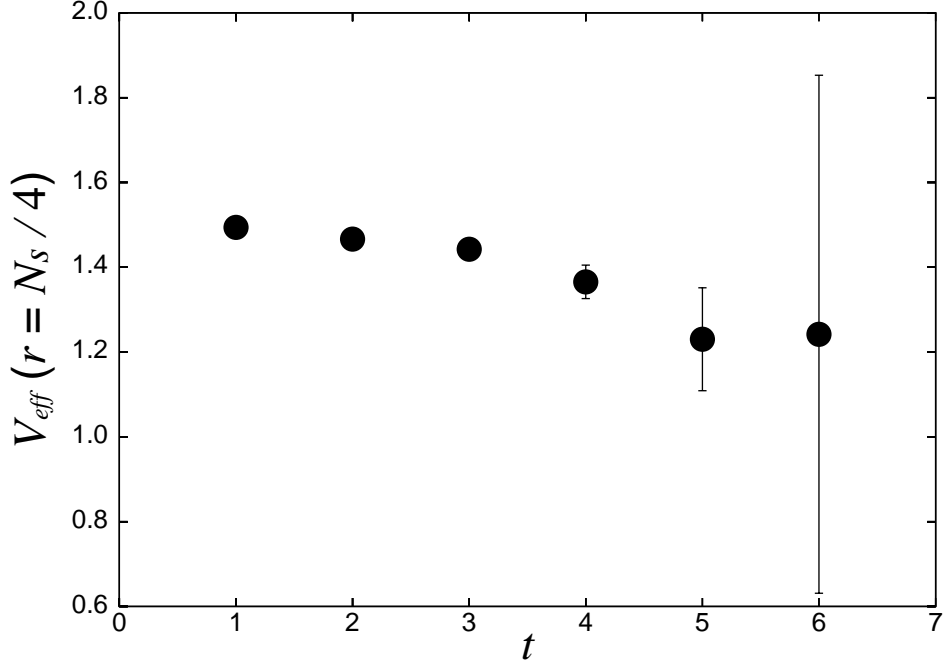


Figure 6.3: Effective potential energies $V_{eff}(r = N_s/4, t)$ at $\kappa_{sea} = 0.14705$ on $12^3 \times 24$ lattice.

and $t_{min} = 5$ for baryons, which is determined by inspecting stability of the fitted mass. The upper cut (t_{max}) dependence of the fit results is small and, therefore, we fix t_{max} to $N_t/2$ for all hadrons. Our choice of fit ranges and result of hadron masses are summarized in Tables D.1–D.9 in Appendix D. Statistical errors of hadron masses are estimated with the jack-knife procedure. We adopt the bin size of 100 trajectories by the bin size dependence of the jack-knife error as discussed below in Sec. 6.2.

The number of smearing steps for static potentials is fixed to its optimum value $N_{opt} = 3$ at which the overlap to the ground state $C(r)$ takes the largest value. We use $r = N_s/4$ as a reference. We inspect the t dependence of the effective potential $V_{eff}(r, t)$ defined in Eq. (A.19). Examples of V_{eff} are plotted in Fig. 6.3. We determine the lower cut of t as $t_{min} = 2$ by the plateau of V_{eff} . As shown in Fig. 6.4, we do not observe any clear indication of the string breaking. Therefore, we perform a correlated fit to $V(r) = V_{eff}(r, t_{min})$

The lower cut of the fit range in Eq. (A.20), is determined as $r_{min} = \sqrt{2}$ by the r_{min} dependence of r_0 . With $r_{min} < \sqrt{2}$, χ^2/dof takes an unacceptably large value, while α becomes ill-determined with $r_{min} > \sqrt{3}$. On the other hand, the r_{max} dependence of r_0 is mild. We fix r_{max} to $N_s/2$.

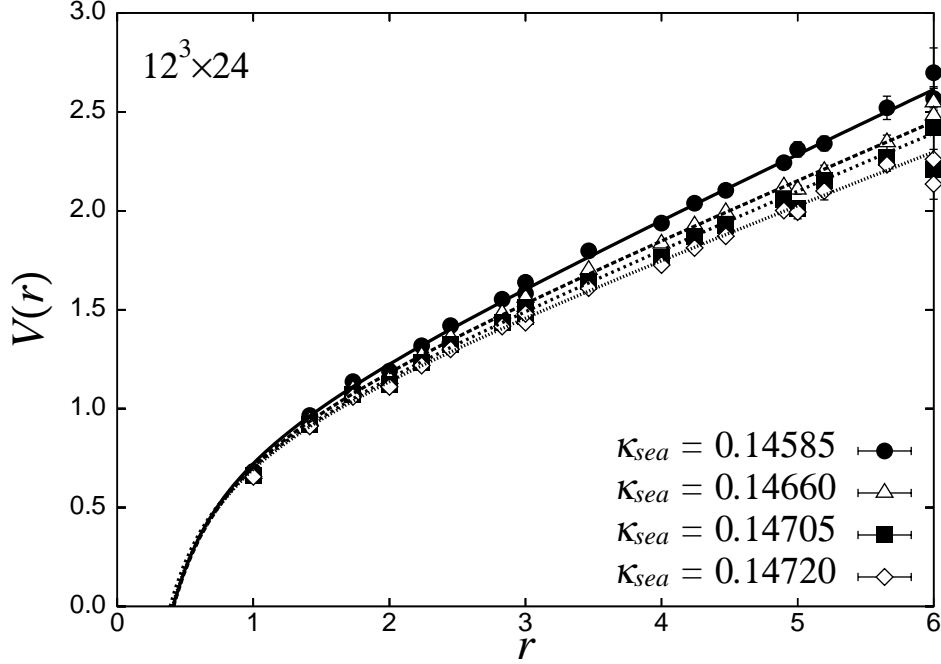


Figure 6.4: Static quark potentials at $\kappa_{sea} = 0.14585, 0.14660, 0.14705$ and 0.14720 corresponds to $m_{PS}/m_V = 0.60, 0.50, 0.40$ and 0.35 on $12^3 \times 24$ lattice.

The systematic errors of σ and r_0 due to the choice of t_{min} and r_{min} are evaluated. We repeat the fit, Eq. (A.22), with other choices of the range: $t_{min} = 3$ or $r_{min} = \sqrt{3}$. The deviations of fit parameters and r_0 are included into their systematic errors. Other systematic errors due to the choice of the optimum number of the smearing steps and r_{max} are small and ignored. Fit parameters in Eq. (A.20) and r_0 are summarized in Table D.11.

6.2 Autocorrelation

The autocorrelation in our full QCD data is studied by calculating the cumulative autocorrelation time of τ_O^{cum} for (i) the plaquette which is measured at every trajectory, (ii) the pseudoscalar meson propagators at $t = N_t/4$, (iii) the temporal Wilson loop with $(r, t) = (2, 2)$. We take $\Delta t_{max} = 50$ as shown in Fig. 6.5. In contrast to the naive expectation, our autocorrelation times of (i)-(iii) do not show clear sea quark mass dependence as seen in Fig. 6.6. One possible reason is that our statistics are not enough to estimate the autocorrelation times. Further studies are needed to draw a definite conclusion. Our results of τ_O^{cum} are summarized in Table 6.1.

Bin size dependences of the jack-knife errors of hadron masses and Wilson loops are

$12^3 \times 24$				
κ_{sea}	0.14585	0.14660	0.14705	0.14720
τ_{plaq}^{cum}	7.6(1.8)	11.7(2.3)	9.5(2.1)	8.9(3.2)
τ_{PS}^{cum}	7.9(1.6)	7.2(1.5)	5.3(1.2)	3.0(1.0)
τ_W^{cum}	8.1(1.9)	12.6(2.9)	11.3(2.2)	13.0(4.4)
$16^3 \times 24$				
κ_{sea}	0.14585	0.14660	0.14705	0.14720
τ_{plaq}^{cum}	14.1(3.9)	8.8(2.1)	—	—
τ_{PS}^{cum}	10.3(2.8)	4.9(1.6)	—	—
τ_W^{cum}	14.1(3.8)	10.1(4.3)	—	—

Table 6.1: Autocorrelation time for a plaquette (τ_{plaq}^{cum}), a pseudoscalar meson propagator at $N_t/4(\tau_{PS}^{cum})$ and a Wilson loop with $(r, t) = (2, 2)$ (τ_W^{cum}). All values are in units of a HMC trajectory.

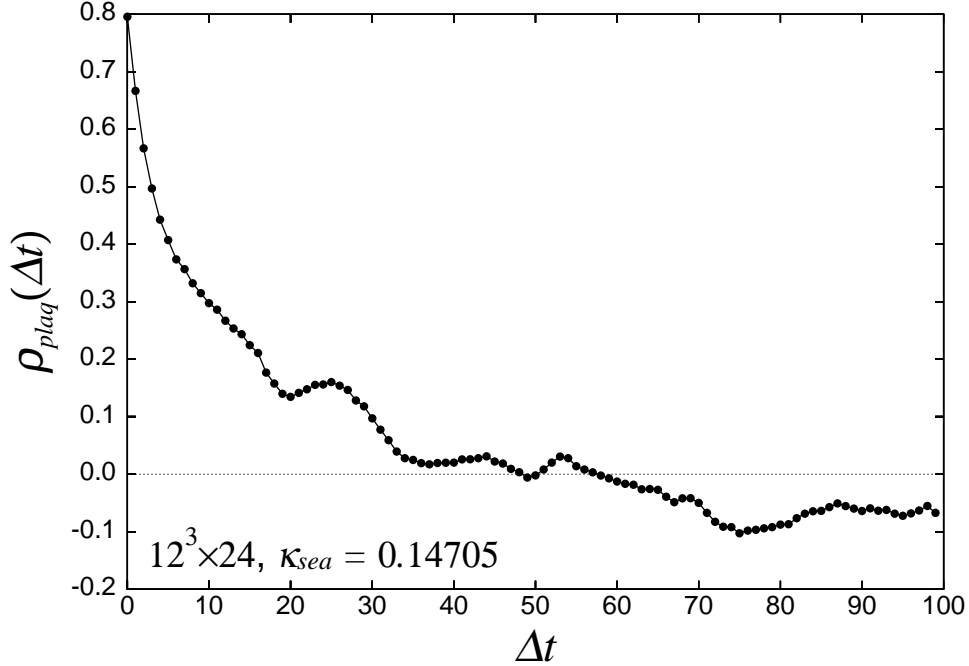


Figure 6.5: Autocorrelation function of a plaquette at $\kappa_{sea} = 0.14705$ on $12^3 \times 24$ lattice.

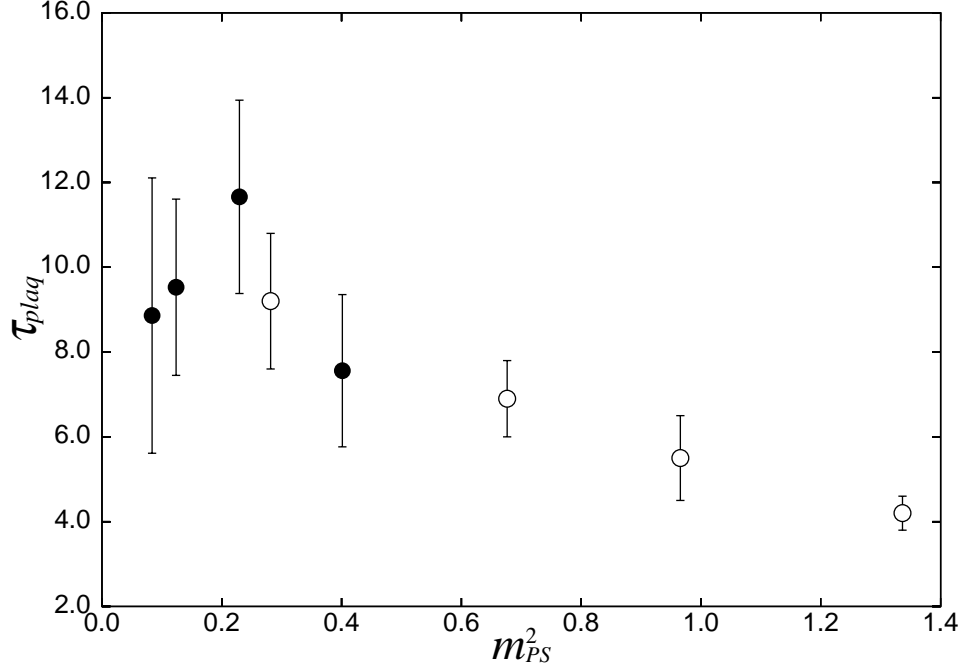


Figure 6.6: Sea quark mass dependence of the cumulative autocorrelation time of a plaquette on $12^3 \times 24$ lattice.

plotted in Figs. 6.7 and 6.8. For hadron masses and the static potential, the jack-knife errors reach plateaus at bin size of 50–100 trajectories. The situation is similar on $16^3 \times 24$. Therefore, we take the bin size of 100 trajectories in the error analysis.

6.3 Finite size effects

We discuss the finite size effect in our data on the $12^3 \times 24$ and $16^3 \times 24$ lattices, which correspond to $L \simeq 2.4 - 3.2$ fm,

In Fig. 6.9, 6.10, we plot our data of meson and AWI quark masses as a function of the spatial volume. For quantities in the meson sector, results obtained on $12^3 \times 24$ and $16^3 \times 24$ lattices are consistent within errors.

Finite size effects are expected to be more pronounced for baryon masses. Our data of the light baryon masses m_N and m_Δ at $m_{PS}/m_V = 0.50$ decrease by 1-3% ($0.8-2.3\sigma$) as shown in Fig. 6.11. A higher statistics is needed to draw more definite conclusions.

Finite size effects in r_0 are known to be much smaller than in hadron masses. Our results shown in Fig 6.12 confirm this.

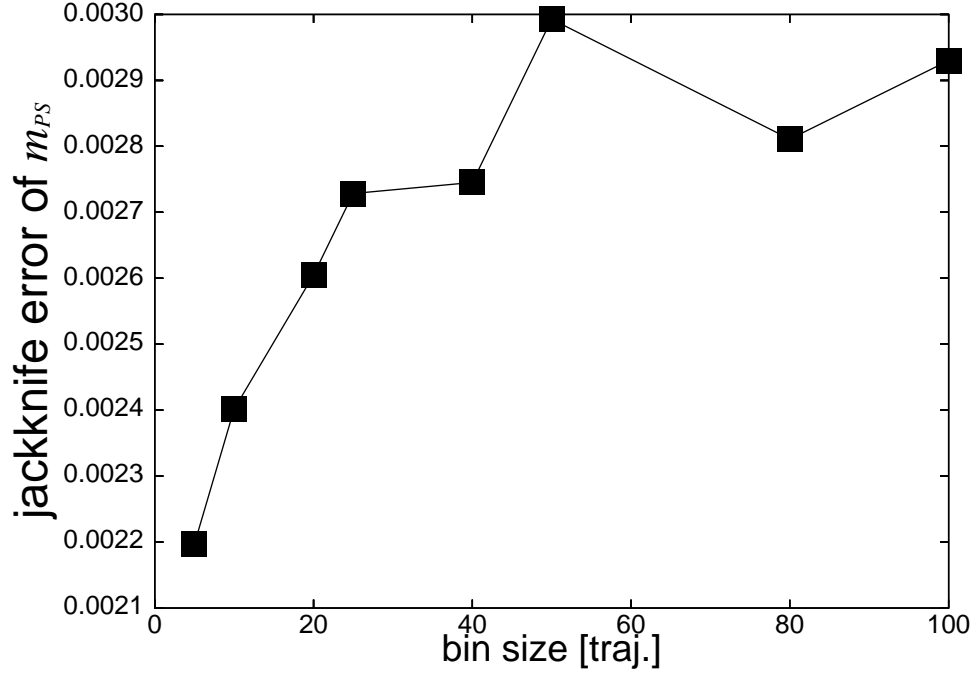


Figure 6.7: Bin size dependence of a jack-knife error of a pseudoscalar meson mass at $\kappa_{sea} = 0.14705$ on $12^3 \times 24$ lattice.

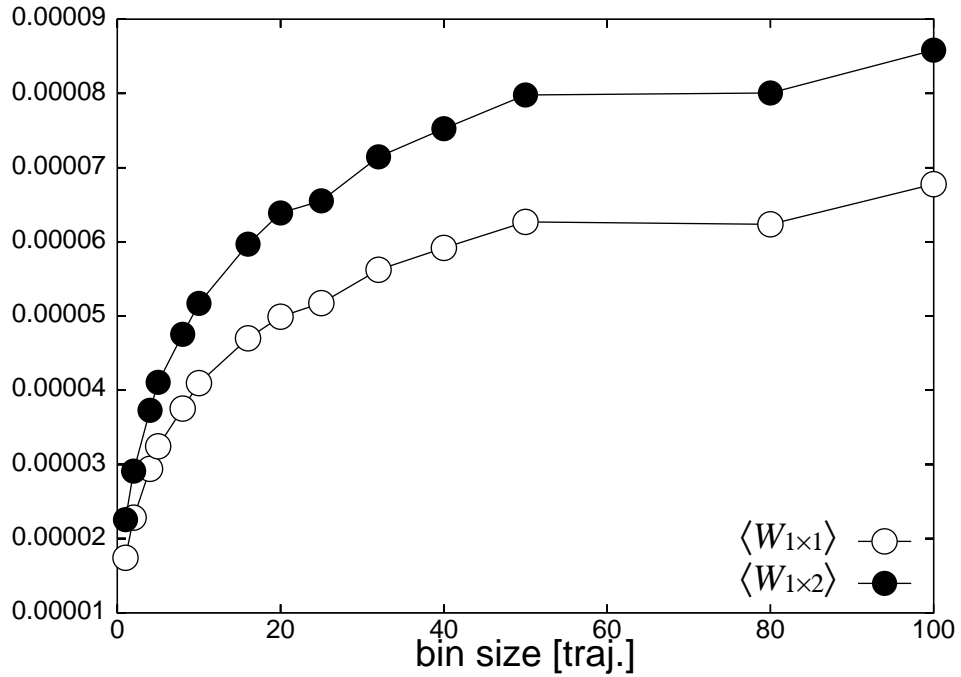


Figure 6.8: Bin size dependence of jack-knife errors of a plaquette and a rectangular loop at $\kappa_{sea} = 0.14705$ on $12^3 \times 24$ lattice.

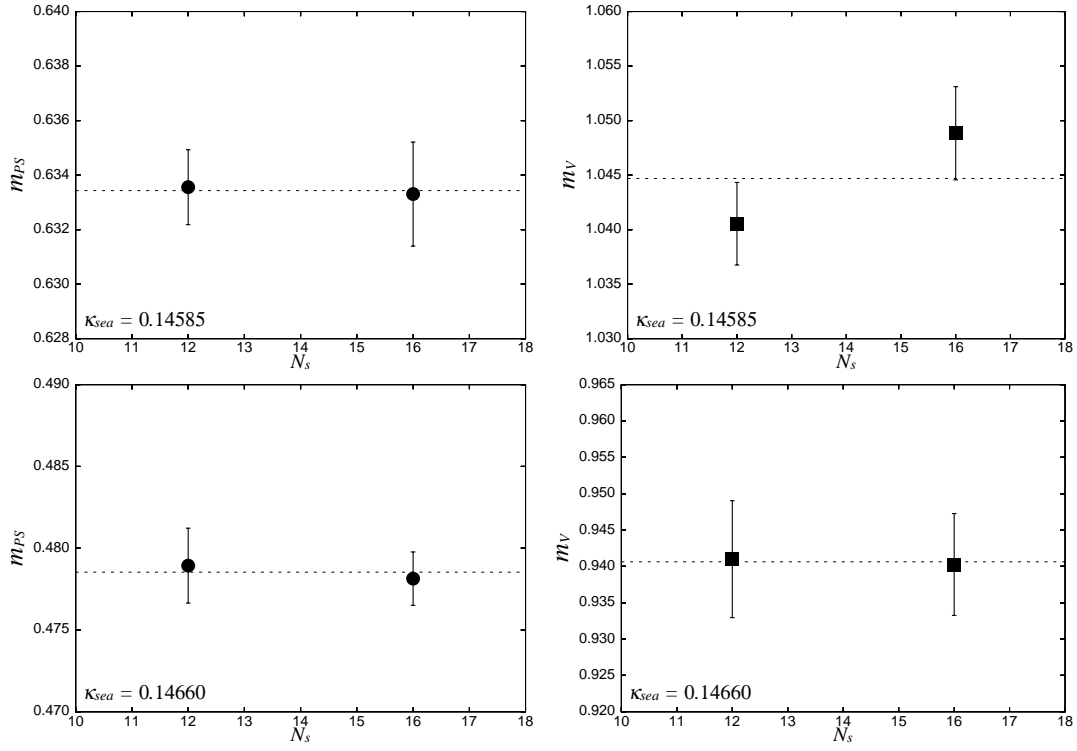


Figure 6.9: Volume dependence of pseudoscalar (left figure) and vector meson masses (right figure).

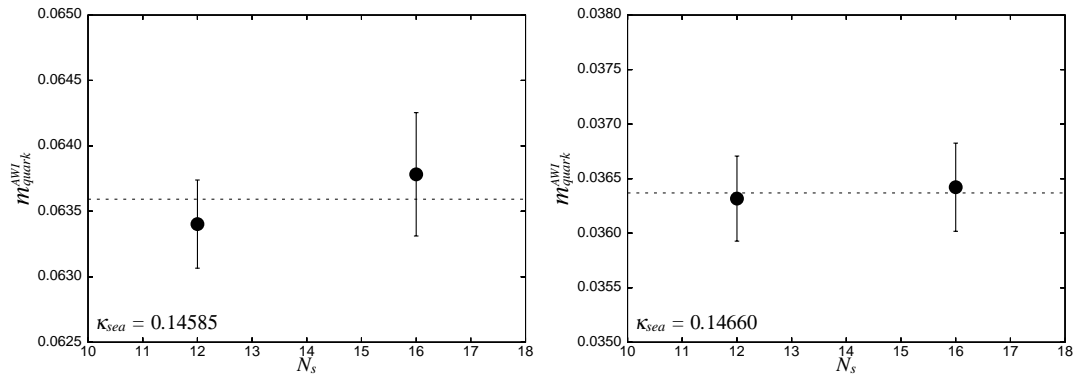


Figure 6.10: Volume dependence of AWI quark masses.

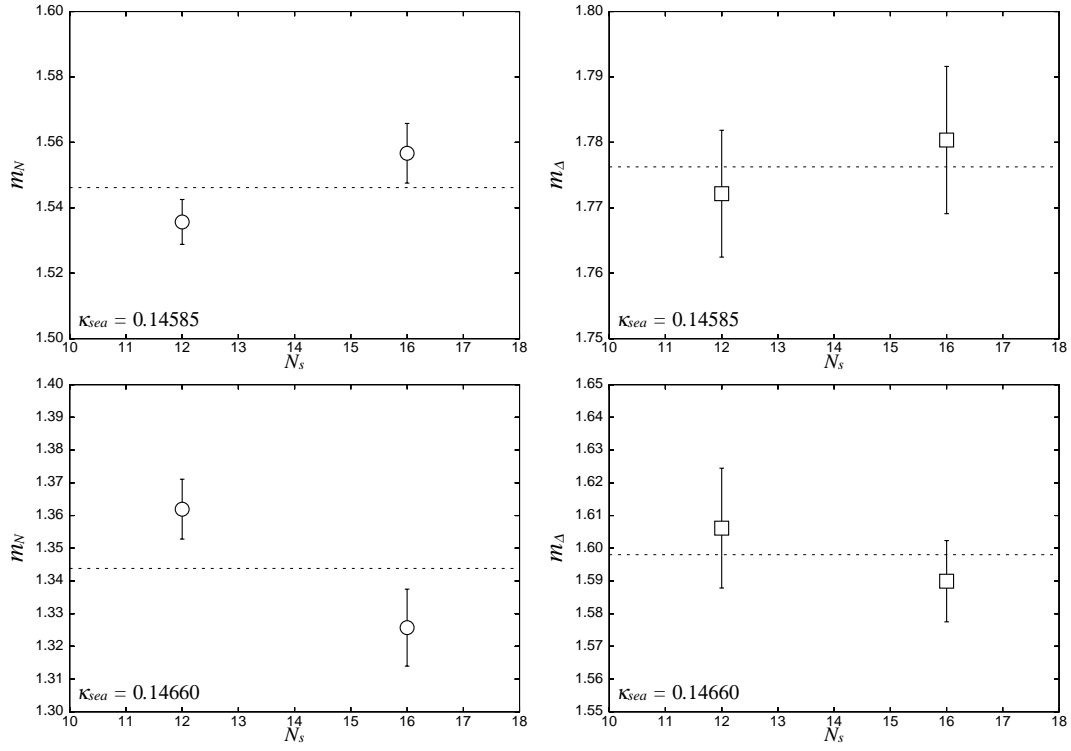


Figure 6.11: Volume dependence of octet (left figure) and decuplet baryon masses (right figure).

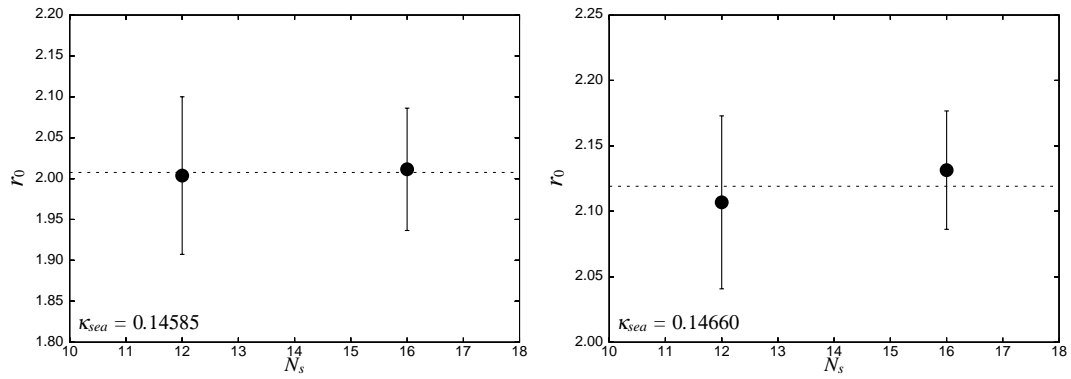


Figure 6.12: Volume dependence of Sommer scales.

Chapter 7

Chiral extrapolations

In order to extrapolate the results of our simulations to their physical values, parameterizations of the lattice data as functions of quark masses are required. In this chapter, our tests are presented using polynomials, functions based on the naive ChPT and those based on the WChPT at one-loop order as the extrapolation functions. All of the parameters in the extrapolation functions are determined by χ^2 fits. The detailed examinations of observables at the physical point are discussed in the next chapter.

7.1 Conventional polynomial extrapolation

We first parameterize pseudoscalar meson masses m_{PS}^2 as a polynomial of the quark mass. For our previous work in the range of $m_{PS}/m_V = 0.80 - 0.55$, the form of the polynomial was quadratic, which was enough to reproduce the lattice data with a reasonable $\chi^2/dof \sim 1$. However significant deviations from the previous fit appear in small sea quark mass region as shown in Fig 7.1. Therefore, we fit m_{PS}^2 with polynomials at several orders. The best fit is obtained by the following form.

$$m_{PS}^2 = B^{PS} m_{quark}^{VWI} + C^{PS} (m_{quark}^{VWI})^2 + D^{PS} (m_{quark}^{VWI})^3 + E^{PS} (m_{quark}^{VWI})^4, \quad (7.1)$$

where the VWI quark mass m_{quark}^{VWI} is defined by

$$m_{quark}^{VWI} = \frac{1}{2} \left(\frac{1}{\kappa} - \frac{1}{\kappa_c} \right). \quad (7.2)$$

The fitting parameters are the critical hopping parameter κ_c and the coefficients $B^{PS} - E^{PS}$. For $D^{PS} = E^{PS} = 0$ (quadratic fit) case, we find that χ^2/dof increases rapidly when the smaller sea quark mass data are added to the previous one as shown in Fig. 7.2. It means that quadratic forms are not enough to describe the sea quark mass dependence in the small quark mass region.

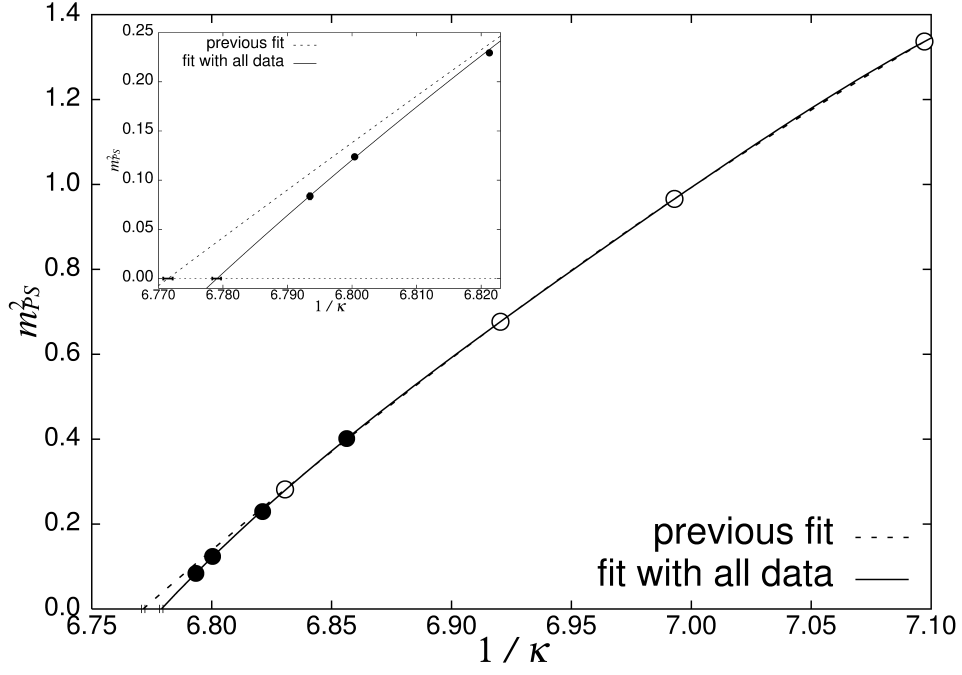


Figure 7.1: Chiral extrapolations of pseudoscalar meson masses. Open symbols show the results obtained in the previous calculations and filled symbols are our new results.

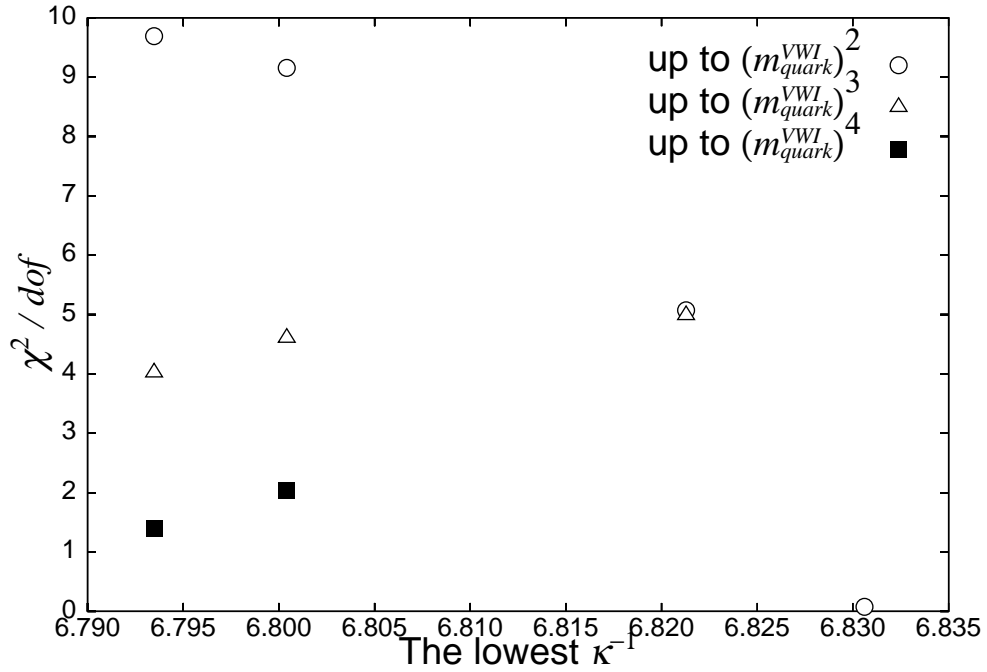


Figure 7.2: Fitting range and function dependence of the quality of fits to pseudoscalar meson masses. The lowest fitting range are changed as shown in the figure, while the highest is fixed to $\kappa = 0.1409$. Quadratic, cubic and quadruple forms of VWI quark masses are tested.

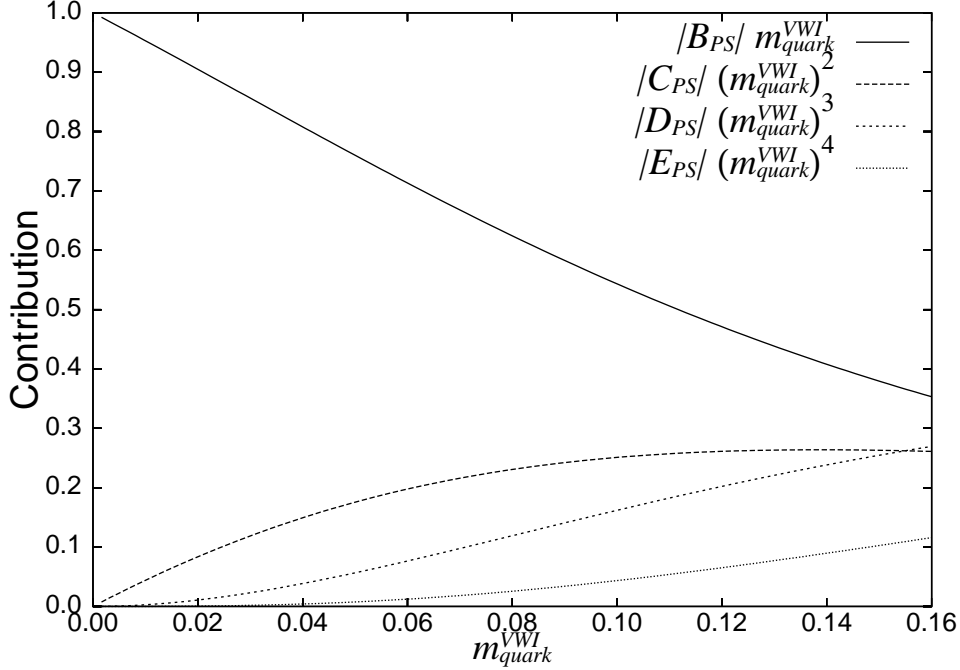


Figure 7.3: Contribution of each term for the fitting of m_{PS}^2 as a function of m_{quark}^{VWI} .

Next we check the contribution of each term to examine if the higher order terms may contribute to this chiral extrapolation. The contributions are plotted in Fig 7.3, which shows the $E^{PS}(m_{quark}^{VWI})^4$ term gives 11% contribution at the heaviest data point. Therefore, even Eq. (7.1) may not be enough for the chiral extrapolation of the pseudoscalar meson masses when smaller sea quark mass data are available. More curvature may appear toward the chiral limit, which can be expressed with higher order terms.

Since m_{PS}^2 may be affected by the logarithmic singularity predicted by ChPT, we also check the order dependence and the convergence of the polynomial extrapolations of the axial vector Ward identity(AWI) quark masses m_{quark}^{AWI} . They have no logarithmic singularity in the context of the naive ChPT. As in the case of m_{PS}^2 , deviations from the previous fit appear as shown in Fig. 7.4. We fit m_{quark}^{AWI} as

$$m_{quark}^{AWI} = B^{AWI} m_{quark}^{VWI} + C^{AWI} (m_{quark}^{VWI})^2 + D^{AWI} (m_{quark}^{VWI})^3 + E^{AWI} (m_{quark}^{VWI})^4. \quad (7.3)$$

The fitting range dependences are shown in Fig. 7.5. As in the case of m_{PS}^2 , terms up to $(m_{quark}^{VWI})^4$ are needed for a reasonable χ^2/dof . The contribution of each term is shown in Fig 7.6. It shows the $E^{PS}(m_{quark}^{VWI})^4$ term gives 13% contribution at the heaviest data point and again the higher order terms may be needed toward the chiral limit.

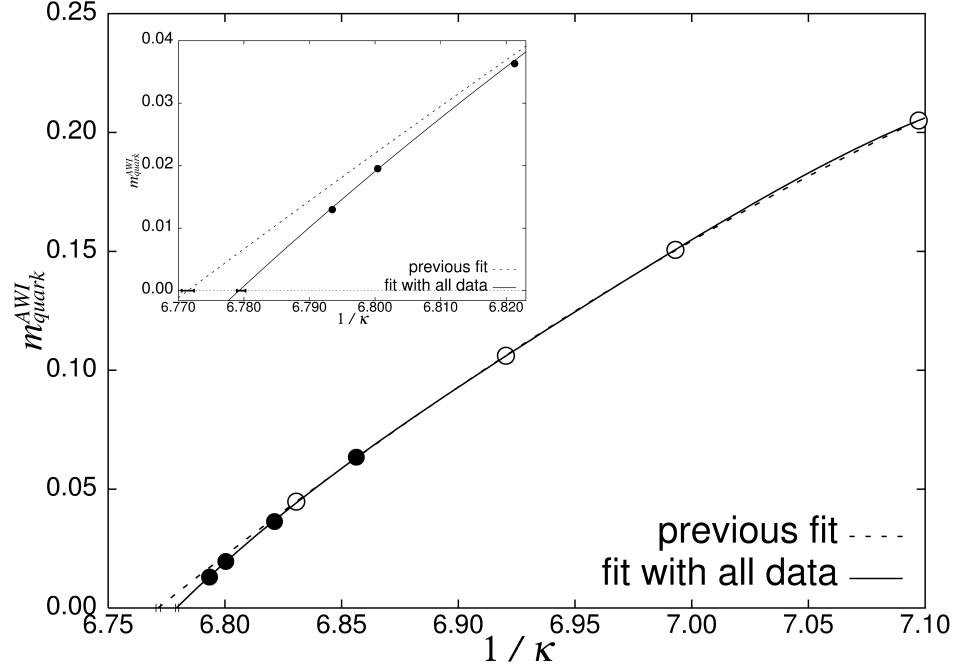


Figure 7.4: Chiral extrapolations of AWI quark masses.

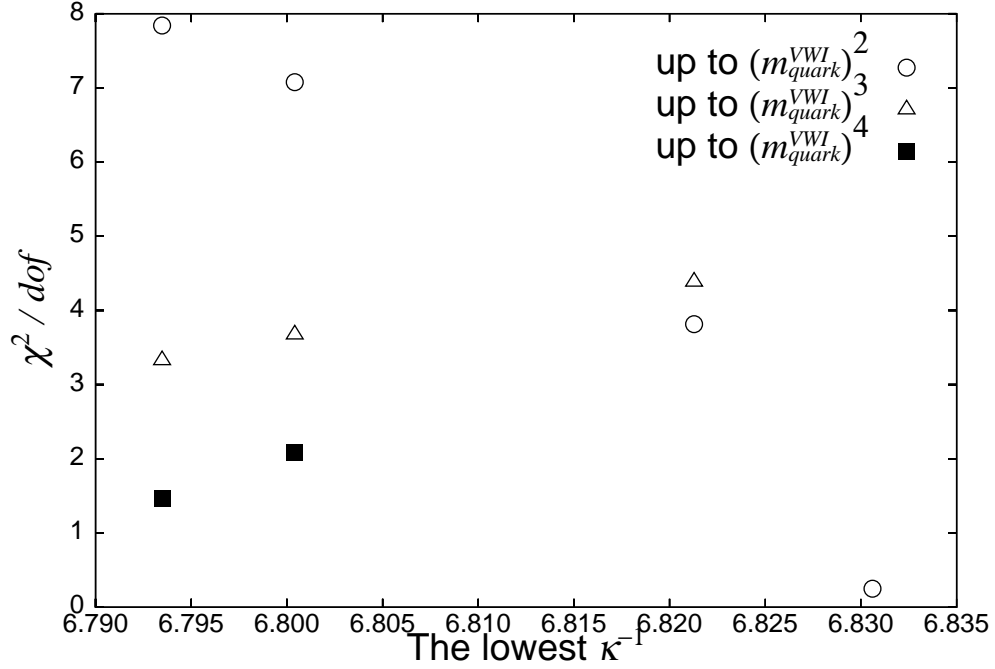


Figure 7.5: Fitting range and function dependence of the quality of fits to AWI quark masses. The highest is also fixed to $\kappa = 0.1409$.

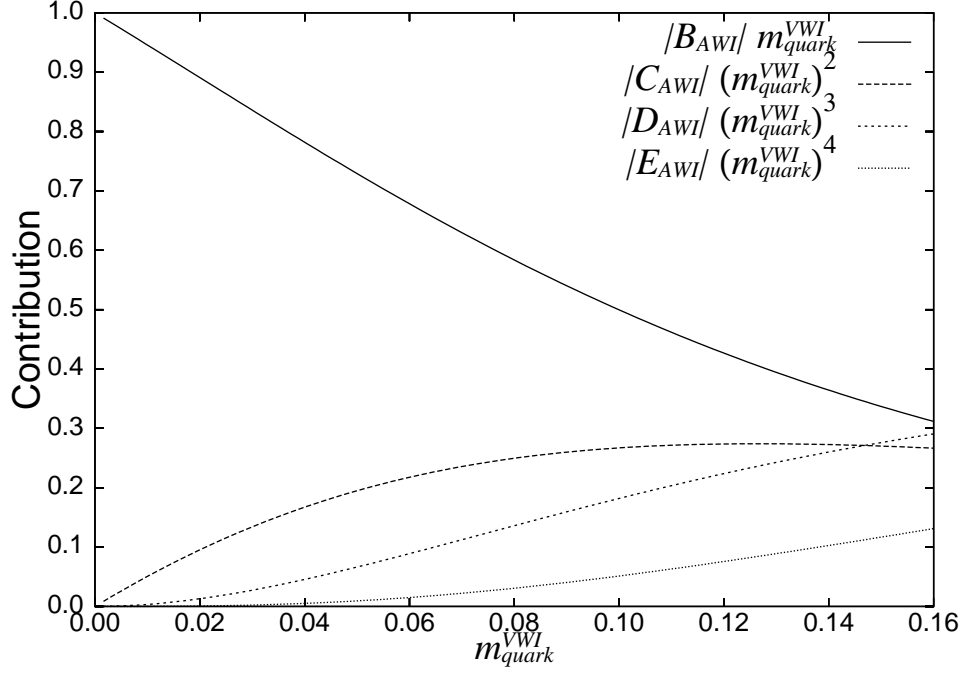


Figure 7.6: Contribution of each term for the fitting of m_{quark}^{AWI} as a function of m_{quark}^{VWI} .

We note that κ_c determined from m_{PS}^2 agrees with that from m_{quark}^{AWI} within errors as shown in Fig. 7.7, in contrast to the case of the quenched QCD, where they differ because of the quenched chiral singularity [29]. Therefore, we simultaneously fit m_{PS}^2 and m_{quark}^{AWI} to determine κ_c and use it for the following polynomial analysis.

The fit results of pseudoscalar meson and AWI quark masses are summarized in Tables 7.1, 7.2.

m_{PS}/m_V	κ_c	B^{AWI}	C^{AWI}	D^{AWI}	E^{AWI}	χ^2/dof	Q
0.35–0.80	0.147502(14)	1.961(60)	-10.5(1.9)	71(20)	-201(67)	7.29/5	0.22
m_{PS}/m_V	κ_c	B^{PS}	C^{PS}	D^{PS}	E^{PS}	χ^2/dof	Q
0.35–0.80	0.147514(15)	12.05(33)	-55.7(90)	359(89)	-966(281)	6.95/5	0.24

Table 7.1: Parameters of independent fits to AWI quark masses and pseudoscalar meson masses as a function of the VWI quark mass.

m_{PS}/m_V	κ_c	B^{AWI}	C^{AWI}	D^{AWI}	E^{AWI}	χ^2/dof
0.35–0.80	0.147508(14)	1.938(54)	-9.8(17)	65(18)	-181(60)	11.4/9
		B^{PS}	C^{PS}	D^{PS}	E^{PS}	Q
		12.18(31)	-58.9(86)	389(85)	-1053(269)	0.26

Table 7.2: Parameters of simultaneous fits to AWI quark masses and pseudoscalar meson masses as a function of the VWI quark mass.

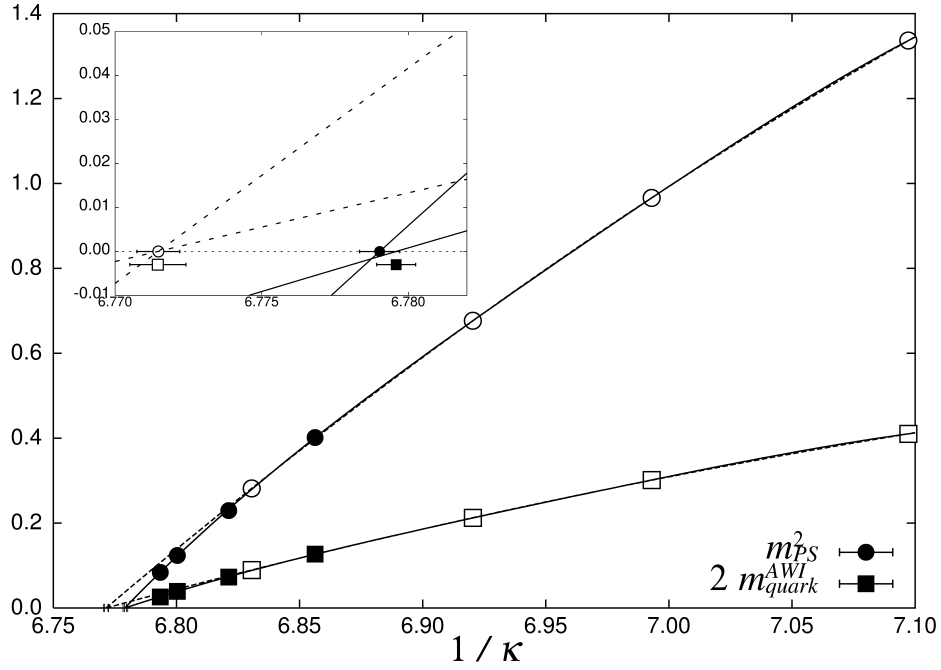


Figure 7.7: Chiral extrapolation of pseudoscalar meson masses and AWI quark masses in terms of a VWI quark mass.

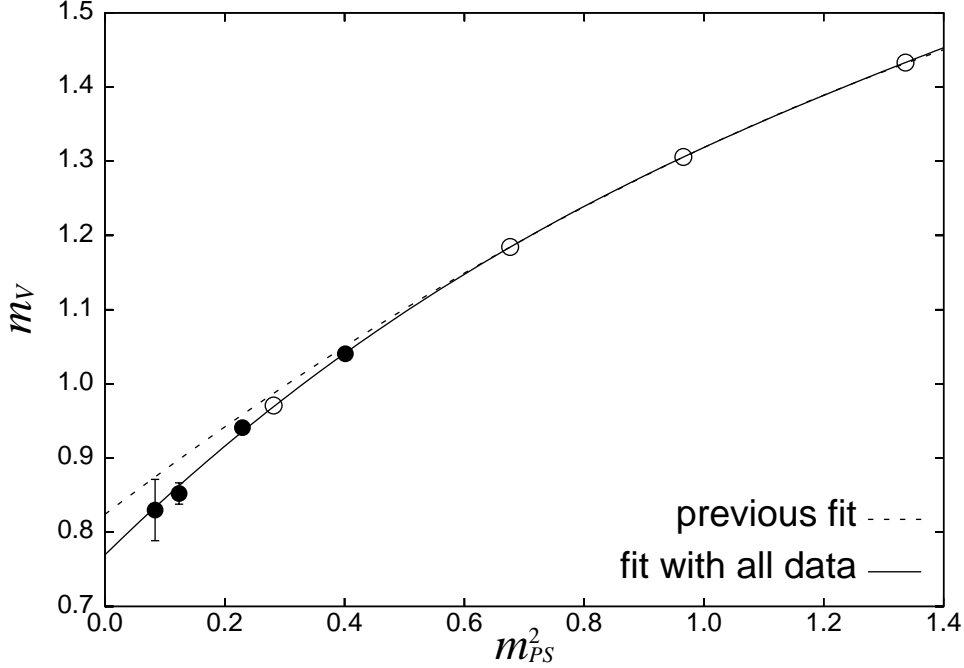


Figure 7.8: Chiral extrapolation of vector meson masses in terms of a pseudoscalar meson mass. Open symbols are the results in our previous study.

Next we parameterize the vector meson masses as a function of the pseudoscalar meson mass.

$$m_V = B^V m_{PS}^2 + D^V m_{PS}^4 + F^V m_{PS}^6. \quad (7.4)$$

The fit results are shown in Fig. 7.8 and Table 7.3. As in the case of m_{PS}^2 and m_{quark}^{AWI} , systematic deviations from the previous fit are also observed in m_V . In the chiral limit, for example, the difference is 7%(3.5 σ). We employ the best fit including m_{PS}^6 term for the following analysis, which shows good convergence as shown in Fig. 7.9.

We note that the effects of vector meson decays are not included because we do not find any clear sign of decays in our propagators for our range of sea quark masses and

m_{PS}/m_V	A^V	B^V	D^V	F^V	χ^2/dof	Q
0.35-0.80	0.7915(72)	0.678(18)	-0.1482(99)	–	2.21/3	0.60
0.35-0.80	0.770(15)	0.790(72)	-0.304(97)	0.063(39)	1.10/4	0.89

Table 7.3: Parameters of fits to vector meson masses.

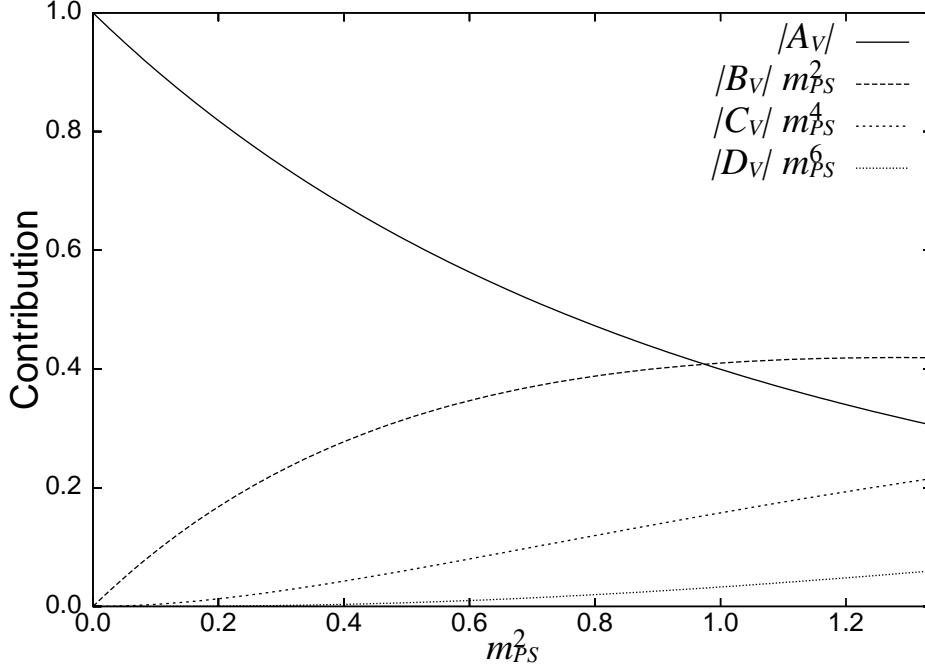


Figure 7.9: Contribution of each term for the fitting of m_V as a function of m_{PS}^2 .

volumes. Naively in the data below $m_{PS}/m_V = 0.50$ a vector meson can decay into two pseudoscalar mesons. However, the finite lattice size limits the lowest momentum of a pseudoscalar meson as $p = 2\pi/L$. Therefore, large lattices as well as small sea quark masses are required for decays of a vector meson.

A simple check of the vector meson decay can be done with $p = 2\pi/L$ vector meson propagators. If a vector meson can decay into two pseudoscalar mesons, the energy of a vector meson with a momentum $2\pi/L$ will be different when it is polarized parallel to the momentum direction or perpendicular to it because of the mixing of a vector and two pseudoscalar meson states [41, 42]. However our data do not show the energy difference as shown in Fig. 7.10. Our range of sea quark masses and spatial volumes may not be enough to create decays of a vector meson.

Chiral extrapolations of pseudoscalar and vector meson decay constants and octet and decuplet baryon masses are carried out as that of the vector meson mass,

$$f_{PS,V} = B^{f_{PS},f_V} m_{PS}^2 + D^{f_{PS},f_V} m_{PS}^4 + F^{f_{PS},f_V} m_{PS}^6, \quad (7.5)$$

$$m_{oct,dec} = B^{oct,dec} m_{PS}^2 + D^{oct,dec} m_{PS}^4 + F^{oct,dec} m_{PS}^6. \quad (7.6)$$

The fit results are summarized in Fig. 7.11, 7.12 and Tables 7.4, 7.5. While deviations from

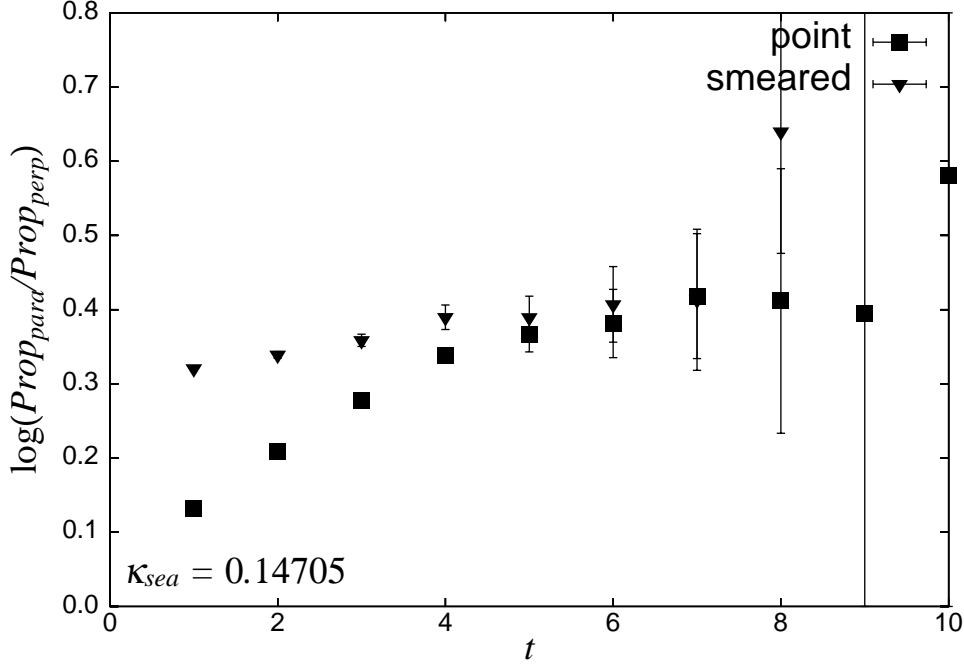


Figure 7.10: Ratio of vector meson correlators with a momentum $2\pi/L$ and the polarization parallel and perpendicular to it.

the previous fit curves appear in decay constants as well as meson masses, baryon masses are almost on the previous fits. It may be caused by the finite size effects. As discussed in Chap. 6.3, our baryon data on $12^3 \times 24$ lattices of $L = 2.4$ fm may be lifted up by finite size effects. Therefore, the sea quark mass dependence may be weakened by finite size effects, which become more significant as sea quark masses decrease.

r_0 is often extrapolated using a linear form. However we found our data show a clear

m_{PS}/m_V	$A^{f_{PS}}$	$B^{f_{PS}}$	$D^{f_{PS}}$	$F^{f_{PS}}$	χ^2/dof	Q
0.35-0.80	0.1239(26)	0.165(17)	-0.076(27)	0.018(12)	17.2/4	0.0018
m_{PS}/m_V	A^{f_V}	B^{f_V}	D^{f_V}	F^{f_V}	χ^2/dof	Q
0.35-0.80	0.228(12)	0.265(59)	-0.156(85)	0.039(35)	2.31/4	0.68

Table 7.4: Parameters of chiral fits to pseudoscalar and vector meson decay constants.

m_{PS}/m_V	A^{oct}	B^{oct}	D^{oct}	F^{oct}	χ^2/dof	Q
0.35-0.80	1.045(23)	1.45(13)	-0.57(19)	0.121(80)	4.02/4	0.40
m_{PS}/m_V	A^{dec}	B^{dec}	D^{dec}	F^{dec}	χ^2/dof	Q
0.35-0.80	1.369(46)	1.06(24)	-0.18(35)	-0.019(151)	2.27/4	0.69

Table 7.5: Parameters of chiral fits to octet and decuplet baryon masses.

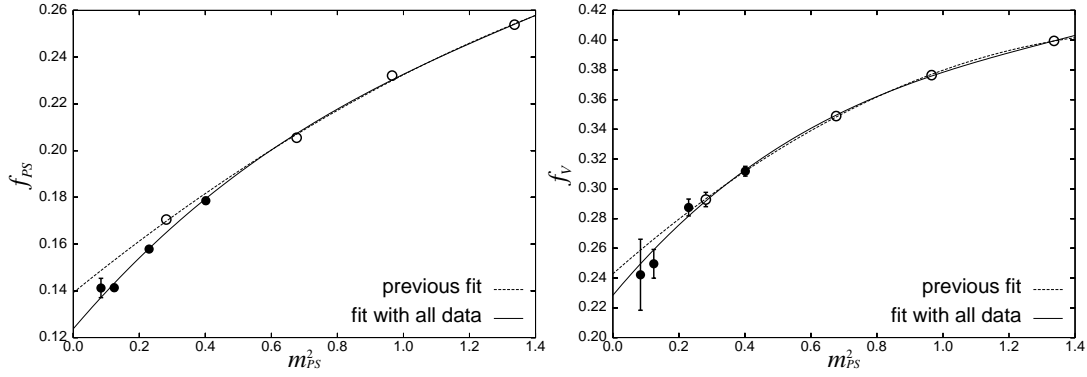


Figure 7.11: Chiral extrapolation of pseudoscalar (left panel) and vector (right panel) meson decay constants. Open symbols are the results in our previous study.

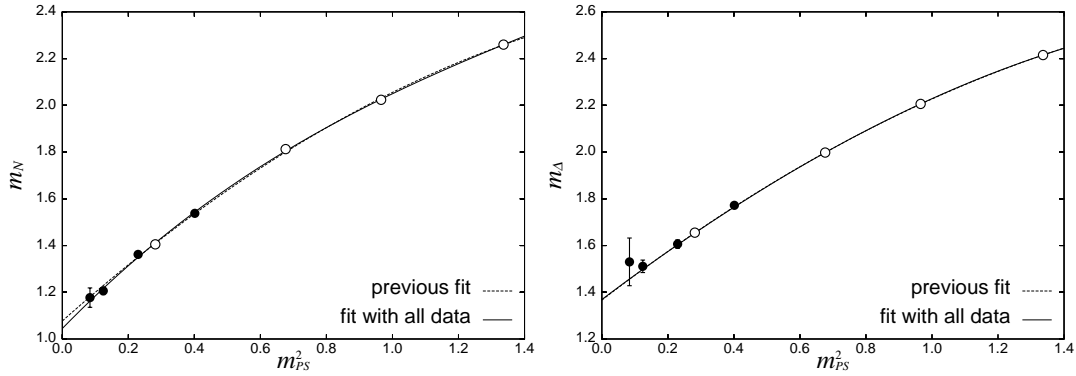


Figure 7.12: Chiral extrapolation of octet (left panel) and decuplet (right panel) baryon masses. Open symbols are the results in our previous study.

curvature. We use the quadratic form as follows,

$$\frac{1}{r_0} = A^{r_0} + B^{r_0} m_{PS}^2 + D^{r_0} m_{PS}^4. \quad (7.7)$$

The fit result is summarized in Fig. 7.13 and Table 7.6.

A_{r_0}	B_{r_0}	D_{r_0}	χ^2/dof	Q
0.4369(82)	0.165(31)	-0.043(25)	0.37/3	0.99

Table 7.6: Parameters of chiral extrapolation of r_0 .

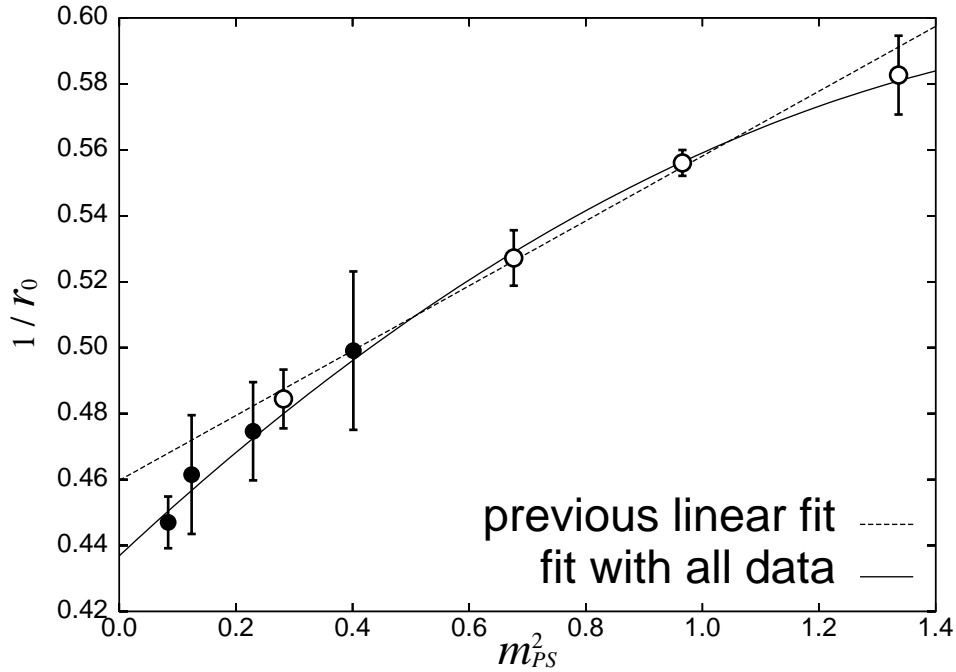


Figure 7.13: Chiral extrapolation of r_0 . Open symbols are the results in our previous study.

We note that we fit hadron masses in lattice units instead of in r_0 normalized units, which is sometimes used in the study of hadron spectrum. However, since we use a coarse lattice $a \simeq 0.2$ fm, r_0 have large systematic errors, which conceal signals.

Let us move on to the explanation of the physical point. The physical point is determined with chiral extrapolations and experimental inputs. We use pion and rho meson

masses in this study. The pion mass at the physical point m_π is determined by solving the equation,

$$\frac{m_\pi}{A_V + B_V m_\pi^2 + D_V m_\pi^4 + F_V m_\pi^6} = \frac{M_\pi}{M_\rho}, \quad (7.8)$$

where we denote the experimental values of the pion and rho meson masses by $M_\pi = 0.1350$ GeV and $M_\rho = 0.7684$ GeV. The rho meson mass at the physical point m_ρ is obtained by Eq. (7.4) with m_π , which determines the lattice spacing a_ρ . Lattice spacings are also determined through r_0 with its phenomenological value $R_0 = 0.49$ fm. Using Eq. (7.7) instead of Eq. (7.4), we have

$$\frac{m_\pi}{A_{r_0} + B_{r_0} m_\pi^2 + D_{r_0} m_\pi^4} = M_\pi R_0. \quad (7.9)$$

Substituting m_π to Eq. (7.7) leads to r_0 at the physical point, which brings an alternative lattice spacing a_{r_0} . The result is $a_{r_0} = 0.2119(61)$ fm, consistent with $a_\rho = 0.2007(38)$ fm within 2σ .

The pion and rho meson decay constants f_π , f_ρ and masses of non-strange baryons N , Δ are determined by substituting m_π to Eq. (7.5) and Eq. (7.6).

The renormalized quark masses in the modified minimal subtraction ($\overline{\text{MS}}$) scheme at 2 GeV are obtained as follows. For the VWI quark mass, solving

$$m_{PS}^2(\kappa_{ud}) = m_\pi^2, \quad (7.10)$$

determines the hopping parameter corresponding to the physical light quark mass κ_{ud} and the VWI quark mass at the physical point,

$$m_{ud}^{VWI} = \frac{1}{2} \left(\frac{1}{\kappa_{ud}} - \frac{1}{\kappa_c} \right). \quad (7.11)$$

Then, m_{ud}^{VWI} is renormalized using one-loop renormalization constants and improvement coefficients at $\mu = 1/a$, as explained in the appendix C.

$$m_R^{VWI} = Z_m \left(1 + b_m \frac{m_{ud}^{VWI}}{u_0} \right) \frac{m_{ud}^{VWI}}{u_0}. \quad (7.12)$$

While the AWI quark mass is obtained with

$$m_R^{AWI} = \frac{Z_A \left(1 + b_A \frac{m_{ud}^{VWI}}{u_0} \right)}{Z_P \left(1 + b_P \frac{m_{ud}^{VWI}}{u_0} \right)} m_{ud}^{VWI}, \quad (7.13)$$

where m_{ud}^{AWI} is calculated by Eq. (7.3) with κ_{ud} . The $\overline{\text{MS}}$ quark masses are evolved to $\mu = 2$ GeV using the four-loop beta function [48, 49].

All results at the physical point extrapolated with polynomials are summarized in Tables 7.7 – 7.9.

	m_{PS}/m_V	$m_N[\text{GeV}]$	$m_\Delta[\text{GeV}]$	$a[\text{fm}]$
Polynomial	0.35–0.80	1.053(27)	1.366(46)	0.2007(38)

Table 7.7: Hadron masses and a lattice spacing obtained by chiral extrapolations with polynomials.

	m_{PS}/m_V	$f_\pi[\text{GeV}]$	$f_\rho[\text{GeV}]$
Polynomial	0.35–0.80	0.1247(31)	0.2294(74)

Table 7.8: pseudoscalar and vector decay constants obtained by chiral extrapolations with polynomials.

	κ_{ud}	$m_R^{VWI}[\text{MeV}]$	$m_R^{AWI}[\text{MeV}]$
Polynomial	0.147440(13)	1.749(53)	2.851(58)

Table 7.9: ud quark masses in $\overline{\text{MS}}$ scheme at $\mu = 2$ GeV obtained by chiral extrapolations with polynomials and the corresponding hopping parameter κ_{ud} .

7.2 Naive ChPT extrapolation

In the quark mass dependence of the pseudoscalar meson mass and the pseudoscalar meson decay constant, the naive ChPT predicts presence of logarithmic singularities. At the one-loop level [9, 11],

$$\frac{m_{PS}^2}{2B_0 m_{quark}} = 1 + \frac{1}{N_f} \frac{2B_0 m_{quark}}{(4\pi f)^2} \log \frac{2B_0 m_{quark}}{\Lambda_3^2} \quad (7.14)$$

$$f_{PS} = f \left(1 - \frac{N_f}{2} \frac{2B_0 m_{quark}}{(4\pi f)^2} \log \frac{2B_0 m_{quark}}{\Lambda_4^2} \right). \quad (7.15)$$

The fitting parameters are B_0 , f , Λ_3 and Λ_4 . We fit m_{PS}^2 and f_{PS} simultaneously to keep the same fitting parameters in m_{PS}^2 and f_{PS} . Though m_{PS}^2 and f_{PS} are correlated, for simplicity uncorrelated fits are employed. Since we use the Jackknife error estimation, the errors of the simultaneous fit reflect the correlation correctly. All we have to care for is that the value of χ^2/dof can not be compared with those obtained from single fits and should be considered as a guide for the quality of the simultaneous fit.

We have two choice for m_{quark} ; m_{quark}^{AWI} or m_{quark}^{VWI} . We test both cases. The fit results for both m_{quark}^{AWI} and m_{quark}^{VWI} cases are summarized in Table 7.10.

- Case 1($m_{quark} = m_{quark}^{AWI}$) : We find the one-loop formulae do not reproduce our data of $m_{PS}/m_V = 0.80 - 0.35$, which give huge $\chi^2/dof \sim 70$. The mass ratio on the left hand-side of Eq.(7.14) is plotted in Fig. 7.14. Our data do not show a curvature except the small sea quark mass region $m_{PS}/m_V = 0.35, 0.40$. Then we drop the heavy sea quark mass data from the fit until the one-loop formulae work. We found the one-loop ChPT can describe the data of $m_{PS}/m_V = 0.60 - 0.35$. It suggests that the naive ChPT formulae should be applied at least below $m_{PS}/m_V = 0.60$.
- Case 2($m_{quark} = m_{quark}^{VWI}$) : In contrast to the Case 1, the mass ratio with m_{quark}^{VWI} plotted in Fig. 7.15 shows a curvature. However, the situation is similar. The fit with $m_{PS}/m_V = 0.80 - 0.35$ gives $\chi^2/dof \sim 100$. The fit range of $m_{PS}/m_V = 0.60 - 0.35$ is also required to fit our data by Eq.(7.14).

Though we can fit our data of $m_{PS}/m_V = 0.60 - 0.35$ by the one-loop naive ChPT formulae, we should be careful for the reliability of the fittings. The fitting range is not wide, which makes the fit less predictive. Another is that $\Lambda_4 = 2.26(7)$ obtained by the fit does not agree with the phenomenological estimation $\Lambda_4 = 1.26(14)$ [28]. More serious problem is the violation of the chiral symmetry, whose effects are sizable in the VWI and

m_{PS}/m_V	B_0^{AWI}	f^{AWI}	Λ_3^{AWI}	Λ_4^{AWI}	χ^2/dof	Q
0.35-0.80	3.838(15)	0.12161(47)	1.553(10)	2.648(15)	283/4	10^{-174}
0.35-0.60	3.398(52)	0.1130(20)	0.902(71)	2.591(98)	7.45/4	0.083
m_{PS}/m_V	B_0^{VWI}	f^{VWI}	Λ_3^{VWI}	Λ_4^{VWI}	χ^2/dof	Q
0.35-0.80	6.886(22)	0.13226(35)	2.4021(85)	2.473(11)	470/4	10^{-294}
0.35-0.60	6.582(87)	0.1145(18)	1.645(83)	2.262(72)	11.7/4	0.0076

Table 7.10: Chiral extrapolation of pseudoscalar meson masses and decay constants based on the naive ChPT formulae at 1-loop with $m_{quark} = m_{quark}^{AWI}$ and $m_{quark} = m_{quark}^{VWI}$. κ_c has been determined with m_{quark}^{AWI} . The value of κ_c is shown in Table 7.1.

m_{PS}/m_V	A^V	B^V	C^V	χ^2/dof	Q
0.35-0.80	0.7692(86)	0.897(32)	-0.346(23)	0.83/3	0.93
0.35-0.60	0.731(45)	1.31(49)	-0.85(60)	0.49/3	0.85

Table 7.11: Parameters of chiral fits to vector meson masses based on ChPT.

AWI quark masses and decay constants. The assumption of the naive ChPT is broken significantly on our coarse lattices of $a \sim 0.2$ fm.

For the vector meson, we use the following function based on ChPT in the static limit of the vector meson mass [43].

$$m_V = B^V m_{PS}^2 + C^V m_{PS}^3. \quad (7.16)$$

This cubic form describes our data well. The fit result is summarized in Fig. 7.16 and Table 7.11. Chiral extrapolations of octet and decuplet baryon masses are carried out with [44]

$$m_{oct,dec} = B^{oct,dec} m_{PS}^2 + C^{oct,dec} m_{PS}^3. \quad (7.17)$$

The results are summarized in Fig. 7.17 and Table 7.12.

To obtain the pseudoscalar meson mass at the physical point m_π , Eq. (7.16) is used instead of Eq. (7.4).

$$\frac{m_\pi}{A_V + B_V m_\pi^2 + C_V m_\pi^3} = \frac{M_\pi}{M_\rho}. \quad (7.18)$$

The masses of non-strange baryons N and Δ are determined by substituting m_π to Eq. (7.17). The pion decay constant f_π is obtained by use of Eq. (7.14) and Eq. (7.15).

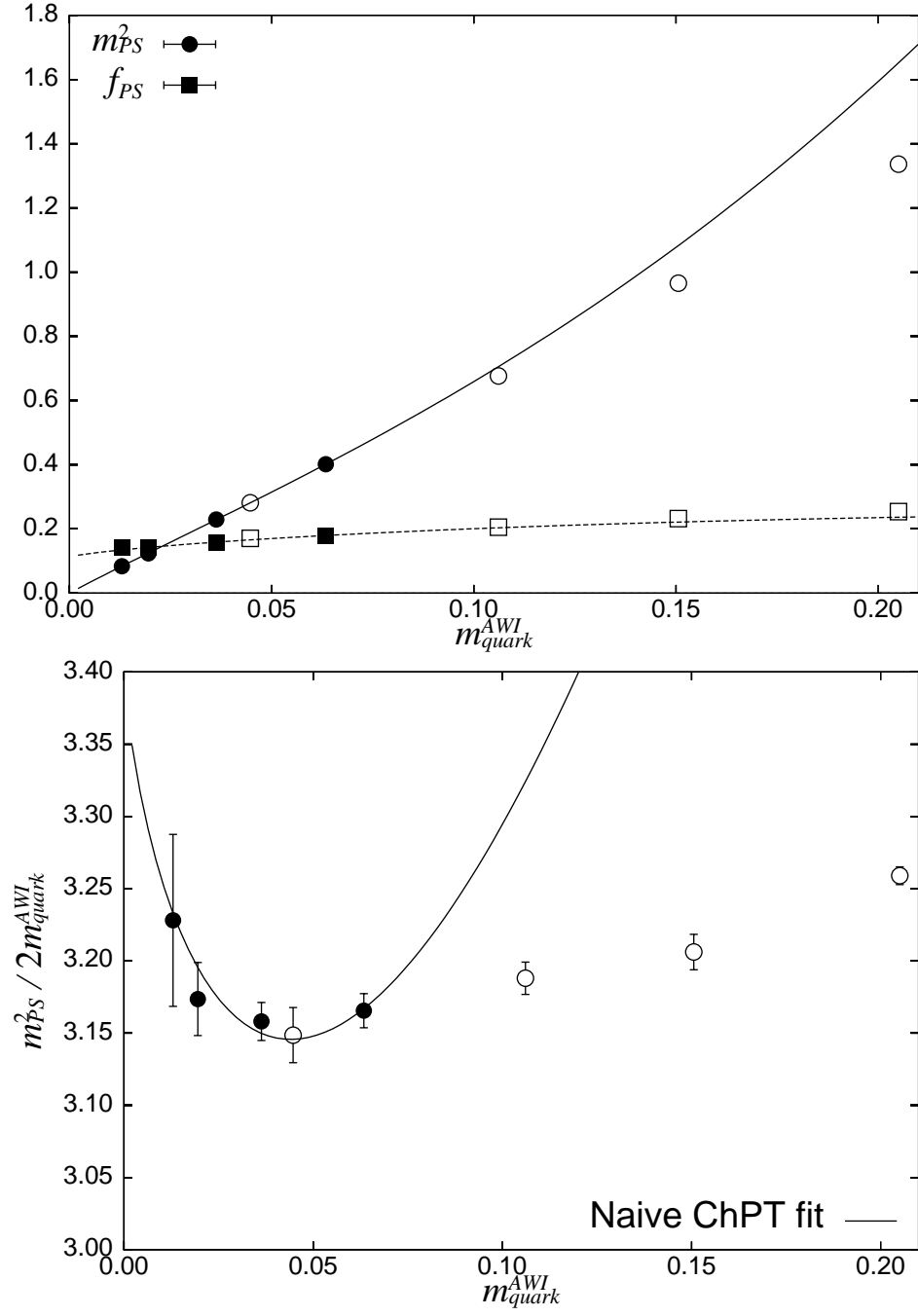


Figure 7.14: Test of the naive ChPT simultaneous fit to pseudoscalar meson masses and decay constants. We use the quark mass defined through the axial vector Ward identity in this plot. The down figure shows the mass ratio to zoom in the chiral logarithm behavior.

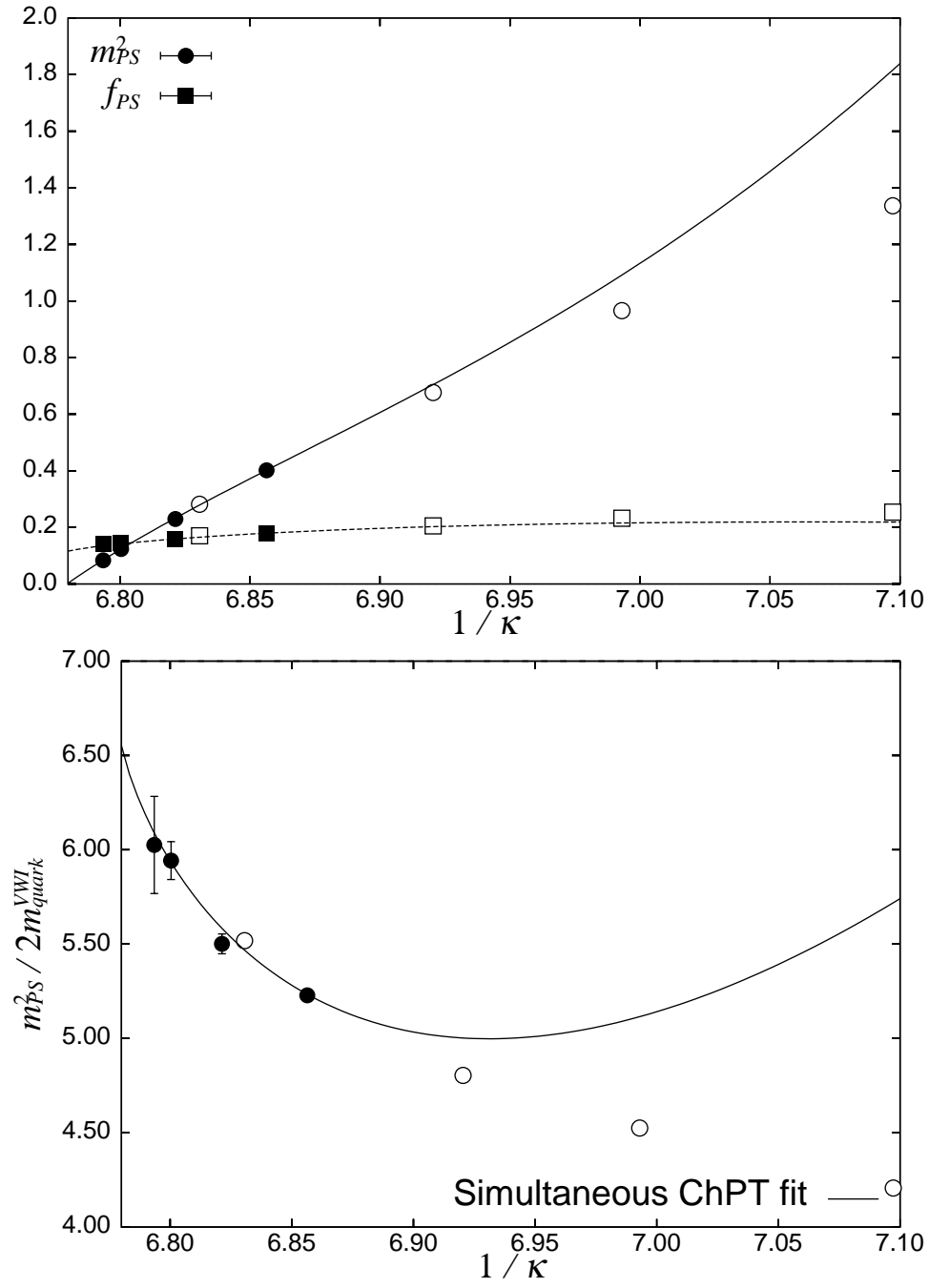


Figure 7.15: Test of the naive ChPT simultaneous fit with the quark mass defined through the vector Ward identity.

m_{PS}/m_V	A^{oct}	B^{oct}	C^{oct}	χ^2/dof	Q
0.35-0.80	1.042(14)	1.651(68)	-0.640(52)	2.64/3	0.49
0.35-0.60	0.981(59)	2.48(71)	-1.73(90)	2.26/3	0.39
m_{PS}/m_V	A^{dec}	B^{dec}	C^{dec}	χ^2/dof	Q
0.35-0.80	1.335(24)	1.404(98)	-0.515(72)	1.56/3	0.76
0.35-0.60	1.53(16)	-0.9(19)	2.4(24)	2.86/3	0.33

Table 7.12: Parameters of chiral fits to octet and decuplet baryon masses based on ChPT.

Substituting m_π to Eq. (7.14) brings the bare quark mass at the physical point m_{ud} . Then Eq. (7.15) with m_{ud} gives f_π . The ChPT formula for the rho meson decay constant has not been available yet. Renormalized quark masses are calculated with m_{ud} as in the case of polynomial extrapolations.

Our results extrapolated to the physical point are summarized in Tables 7.13 –7.15.

	m_{PS}/m_V	$m_N[\text{GeV}]$	$m_\Delta[\text{GeV}]$	$a[\text{fm}]$
ChPT	0.35–0.60	1.052(72)	1.56(16)	0.192(10)
	0.35–0.80	1.029(14)	1.306(22)	0.2009(21)

Table 7.13: Hadron masses and a lattice spacing obtained by chiral extrapolations with the naive one-loop ChPT formulae.

	m_{PS}/m_V	$f_\pi[\text{GeV}]$
ChPT($m_{quark} = m_{quark}^{AWI}$)	0.35–0.60	0.1219(64)
ChPT($m_{quark} = m_{quark}^{VWI}$)	0.35–0.60	0.1231(65)

Table 7.14: pseudoscalar decay constants obtained by chiral extrapolations with the naive one-loop ChPT formulae.

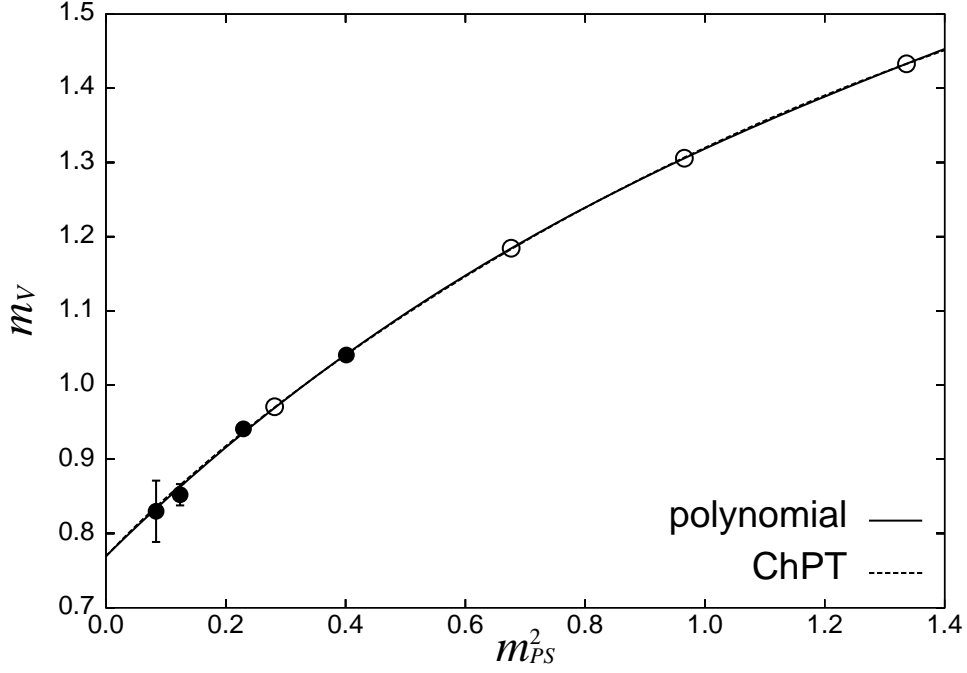


Figure 7.16: Chiral extrapolation of vector meson masses with a polynomial and a function motivated by ChPT. Open symbols are the results in our previous study.

	κ_{ud}	$m_R^{VWT}[\text{MeV}]$	$m_R^{AWT}[\text{MeV}]$
Naive ChPT($m_{quark} = m_{quark}^{AWT}$)	0.147445(14)	1.557(97)	2.57(15)
Naive ChPT($m_{quark} = m_{quark}^{VWT}$)	0.1474431(65)	1.57(36)	2.60(53)

Table 7.15: ud quark masses in $\overline{\text{MS}}$ scheme at $\mu = 2 \text{ GeV}$ obtained by chiral extrapolations with the naive one-loop ChPT formulae and the corresponding hopping parameter κ_{ud} .

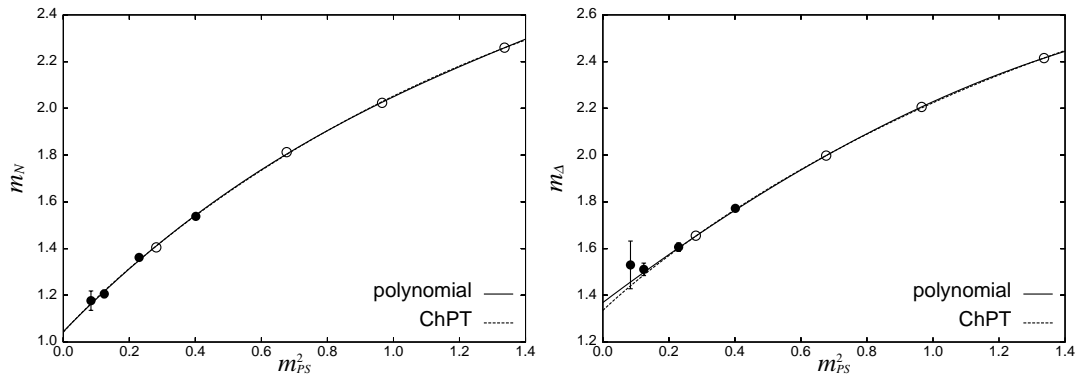


Figure 7.17: Chiral extrapolation of octet (left panels) and decuplet (right panels) baryon masses with polynomials and functions motivated by ChPT. Open symbols are the results in our previous study.

7.3 WChPT extrapolation

Though several kinds of WChPT formulae have been proposed [12–15], we employ the one-loop formulae including a^2 effect. The $O(a^2)$ chiral breaking term play an essential role to generate the parity-flavor breaking phase transition, which is necessary to explain existence of massless pions for the Wilson-type quark action [45–47].

WChPT including effects of the chiral symmetry breaking predicts several features, which do not appear in the naive ChPT. The ChPT log curvature in the pseudoscalar meson mass can be weakened by the $O(a^2)$ chiral symmetry breaking terms and additional log contributions appear. The one-loop WChPT formulae are [15]

$$m_{PS}^2 = Am_{quark}^{VWI} \left(1 + \omega_1^{PS} m_{quark}^{VWI} \log \left(\frac{Am_{quark}^{VWI}}{\Lambda_3^2} \right) + \omega_0 \log \left(\frac{Am_{quark}^{VWI}}{\Lambda_0^2} \right) \right) \quad (7.19)$$

$$m_{quark}^{AWI} = m_{quark}^{VWI} \left(1 + \omega_1^{AWI} m_{quark}^{VWI} \log \left(\frac{Am_{quark}^{VWI}}{\Lambda_{3,AWI}^2} \right) + \omega_0 \log \left(\frac{Am_{quark}^{VWI}}{\Lambda_0^2} \right) \right) \quad (7.20)$$

$$f_{PS} = f \left(1 - \omega_1^{fPS} m_{quark}^{VWI} \log \left(\frac{Am_{quark}^{VWI}}{\Lambda_4^2} \right) \right) \quad (7.21)$$

where the fitting parameters are κ_c , A , f , ω_0 , ω_1^{PS} , ω_1^{AWI} , ω_1^{fPS} , Λ_3 , $\Lambda_{3,AWI}$, Λ_0 and Λ_4 . The overall factor of m_{quark}^{AWI} can be absorbed in ω_0 and Λ_0 . We should be careful that $\omega_0 \sim O(a^2)$, $\omega_1^{AWI} \sim O(a)$ and

$$\omega_1^{PS} = \frac{(A + w_1^\pi a)m_R}{32\pi^2 f_\pi^2}, \quad (7.22)$$

$$\omega_1^{fPS} = \frac{(A + w_1^{f\pi} a)m_R}{32\pi^2 f_\pi^2}, \quad (7.23)$$

where f_π is the pion decay constant in the continuum and chiral limit, which can be different from f by $O(a)$ effects.

We first fit m_{PS} and m_{quark}^{AWI} simultaneously. Then we fit f_{PS} fixing A and κ_c . As in the case of the naive ChPT, we employ uncorrelated fits for simplicity. Therefore, the χ^2/dof should be used to check the quality of the fit but the errors of the fit include the correlation because of the Jackknife error estimation. The fit results are summarized in Fig. 7.18 and Tables 7.16, 7.17. The one-loop WChPT formulae reproduce our data of $m_{PS}/m_V = 0.80 - 0.35$ well.

Since $\log m_R$ in WChPT becomes larger and larger toward the chiral limit, we must perform a resummation of $\log m_R$. A resummed WChPT inspired by some 4 dimensional

m_{PS}/m_V	κ_c	A	ω_0	ω_1^{PS}	ω_1^{AWI}
0.35-0.80	0.147445(27)	6.312(44)	-0.40(13)	-2.0(14)	-2.0(14)
	Λ_0	Λ_3	Λ_3^{AWI}	χ^2/dof	Q
	0.91(35)	1.95(15)	1.77(23)	15.3/9	0.11

Table 7.16: Parameters of chiral fits to pseudoscalar meson and AWI quark masses based on WChPT.

m_{PS}/m_V	f	ω_1^{fPS}	Λ_4	χ^2/dof	Q
0.35-0.80	0.1233(17)	3.73(30)	2.44(13)	10.9/3	0.0028

Table 7.17: Parameters of chiral fits to pseudoscalar meson decay constants based on WChPT. κ_c and A has been fixed to the values in Table 7.16.

scalar(pion) theory predicts [15],

$$m_{PS}^2 = Am_{quark}^{VWI} \left(-\log \left(\frac{Am_{quark}^{VWI}}{\Lambda_0^2} \right) \right)^{\omega_0} \left(1 + \omega_1^{PS} m_{quark}^{VWI} \log \left(\frac{Am_{quark}^{VWI}}{\Lambda_3^2} \right) \right) \quad (7.24)$$

$$m_{quark}^{AWI} = m_{quark}^{VWI} \left(-\log \left(\frac{Am_{quark}^{VWI}}{\Lambda_0^2} \right) \right)^{\omega_0} \left(1 + \omega_1^{AWI} m_{quark}^{VWI} \log \left(\frac{Am_{quark}^{VWI}}{\Lambda_{3,AWI}^2} \right) \right) \quad (7.25)$$

where the fitting parameters are κ_c , A , ω_0 , ω_1^{PS} , ω_1^{AWI} , Λ_3 , $\Lambda_{3,AWI}$ and Λ_0 . We note that f_{PS} is not affected directly by the resummation because $\log m_R$ terms are not appeared in f_{PS} . It just reflects the shift of κ_c . The fit results are summarized in Fig. 7.19 and Tables 7.18, 7.19. The resummed WChPT formulae also describe our whole data well.

Let us discuss the parameters determined by the fit. As in the case of the naive ChPT, $\Lambda_4 = 2.44(13)$ does not agree with the phenomenological estimation $\Lambda_4 = 1.26(14)$ [28]. The possible reasons are the renormalization factor of the axial current and the scaling violation. The non-perturbative renormalization factor and the scaling check are needed for a definite conclusion. Next we examine $(\omega_1^{PS} - \omega_1^{AWI})$, which controls the curvature in $m_{PS}^2/2m_{quark}^{AWI}$. Our fit result is $(\omega_1^{PS} - \omega_1^{AWI}) = 0.24(71)$. The counter part in the continuum theory is estimated approximately as $\omega_1^{PS} = A/32\pi^2 f_\pi^2 \sim 2.4$, $\omega_1^{AWI} = 0$, where the phenomenological value of $f_\pi = 0.086$ [GeV] and $A = 2B_0(\overline{MS}, \mu = 2 \text{ GeV}) \sim 2.8$ [GeV] are used [11]. Therefore, the curvature is suppressed to 10% of the naive ChPT by the $O(a)$ contributions.

m_{PS}/m_V	κ_c	A	ω_0	ω_1^{PS}	ω_1^{AWI}
0.35-0.80	0.147458(20)	6.354(59)	0.5418(46)	0.65(51)	0.42(49)
	Λ_0	Λ_3	Λ_3^{AWI}	χ^2/dof	Q
	1.59(11)	0.15(15)	0.07(16)	14.2/9	0.14

Table 7.18: Parameters of chiral fits to pseudoscalar meson and AWI quark masses based on the resummed WChPT.

m_{PS}/m_V	f	ω_1^{fPS}	Λ_4	χ^2/dof	Q
0.35-0.80	0.1227(17)	3.78(30)	2.44(13)	10.9/3	0.0028

Table 7.19: Parameters of chiral fits to pseudoscalar meson decay constants based on the resummed WChPT. κ_c and A has been fixed to the values in Table 7.18.

WChPT formulae for a vector meson and baryons has not been available. We leave them for future works.

Next we discuss observables at the physical point. Since we have not had the WChPT formulae for a vector meson and baryons, we use Eq. (7.16) to determine the physical pion mass m_π as in the case of the naive ChPT. Therefore, the differences from the ChPT results appear in quark masses and the pseudoscalar decay constant. Substituting m_π to Eq. (7.24) determines the VWI quark mass at the physical point m_{ud}^{VWI} . Then Eq. (7.25) and Eq. (7.21) with m_{ud}^{VWI} give m_{ud}^{AWI} and f_π respectively.

Our results are summarized in Tables 7.20, 7.21.

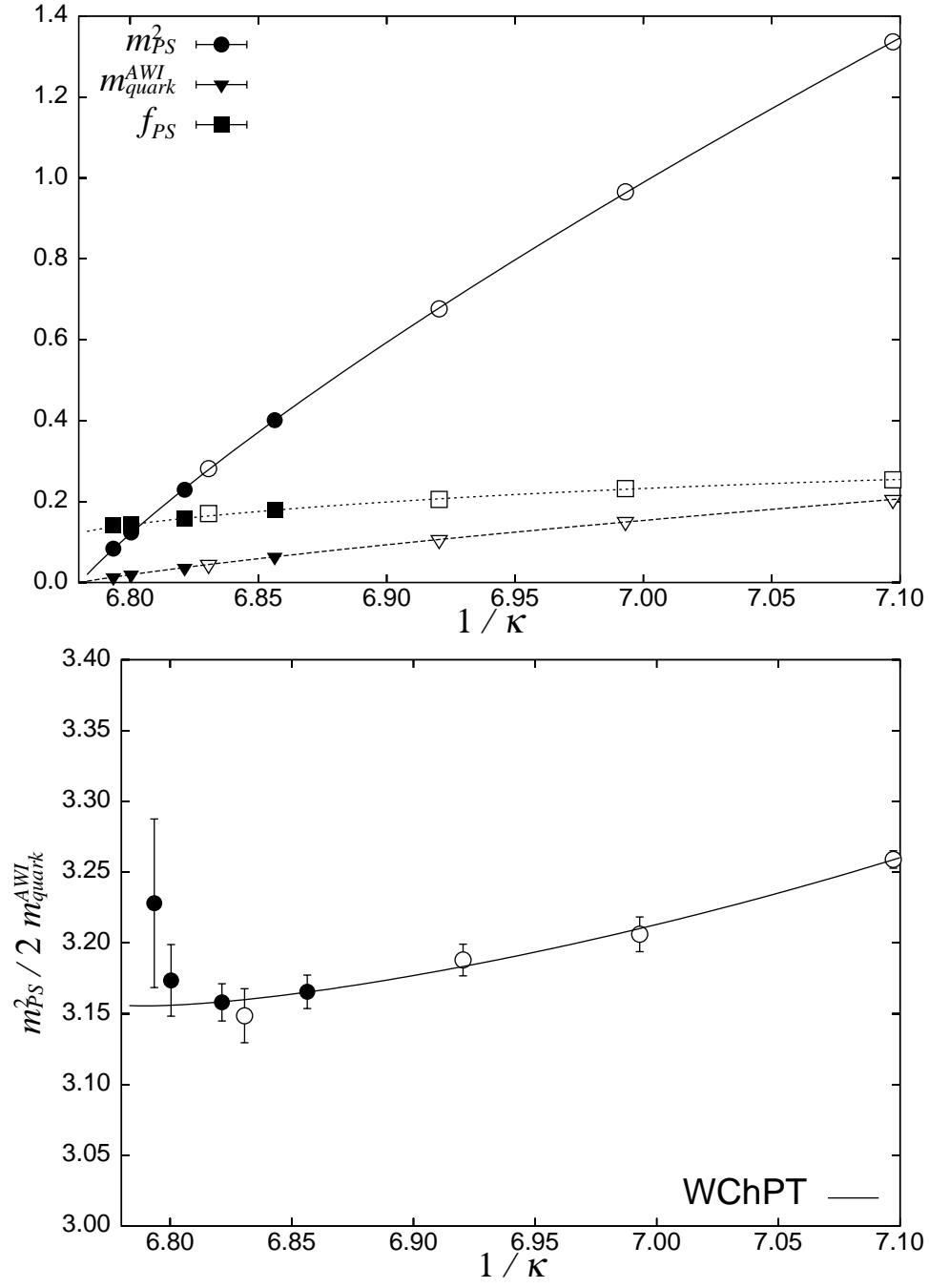


Figure 7.18: Test of the WChPT fit to pseudoscalar meson masses, AWI quark masses and decay constants. The left figure shows the mass ratio to zoom in the chiral logarithm behavior.

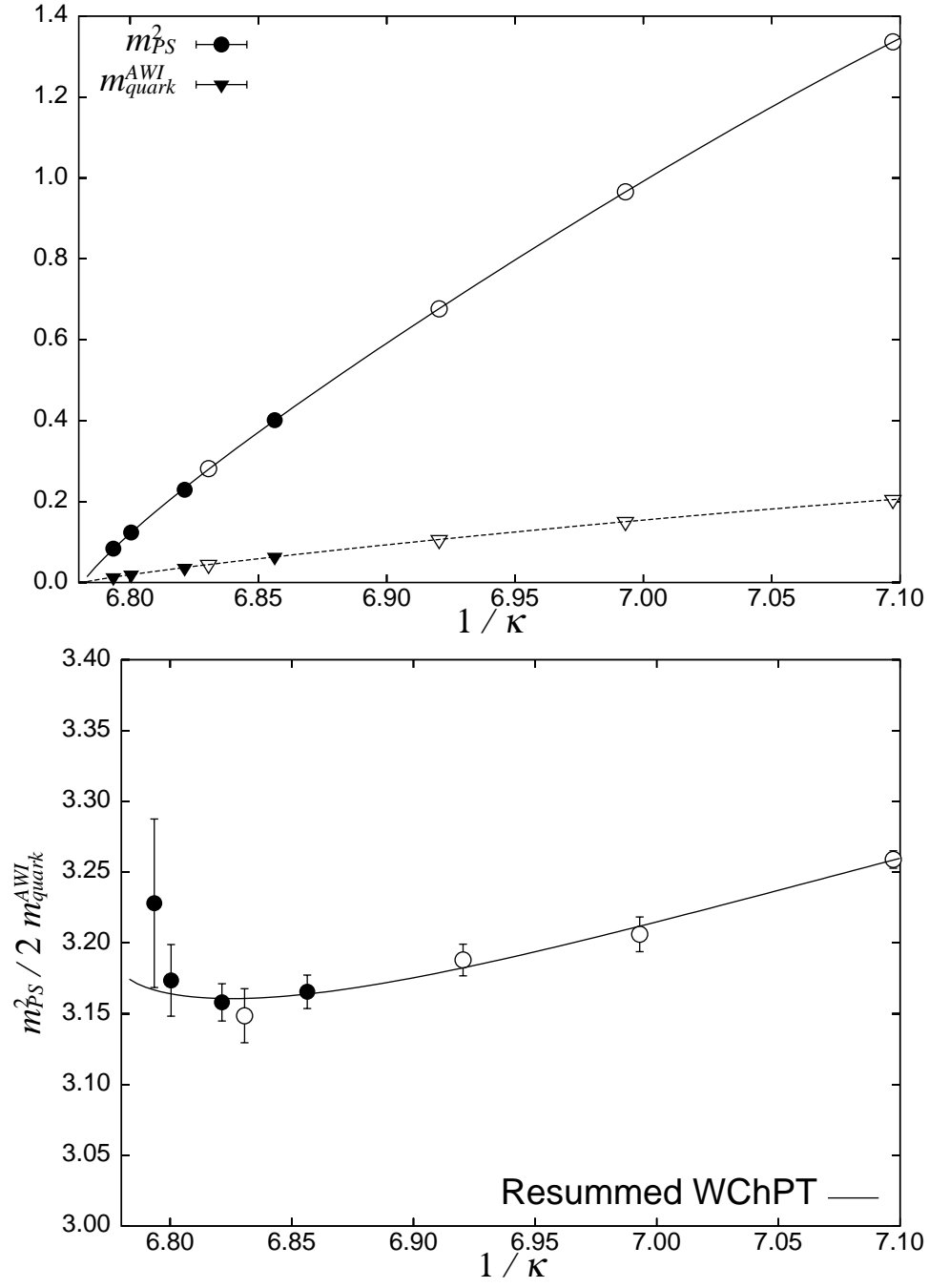


Figure 7.19: Test of the resummed WChPT fit to pseudoscalar meson masses and AWI quark masses. The down figure shows the mass ratio to zoom in the chiral logarithm behavior.

	m_{PS}/m_V	$f_\pi[\text{GeV}]$
WChPT	0.35–0.80	0.1242(23)
resummed WChPT	0.35–0.80	0.1238(21)

Table 7.20: pseudoscalar decay constants obtained by chiral extrapolations with the one-loop WChPT formulae.

	κ_{ud}	$m_R^{VWI}[\text{MeV}]$	$m_R^{AWI}[\text{MeV}]$
WChPT	0.147402(21)	1.09(16)	2.741(35)
resummed WChPT	0.147411(16)	1.230(94)	2.725(38)

Table 7.21: ud quark masses in $\overline{\text{MS}}$ scheme at $\mu = 2 \text{ GeV}$ obtained by chiral extrapolations with the one-loop WChPT formulae and the corresponding hopping parameter κ_{ud} .

Chapter 8

Observables at the physical point

Comparisons with the previous results and dependences of physical observables on function forms of chiral extrapolations are presented in this chapter. First, deviations from the previous results in the polynomial extrapolation case are discussed. Then, differences between polynomial and ChPT-based extrapolations are examined.

8.1 Deviations from the previous results

The results at the physical points obtained with polynomial extrapolations are summarized in Table 8.1. The deviations from the previous results are especially large for the quark masses, as shown in Fig. 8.1. The quadratic extrapolations in the previous study underestimated the sea quark mass dependence. The quark mass in the continuum limit may have been overestimated by 10 – 20%.

	this study	previous	difference
$a_\rho[\text{fm}]$	0.2007(38)	0.2150(22)	-7%(3.8 σ)
$m_R^{VWI}(\mu = 2 \text{ GeV})[\text{MeV}]$	1.749(53)	2.277(27)	-23%(10 σ)
$m_R^{AWI}(\mu = 2 \text{ GeV})[\text{MeV}]$	2.851(58)	3.094(35)	-8%(4.2 σ)
$f_\pi[\text{GeV}]$	0.1247(31)	0.1288(33)	-3%(1.2 σ)
$f_\rho[\text{GeV}]$	0.2294(74)	0.2389(47)	-4%(1.3 σ)
$m_N[\text{GeV}]$	1.053(27)	1.016(16)	+4%(1.4 σ)
$m_\Delta[\text{GeV}]$	1.366(46)	1.270(23)	+4%(2.1 σ)

Table 8.1: Lattice spacing, quark masses and hadron quantities in physical units.

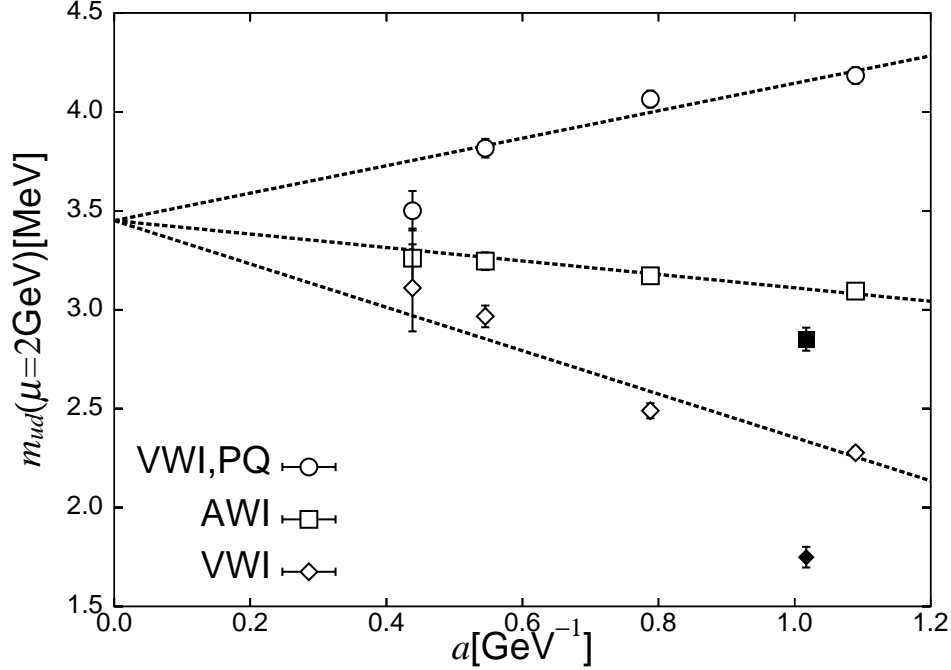


Figure 8.1: Comparison of degenerate up and down quark masses obtained by chiral extrapolations with polynomials. Open symbols show the results obtained in the previous calculations and filled symbols are our new results. Lines are combined linear continuum extrapolations in the previous calculation.

8.2 Comparison of function form dependence of physical quantities

We observed that the chiral extrapolations depend on the function forms. Both polynomials and resummed WChPT formulae reproduce our data well. However, they give different values at the physical point.

$$m_R^{\text{VWI}}(\mu = 2 \text{ GeV})[\text{MeV}] = \begin{cases} 1.230(94) & (\text{resummed WChPT}) \\ 1.749(53) & (\text{polynomial}) \end{cases} \quad (8.1)$$

$$m_R^{\text{AWI}}(\mu = 2 \text{ GeV})[\text{MeV}] = \begin{cases} 2.725(38) & (\text{resummed WChPT}) \\ 2.851(58) & (\text{polynomial}) \end{cases} \quad (8.2)$$

$$f_\pi[\text{GeV}] = \begin{cases} 0.1238(21) & (\text{resummed WChPT}) \\ 0.1247(31) & (\text{polynomial}) \end{cases} \quad (8.3)$$

Though the chiral logarithm appears in the resummed WChPT extrapolation, the pseudoscalar meson decay constant does not show clear function form dependence. The difference is 1%(0.3 σ). On the other hand, quark masses clearly depend on the extrapolation

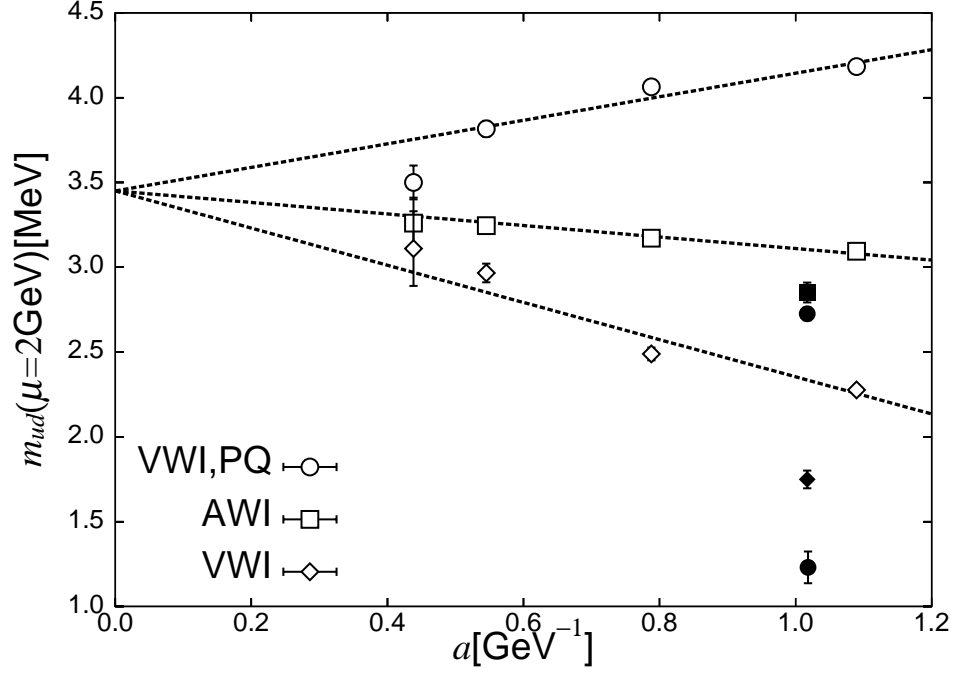


Figure 8.2: Comparison of degenerate up and down quark masses obtained by chiral extrapolations with polynomials. Filled circle symbols represent the results obtained with the resummed WChPT formulae.

forms as shown in Fig. 8.2 and Fig. 8.3. The difference is 42%(5.5 σ) for the VWI quark mass and 5%(2.2 σ) for the AWI quark mass. These results suggest that for a controlled chiral extrapolations of quark masses the WChPT formulae are necessary.

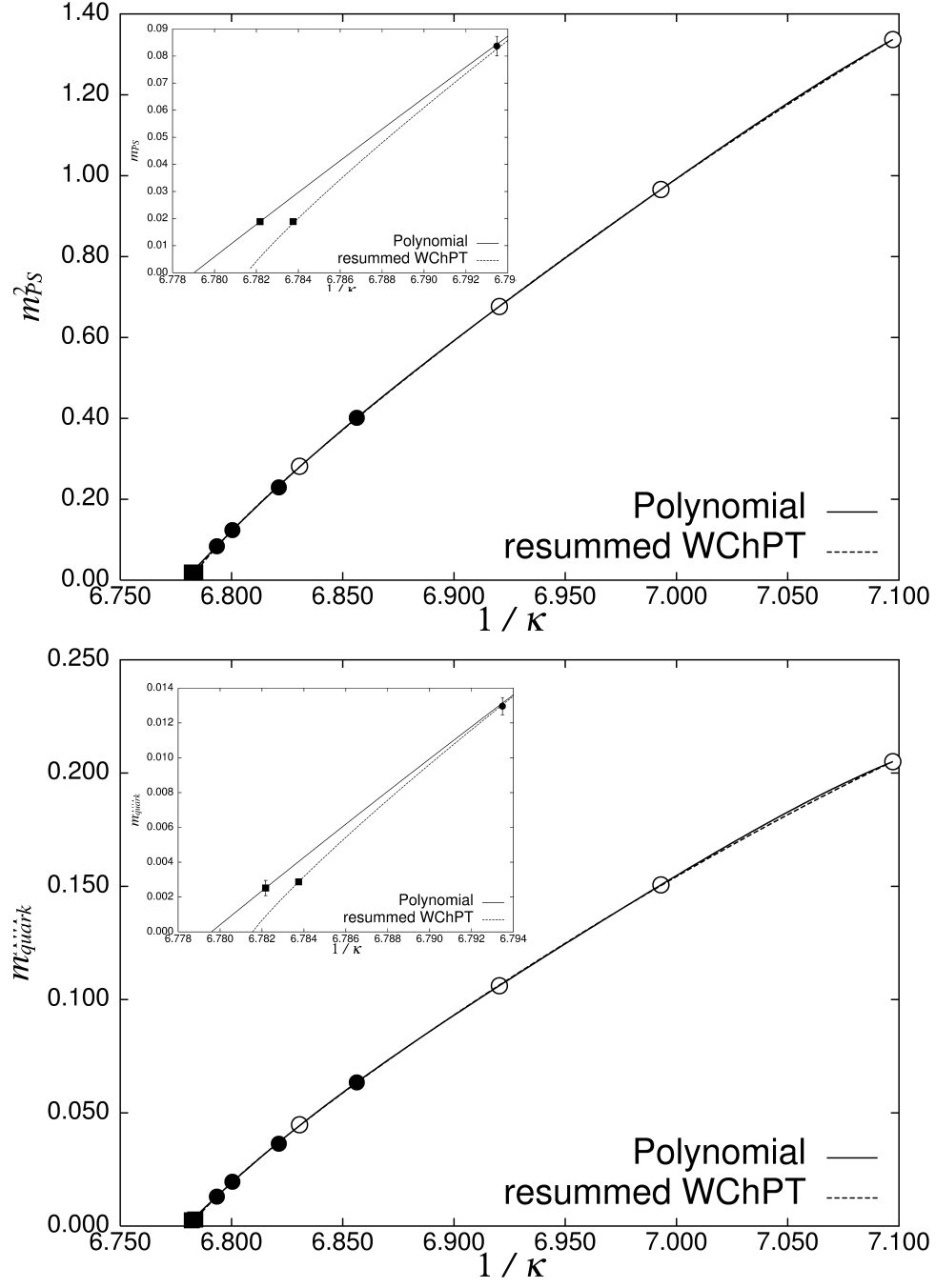


Figure 8.3: Comparisons of the polynomial and the resummed WChPT fits to pseudoscalar meson masses and AWI quark masses. The circle shows the lattice data and the square is the extrapolated result to the physical point.

Chapter 9

Conclusions

In this thesis we have presented a study of the hadron spectrum and quark masses in two-flavor QCD with small sea quark mass data down to $m_{PS}/m_V = 0.35$, using the RG gauge action and the meanfield-improved Wilson quark action.

We found previous extrapolations from $m_{PS}/m_V = 0.80 - 0.55$ data with quadratic functions show systematic deviations from those with $m_{PS}/m_V = 0.80 - 0.35$. The extrapolation from $m_{PS}/m_V = 0.80 - 0.35$ give 7%(3.5 σ) smaller value for the lattice spacing. The differences are especially large for the quark masses. 8%(4.2 σ) decrease is observed for the AWI quark mass and 23%(10 σ) for the VWI quark mass. The previous quadratic extrapolations underestimated the sea quark mass dependence and the correct quark mass in the continuum limit may have smaller values by 10 – 20% than that in the previous estimation.

The difference from the previous extrapolation may be from the chiral singularity, which requires high order terms for polynomial extrapolations. Therefore we tested the formulae based on ChPT. We found the naive one-loop ChPT formulae fail to reproduce our data of $m_{PS}/m_V = 0.80 - 0.35$. They must be applied under $m_{PS}/m_V = 0.60$ for a reasonable χ^2/dof . The narrow fitting range makes the extrapolations less predictive.

Since the chiral symmetry is explicitly broken for the Wilson-type fermion, it may be a source of the failure of the naive one-loop ChPT formulae. Actually the resummed one-loop WChPT formulae including $O(a^2)$ effects describe our data well. We have also confirmed that the convergence of the resummed WChPT formulae is well. The one-loop contribution take reasonable values up to 30% within our data range. Therefore, systematic errors concerning chiral extrapolations are expected to be controlled well by use of the one-loop WChPT formulae for our data of $m_{PS}/m_V = 0.80 - 0.35$.

The influence by the WChPT formulae appears in quark masses at the physical point.

The polynomial extrapolation and the WChPT formula give similar values for the pseudoscalar meson decay constant at the physical point. The difference is within the statistical error. However, the difference is remarkable for quark masses.

$$m_R^{VWI}(\mu = 2 \text{ GeV})[\text{MeV}] = \begin{cases} 1.230(94) & (\text{resummed WChPT}) \\ 1.749(53) & (\text{polynomial}) \end{cases} \quad (9.1)$$

$$m_R^{AWI}(\mu = 2 \text{ GeV})[\text{MeV}] = \begin{cases} 2.725(38) & (\text{resummed WChPT}) \\ 2.851(58) & (\text{polynomial}) \end{cases} \quad (9.2)$$

The WChPT formulae give smaller values than those obtained with polynomials, 5%(2.2 σ) for the AWI quark mass and 42%(5.5 σ) for the VWI quark mass. It suggests indispensability of the WChPT formulae for the calculation of quark masses.

Certainly more works at smaller lattice spacings are needed. This work is carried out at a single lattice spacing. Scaling checks of WChPT are important to confirm the validity of WChPT. Another point is the $\rho \rightarrow \pi\pi$ effect. Since $\rho \rightarrow \pi\pi$ is a higher order contribution, it does not change the extrapolation of the vector meson mass dramatically but it can be a source of systematic deviations. Therefore, in addition to our check of a vector meson decay by polarization effects, more careful analysis using the finite volume method [50, 51] should be done.

Acknowledgements

I'd like to thank Prof. K. Kanaya, Prof. A. Ukawa and Prof. S. Aoki for their guidances and discussions. I am also thankful to Dr. T. Kaneko, Dr. K. Ishikawa and Prof. T. Yoshie for their supports and to Prof. N. Ishizuka and Prof. Y. Iwasaki for advices and suggestions. All staffs and students of the Institute of Theoretical Physics of the University of Tsukuba, especially to my colleagues K. Ide and T. Yamazaki, and the members of the CP-PACS collaboration are appreciated for discussions.

This work is supported in part by Large Scale Numerical Simulation Project of the Science Information Processing Center, University of Tsukuba.

Bibliography

- [1] K.G. Wilson, Phys. Rev. D **10**, 2445 (1974).
- [2] M. Lüscher *et al.*, Nucl. Phys. B **491**, 344 (1997);
S. Capitani *et al.* (ALPHA Collaboration) *ibid.* B **544**, 669 (1999).
- [3] M. Fukugita *et al.*, Phys. Lett. B **294**, 380 (1992); Phys. Rev. D **47**, 4739 (1993).
- [4] S. Aoki *et al.*, Phys. Rev. D **50**, 486 (1994).
- [5] S. Aoki *et al.* (JLQCD Collaboration), Phys. Rev. D **68**, 054502 (2003).
- [6] J.B. Kogut and L. Susskind, Phys. Rev. D **11**, 395 (1975).
- [7] K.G. Wilson, New Phenomena in Subnuclear Physics(Plenum,New York), 69 (1975).
- [8] C. Bernard *et al.* (MILC Collaboration), Nucl. Phys. B (Proc. Suppl.) **73**, 198 (1999);
ibid. **60A**, 297 (1998) and references therein.
- [9] J. Gasser and H. Leutwyler, Ann. Phys. **158**, 142 (1984);
Nucl. Phys. B **250**, 465;517;539 (1985).
- [10] S.R. Sharpe and N. Shores, Phys. Rev. D **62** 094503 (2000).
- [11] S. Durr, Eur. Phys. J. C **29** 383 (2003).
- [12] S.R. Sharpe and R. Singleton Jr., Phys. Rev. D **58** 074501 (1998).
- [13] G. Rupak and N. Shores, Phys. Rev. D **66** 054503 (2002).
- [14] O. Bär, G. Rupak and N. Shores, hep-lat/0306021.
- [15] S. Aoki, Phys. Rev. D **68** 054508 (2003).
- [16] W. Lee and S.R. Sharpe, Phys. Rev. D **60** 114503 (1999).

- [17] C. Bernard, Phys. Rev. D **65** 054031 (2002).
- [18] C. Aubin and C. Bernard, Phys. Rev. D **68** 034014 (2003); *ibid.* 074011 (2003).
- [19] F. Farchioni *et al.* (qq+q Collaboration), Phys. Lett. B **561** 102 (2003);
Eur. Phys. J. **C31** 227 (2003).
- [20] A. Ali Khan *et al.* (CP-PACS Collaboration), Phys. Rev. Lett. **85**, 4674 (2000);
Phys. Rev. D **65**, 054505 (2002).
- [21] A. Ukawa, Nucl. Phys. B (Proc. Suppl.) **106**, 195 (2002).
- [22] Y. Namekawa *et al.* (CP-PACS Collaboration),
Nucl. Phys. B (Proc. Suppl.) **119**, 335 (2003).
- [23] K. Symanzik, Nucl. Phys. B **226**, 187 (1983); *ibid.* 205.
- [24] Y. Iwasaki, Nucl. Phys. B **258**, 141 (1985);
Univ. of Tsukuba report UTHEP-118 (1983), unpublished.
- [25] B. Sheikholeslami and R. Wohlert, Nucl. Phys. B **259**, 572 (1985).
- [26] G.P. Lepage and P.B. Mackenzie, Phys. Rev. D **48**, 2250 (1993).
- [27] M. Lüscher *et al.*, Nucl. Phys. B **478**, 365 (1996); *ibid.* B **491**, 323 (1997).
- [28] G. Colangelo, J. Gasser and H. Leutwyler, Nucl. Phys. B **603**, 125 (2001).
- [29] S. Aoki *et al.* (CP-PACS Collaboration), Phys. Rev. Lett. **84**, 238 (2000);
Phys. Rev. D **67**, 034503 (2003).
- [30] S.R. Sharpe, Phys. Rev. D **46**, 3146 (1992).
- [31] C.W. Bernard and M.F.L. Golterman, Phys. Rev. D **46**, 853 (1992).
- [32] S. Aoki *et al.* (CP-PACS Collaboration), Phys. Rev. D **60**, 114508 (1999).
- [33] S. Duane, A.D. Kennedy, B.J. Pendleton, and D. Roweth,
Phys. Lett. B **195**, 216 (1987).
- [34] S. Gottlieb, W. Liu, D. Toussaint, R.L. Renken and R.L. Sugar,
Phys. Rev. D **35**, 2531 (1987).

- [35] H. van der Vorst, SIAM J. Sc. Stat. Comp. **13**, 631 (1992).
- [36] G.L.G. Sleijpen and D.R. Fokkema, Elec. Trans. on Numer. Anal. **1**, 11 (1993).
- [37] S. Itoh and Y. Namekawa, J. Comp. Appl. Math. **159**, 65 (2003).
- [38] T. Miyauchi, S. Itoh, S. Zhang and M. Natori,
Trans. of Japan Soc. for Ind. and Appl. Math. **11** No.2, 49 (2001).
- [39] K. Jansen and R. Sommer, Nucl. Phys. B **530**, 185 (1998).
- [40] A. Ukawa, private communication.
- [41] C. Bernard *et al.*, Phys. Rev. D **48**, 4419 (1993).
- [42] C. McNeile *et al.*, Phys. Lett. B **556** 177 (2003).
- [43] E. Jenkins, A.V. Manohar and M.B. Wise, Phys. Rev. Lett. **75**, 2272 (1995).
- [44] V. Bernard, N. Kaiser and U.G. Meissner, Z. Phys. C **60**, 111 (1993).
- [45] S. Aoki, Phys. Rev. D **30**, 2653 (1984); Phys. Rev. Lett. **57**, 3136 (1986);
Nucl. Phys. B **314**, 79 (1989); Prog. Theor. Phys. **122**, 179 (1996)
- [46] S. Aoki and A. Gocksch, Phys. Lett. B **231**, 449 (1989); *ibid.* **243**, 409 (1990);
Phys. Rev. F **45**, 3845 (1992).
- [47] S. Aoki, A. Ukawa and T. Umemura, Phys. Rev. Lett. **76**, 873 (1996);
S. Aoki, T. Kaneda and A. Ukawa, Phys. Rev. D **56**, 1808 (1997)
- [48] K.G. Chetyrkin, Phys. Lett. B404, 161 (1997).
- [49] J.A.M. Vermaseren, S.A. Larin and T. van Ritbergen, Phys. Lett. B405, 327 (1997).
- [50] M. Lüscher, Commun. Math. Phys. **105** 153 (1986).
- [51] K. Rummukainen and S. Gottlieb, Nucl. Phys. B **450**, 397 (1995).
- [52] S. Aoki, R. Frezzotti and P. Weisz, Nucl. Phys. B **540**, 501 (1999).
- [53] S. Aoki, K. Nagai, Y. Taniguchi and A. Ukawa, Phys. Rev. D **58**, 074505 (1998);
Y. Taniguchi and A. Ukawa, *ibid.* **58**, 114503 (1998).

- [54] G.S. Bali and K. Schilling, Phys. Rev. D **46**, 2636 (1992);
G.S. Bali, K. Schilling and C. Schlichter, *ibid.* **51**, 5165 (1995)
- [55] C.B. Lang and C. Rebbi, Phys. Lett. B **115**, 137 (1982).
- [56] R. Sommer, Nucl. Phys. B **411**, 839 (1994).

Appendix A

Measurements of observables

A.1 Hadron Masses

Meson operators are defined by

$$M(x) = \bar{q}^{(f)}(x) \Gamma q^{(g)}(x), \quad \Gamma = I, \gamma_5, \gamma_\mu, \gamma_5 \gamma_\mu, \quad (\text{A.1})$$

where f and g are flavor indices and x is the coordinates on the lattice. Meson correlators are calculated as

$$\langle M(n) M(0) \rangle. \quad (\text{A.2})$$

The octet baryon operator is defined as

$$O^{fgh}(x) = \epsilon^{abc} \left(q^{(f)a}(x)^T C \gamma_5 q^{(g)b}(x) \right) q^{(h)c}(x), \quad (\text{A.3})$$

where a, b, c are color indices and $C = \gamma_4 \gamma_2$ is the charge conjugation matrix. $\alpha = 1, 2$ represents the z -component of the spin $J_z = 1/2$. Decuplet baryon correlators are calculated using an operator defined by

$$D^{fgh}(x) = \epsilon^{abc} \left(q^{(f)a}(x)^T C \gamma_\mu q^{(g)b}(x) \right) q^{(h)c}(x). \quad (\text{A.4})$$

For each configuration quark propagators are calculated with a point source and a smeared source. For the smeared source, we fix the gauge configuration to the Coulomb gauge and use an exponential smearing function $\psi(r) = A \exp(-Br)$ for $r > 0$ with $\psi(0) = 1$. We chose $A = 1.25$ and $B = 0.50$ as in our previous study [20].

In order to reduce the statistical fluctuation of hadron correlators, we repeat the measurement for two choices of the location of the hadron source, $t_{src} = 1$ and $N_t/2 + 1 (= 13)$ and take the average over the two [5]:

$$\frac{1}{2} \left(\left\langle M(t_{src} + t) M(t_{src})^\dagger \right\rangle_{t_{src}=1} + \left\langle M(t_{src} + t) M(t_{src})^\dagger \right\rangle_{t_{src}=N_t/2+1} \right). \quad (\text{A.5})$$

This procedure reduces the statistical error of hadron correlators by typically 30-40%, which suggests that the statistics is increased effectively by a factor of 1.7–2. For further reduction of the statistical fluctuation, we take the average over three polarization states for vector mesons, two spin states for octet baryons and four spin states for decuplet baryons.

Hadron masses are extracted by χ^2 fits to hadron correlators, taking account of correlations among different time slices. A single hyperbolic cosine form is assumed for mesons, and a single exponential form for baryons. Inspecting stability of the fitted mass, we set the lower cut of the fit range. Statistical errors of hadron masses are estimated with the jack-knife procedure.

A.2 Decay constants

The pseudoscalar meson decay constant is calculated by

$$f_{PS} = 2\kappa u_0 Z_A \left(1 + b_A \frac{m_{quark}^{VWI}}{u_0} \right) \frac{C_A^s}{C_P^s} \sqrt{\frac{2C_P^l}{m_{PS}}}, \quad (\text{A.6})$$

where the superscripts l and s distinguish local and smeared operators. The VWI quark mass m_{quark}^{VWI} is defined by

$$m_{quark}^{VWI} = \frac{1}{2} \left(\frac{1}{\kappa} - \frac{1}{\kappa_c} \right). \quad (\text{A.7})$$

The critical hopping parameter κ_c is determined by chiral extrapolations as discussed in Sec. 7. Various amplitudes are extracted in the following steps. The pseudoscalar mass m_{PS} and the amplitude C_P^s are determined from

$$\langle P^l(t) P^s(0) \rangle = C_P^s [\exp(-m_{PS}t) + \exp(-m_{PS}(L_t - t))]. \quad (\text{A.8})$$

Keeping m_{PS} fixed, we extract C_P^l and C_A^s from the fits

$$\langle P^l(t) P^l(0) \rangle = C_P^l [\exp(-m_{PS}t) + \exp(-m_{PS}(L_t - t))], \quad (\text{A.9})$$

$$\langle A_4^l(t) P^s(0) \rangle = C_A^s [\exp(-m_{PS}t) - \exp(-m_{PS}(L_t - t))]. \quad (\text{A.10})$$

Since non-perturbatively determined values for Z_A , b_A and c_A are not available for our combination of actions in two-flavor QCD, we adopt one-loop perturbative values in Refs. [52, 53] with the tadpole improvement.

Vector meson decay constant f_V is defined as

$$\langle 0 | V_i | V \rangle = \epsilon_i f_V m_V, \quad (\text{A.11})$$

where ϵ_i is a polarization vector. The procedure to obtain the vector meson decay constant is parallel to the one for pseudoscalar decay constant. The rho correlator with smeared source is fitted with

$$\langle V^l(t)V^s(0) \rangle = C_V^s [\exp(-m_V t) + \exp(-m_V(L_t - t))], \quad (\text{A.12})$$

which determines m_V and C_V^s . Using m_V as an input we make fits to the correlator

$$\langle V^l(t)V^l(0) \rangle = C_V^l [\exp(-m_V t) + \exp(-m_V(L_t - t))], \quad (\text{A.13})$$

where the amplitude C_V^l is the only fit parameter. A renormalized vector meson decay constant is then obtained through

$$f_V = 2\kappa u_0 Z_V \left(1 + b_V \frac{m_{VWI}}{u_0}\right) \sqrt{\frac{2C_V^l}{m_V}}, \quad (\text{A.14})$$

where we also use one-loop perturbative values of Z_V, b_V in Refs. [52, 53]. We do not include the improvement term $c_V \bar{\partial}_\nu T_{n\mu\nu}$, because the corresponding correlator is not measured.

A.3 bare quark masses

The up-down quark masses are calculated through the vector Ward identity m_{VWI} and the axial vector Ward identity m_{AWI} . These two kinds of quark masses may differ because of explicit violation of chiral symmetry at finite lattice spacings. A bare VWI quark mass is defined by Eq. (A.7). A bare AWI quark mass m_{quark}^{AWI} is calculated using the fourth component of the improved axial vector current

$$A_4^{imp} = A_4 + c_A \partial_4 P, \quad (\text{A.15})$$

where ∂_4 is the symmetric lattice derivative. Then, m_{quark}^{AWI} is obtained through

$$m_{quark}^{AWI} = \frac{m_{PS} C_A}{2C_P}, \quad (\text{A.16})$$

where C_A and C_P are the amplitudes of $\langle A_4^{imp}(t)P(0)^\dagger \rangle$ and $\langle P(t)P(0)^\dagger \rangle$ with the smeared source and the local sink operators.

A.4 Static quark potential

The static quark potential $V(r)$ is calculated from the temporal Wilson loops $W(r, t)$

$$W(r, t) = C(r) \exp(-V(r)t). \quad (\text{A.17})$$

To obtain the clear signals, smearing techniques are often employed for the static potential. Smearing enhances the ground state contributions in the temporal Wilson loops. Then we can obtain the static potential from rather small t , where the errors of the Wilson loops are small. As t becomes larger, signals of the Wilson loops become worse rapidly. We apply the smearing procedure of Ref. [54]. We replace a spatial link by the sum of the staple products

$$U_{n,i} \rightarrow \sum_{j=\pm 1, \dots, \pm 3, j \neq \pm i} U_{n,j} U_{n+\hat{j},i} U_{n+\hat{i},j}^\dagger. \quad (\text{A.18})$$

Smearing is applied to all the spatial links iteratively. We repeat this procedure several times and construct the Wilson loop from the smeared link variables. We inspect the t dependence of the effective potential

$$V_{eff}(r, t) = \log [W(r, t)/W(r, t+1)]. \quad (\text{A.19})$$

We determine the lower cut of t by the plateau of V_{eff} . Then, we perform a correlated fit to $V(r) = V_{eff}(r, t_{min})$ with

$$V(r) = V_0 - \frac{\alpha}{r} + \sigma r. \quad (\text{A.20})$$

Since the rotational symmetry is well-restored by use of an RG-improved action, the lattice correction to the Coulomb term calculated perturbatively from one lattice-gluon exchange diagram [55] is not included.

The Sommer scale r_0 defined through [56]

$$r_0^2 \left. \frac{dV(r)}{dr} \right|_{r=r_0} = 1.65. \quad (\text{A.21})$$

r_0 is extracted by the numerical derivatives or the parameterization of the potential $V(r)$:

$$r_0 = \sqrt{\frac{1.65 - \alpha}{\sigma}}. \quad (\text{A.22})$$

A.5 Autocorrelation

Since configurations are produced subsequently by any algorithms, there are a lot of similarities in the configurations. The correlation in the sequence of configurations is called as autocorrelation.

The autocorrelation of lattice data is studied by calculating the cumulative autocorrelation time

$$\tau_{\mathcal{O}}^{cum}(\Delta t_{max}) = \frac{1}{2} + \sum_{\Delta t=1}^{\Delta t_{max}} \rho_{\mathcal{O}}(\Delta t), \quad (\text{A.23})$$

where $\rho_{\mathcal{O}}(t)$ is the autocorrelation function

$$\rho_{\mathcal{O}}(\Delta t) = \frac{\Gamma_{\mathcal{O}}(\Delta t)}{\Gamma_{\mathcal{O}}(0)}, \Gamma_{\mathcal{O}}(\Delta t) = \langle (\mathcal{O}(t) - \langle \mathcal{O} \rangle) (\mathcal{O}(t + \Delta t) - \langle \mathcal{O} \rangle) \rangle \quad (\text{A.24})$$

where Δt should be taken large enough.

Appendix B

Jackknife error estimation for full QCD simulations

Throughout this thesis, uncorrelated fits are used for chiral extrapolations. However, measurements of different observables have been done on each configuration, observables obtained on the same configuration are correlated. Central values of uncorrelated fits do not differ from those of correlated fits significantly. On the other hand, errors are often underestimated in the case of uncorrelated fits. By use of the jack-knife method, the errors of fit parameters can still be correctly estimated [20].

The jack-knife method is implemented for full QCD simulations in the following way. First, hadron masses are determined with the usual jack-knife method. This yields mass estimates $m_{\text{H}}^{(J)i}(\kappa_{\text{sea}}^k)$ for each jack-knife ensemble obtained by omitting the gauge configuration number i from the run with sea hopping parameter number k . Mean values and variances are defined by

$$m_{\text{H}}(\kappa_{\text{sea}}^k) = \frac{1}{N_k} \sum_{i=1}^{N_k} m_{\text{H}}^{(J)i}(\kappa_{\text{sea}}^k), \quad (\text{B.1})$$

$$\left(\Delta m_{\text{H}}(\kappa_{\text{sea}}^k)\right)^2 = \frac{N_k - 1}{N_k} \sum_{i=1}^{N_k} \left(m_{\text{H}}^{(J)i}(\kappa_{\text{sea}}^k) - m_{\text{H}}(\kappa_{\text{sea}}^k)\right)^2. \quad (\text{B.2})$$

Chiral fits are then carried out by replacing mean values $m_{\text{H}}(\kappa_{\text{sea}}^k)$ with jack-knife estimates $m_{\text{H}}^{(J)i}(\kappa_{\text{sea}}^k)$ for the sea hopping parameter number k while keeping masses at all other sea hopping parameters at their mean value. This procedure gives error estimates $(\Delta P)_k$ as above, where P stands for a fit parameter or a quantity derived from fit parameters. Since runs at different sea quarks are uncorrelated, the total error ΔP is determined by quadratic addition $(\Delta P)^2 = \sum_k ((\Delta P)_k)^2$.

Appendix C

Renormalization factors and improvement coefficients

One-loop renormalization factors and improvement coefficients used in this thesis are summarized [52, 53].

For the coupling constant we adopt a mean-field improved value [26] in the modified minimal subtraction ($\overline{\text{MS}}$) scheme obtained in the following way. We start with the one-loop perturbative relation between the bare and $\overline{\text{MS}}$ couplings for the RG improved gauge action and the $O(a)$ -improved Wilson quark action [53],

$$\frac{1}{g_{\overline{\text{MS}}}^2(\mu)} = \frac{1}{g^2} + 0.1000 + 0.03149N_f + \frac{11 - \frac{2}{3}N_f}{8\pi^2} \log(\mu a). \quad (\text{C.1})$$

The formula is reorganized so that $1/g^2$ becomes the coefficient in front of $F_{\mu\nu}^2$ in the continuum limit after the mean field approximation. Using the one-loop expressions [24] $P = 1 - 0.1402g^2$ and $R = 1 - 0.2689g^2$ for the expectation value of the plaquette $P = \langle W^{1 \times 1} \rangle$ and the 1×2 rectangle $R = \langle W^{1 \times 2} \rangle$, we obtain the relation

$$\frac{1}{g_{\overline{\text{MS}}}^2(\mu)} = \frac{c_0 P + 8c_1 R}{g^2} - 0.1006 + 0.03149N_f + \frac{11 - \frac{2}{3}N_f}{8\pi^2} \log(\mu a). \quad (\text{C.2})$$

Tadpole-improvement is realized by using nonperturbatively measured values of P and R . For full QCD we use values extrapolated to the chiral limit of the sea quark. Numerical values of P and R used in the calculation are given in Tables D.5.

The VWI quark mass is renormalized with

$$m_R = Z_m \left(1 + b_m \frac{m}{u_0} \right) \frac{m}{u_0}, \quad (\text{C.3})$$

where

$$Z_m = 1 + g_{\overline{\text{MS}}}^2(\mu) \left(0.0400 - \frac{1}{4\pi^2} \log(\mu a)^2 \right), \quad (\text{C.4})$$

and

$$b_m = -\frac{1}{2} - 0.0323g_{\overline{\text{MS}}}^2(\mu). \quad (\text{C.5})$$

For u_0

$$u_0 = P^{1/4} = \left(1 - \frac{0.8412}{\beta}\right)^{1/4} \quad (\text{C.6})$$

is used.

The local pseudoscalar density $P_n = \bar{\psi}_n \gamma_5 \psi_n$ is renormalized with

$$P_n^R = 2\kappa u_0 Z_P \left(1 + b_P \frac{m}{u_0}\right) P_n, \quad (\text{C.7})$$

where

$$Z_P = 1 + g_{\overline{\text{MS}}}^2(\mu) \left(-0.0523 + \frac{1}{4\pi^2} \log(\mu a)^2\right), \quad (\text{C.8})$$

and

$$b_P = 1 + 0.0397g_{\overline{\text{MS}}}^2(\mu). \quad (\text{C.9})$$

The renormalized axial vector current A_μ^R , improved to $O(g^2 a)$, is obtained through

$$A_{n\mu}^R = 2\kappa u_0 Z_A \left(1 + b_A \frac{m}{u_0}\right) (A_{n\mu} + c_A \tilde{\partial}_\mu P_n), \quad (\text{C.10})$$

where $A_{n\mu} = \bar{\psi}_n i\gamma_\mu \gamma_5 \psi_n$ is the bare local current and $\tilde{\partial}_\mu$ the symmetric lattice derivative. Perturbative expressions for the renormalization factor and the improvement coefficients are

$$Z_A = 1 - 0.0215g_{\overline{\text{MS}}}^2(\mu), \quad (\text{C.11})$$

$$b_A = 1 + 0.0378g_{\overline{\text{MS}}}^2(\mu), \quad (\text{C.12})$$

$$c_A = -0.0038g_{\overline{\text{MS}}}^2(\mu). \quad (\text{C.13})$$

Similarly, the renormalized vector current V_μ^R is obtained from the bare local vector current $V_{n\mu} = \bar{\psi}_n \gamma_\mu \psi_n$ and $T_{n\mu\nu} = \bar{\psi}_n i\sigma_{\mu\nu} \psi_n$ through

$$V_{n\mu}^R = 2\kappa u_0 Z_V \left(1 + b_V \frac{m}{u_0}\right) (V_{n\mu} + c_V \tilde{\partial}_\nu T_{n\mu\nu}). \quad (\text{C.14})$$

Here the perturbative results are

$$Z_V = 1 - 0.0277g_{\overline{\text{MS}}}^2(\mu), \quad (\text{C.15})$$

$$b_V = 1 + 0.0382g_{\overline{\text{MS}}}^2(\mu), \quad (\text{C.16})$$

$$c_V = -0.0097g_{\overline{\text{MS}}}^2(\mu). \quad (\text{C.17})$$

Appendix D

Hadron spectrum data

κ_{sea}	m_{PS}	$[t_{min}, t_{max}]$	χ^2/dof	m_V	$[t_{min}, t_{max}]$	χ^2/dof
0.14585	0.6336(14)	[6,12]	0.76(84)	1.0405(38)	[6,12]	0.40(51)
0.14660	0.4789(23)	[6,12]	1.60(119)	0.9410(81)	[6,12]	2.36(102)
0.14705	0.3517(30)	[6,12]	0.63(84)	0.8522(144)	[6,12]	0.76(88)
0.14720	0.2893(61)	[6,12]	0.50(93)	0.8300(413)	[6,12]	0.95(92)

Table D.1: Meson masses on $12^3 \times 24$ lattice.

κ_{sea}	m_{quark}^{AWI}
0.14585	0.06340(34)
0.14660	0.03632(39)
0.14705	0.01951(31)
0.14720	0.01296(49)

Table D.2: Bare AWI quark masses on $12^3 \times 24$ lattice.

κ_{sea}	f_{PS}	$[t_{min}, t_{max}]$	f_V	$[t_{min}, t_{max}]$
0.14585	0.1785(14)	[6,12]	0.3118(33)	[6,12]
0.14660	0.15784(87)	[6,12]	0.2874(57)	[6,12]
0.14705	0.1413(14)	[6,12]	0.2491(98)	[6,12]
0.14720	0.1412(41)	[6,12]	0.2422(239)	[6,12]

Table D.3: Decay constants on $12^3 \times 24$ lattice. Here for the renormalization factor we employ κ_c determined from a simultaneous fit to m_{PS}^2 and m_{quark}^{AWI} in Table 7.2.

κ_{sea}	m_N	$[t_{min}, t_{max}]$	χ^2/dof	m_Δ	$[t_{min}, t_{max}]$	χ^2/dof
0.14585	1.5357(69)	[5,12]	0.65(76)	1.7722(97)	[5,12]	0.74(83)
0.14660	1.3619(92)	[5,12]	0.85(66)	1.6061(183)	[5,12]	1.45(97)
0.14705	1.2054(165)	[5,12]	0.69(96)	1.5110(268)	[5,12]	1.28(81)
0.14720	1.1791(417)	[5,12]	0.99(62)	1.5300(1020)	[5,12]	0.62(123)

Table D.4: Baryon masses on $12^3 \times 24$ lattice.

κ_{sea}	$\langle W^{1 \times 1} \rangle$	$\langle W^{1 \times 2} \rangle$
0.14585	0.504529(56)	0.249916(70)
0.14660	0.508445(69)	0.254866(88)
0.14705	0.511202(68)	0.258350(86)
0.14720	0.51263(14)	0.26016(19)
$m_{PS}^2 = 0$	0.51485(11)	0.26294(14)

Table D.5: Plaquette and rectangular loops on $12^3 \times 24$ lattice.

κ_{sea}	m_{PS}	$[t_{min}, t_{max}]$	χ^2/dof	m_V	$[t_{min}, t_{max}]$	χ^2/dof
0.14585	0.6333(19)	[6,12]	0.72(52)	1.0488(43)	[6,12]	0.82(76)
0.14660	0.4781(16)	[6,12]	3.55(204)	0.9403(70)	[6,12]	1.41(93)

Table D.6: Meson masses on $16^3 \times 24$ lattice.

κ_{sea}	m_{quark}^{AWI}
0.14585	0.06378(47)
0.14660	0.03642(40)

Table D.7: Bare AWI quark masses on $16^3 \times 24$ lattice.

κ_{sea}	f_{PS}	$[t_{min}, t_{max}]$	f_V	$[t_{min}, t_{max}]$
0.14585	0.1804(23)	[6,12]	0.3151(45)	[6,12]
0.14660	0.1592(16)	[6,12]	0.2913(48)	[6,12]

Table D.8: Decay constants on $16^3 \times 24$ lattice. Here for the renormalization factor we employ κ_c determined from a simultaneous fit to m_{PS}^2 and m_{quark}^{AWI} in Table 7.2.

κ_{sea}	m_N	$[t_{min}, t_{max}]$	χ^2/dof	m_Δ	$[t_{min}, t_{max}]$	χ^2/dof
0.14585	1.5567(91)	[5,12]	1.97(92)	1.7804(113)	[5,12]	0.64(54)
0.14660	1.3257(118)	[5,12]	1.58(91)	1.5899(124)	[5,12]	0.96(77)

Table D.9: Baryon masses on $16^3 \times 24$ lattice.

κ_{sea}	$\langle W^{1 \times 1} \rangle$	$\langle W^{1 \times 2} \rangle$
0.14585	0.504482(75)	0.249850(90)
0.14660	0.508338(61)	0.254739(76)

Table D.10: Plaquette and rectangular loops on $16^3 \times 24$ lattice.

$12^3 \times 24$				
κ_{sea}	t_{min}	r_{min}	σ	r_0
0.14585	2	$\sqrt{2}$	0.329(6)(42)(91)	2.004(8)(58)(77)
0.14660	2	$\sqrt{2}$	0.289(5)(117)(64)	2.107(8)(37)(54)
0.14705	2	$\sqrt{2}$	0.278(5)(38)(34)	2.167(9)(80)(25)
0.14720	2	$\sqrt{2}$	0.255(8)(10)(42)	2.237(17)(10)(34)
$16^3 \times 24$				
κ_{sea}	t_{min}	r_{min}	σ	r_0
0.14585	2	$\sqrt{2}$	0.313(11)(10)(90)	2.011(10)(17)(72)
0.14660	2	$\sqrt{2}$	0.270(6)(67)(66)	2.131(11)(50)(39)

Table D.11: Sommer scale r_0 at simulated sea quark masses. The first error is statistical. The second and third ones are the systematic errors due to the choice of t_{min} and r_{min} .